Lakehead University

Knowledge Commons,http://knowledgecommons.lakeheadu.ca

Electronic Theses and Dissertations Electronic Theses and Dissertations from 2009

2020

Medical applications of fluorine-19 and hyperpolarized xenon129 magnetic resonance imaging

Shepelytskyi, Yurii

http://knowledgecommons.lakeheadu.ca/handle/2453/4754

Downloaded from Lakehead University, KnowledgeCommons

Medical Applications of Fluorine-19 and Hyperpolarized Xenon-129 Magnetic Resonance Imaging

by

Yurii Shepelytskyi

Faculty of Science & Environmental Studies

Lakehead University, Thunder Bay, Ontario

October 2020

A dissertation submitted in partial fulfillment

of the requirements of the degree of Doctor of Philosophy

Chemistry and Materials Science Program

Thunder Bay, Ontario, Canada 2020

Yurii Shepelytskyi 2020 ©

Medical Applications of Fluorine-19 and Hyperpolarized Xenon-129 Magnetic Resonance Imaging

Yurii Shepelytskyi

Doctor of Philosophy, 2020

Chemistry and Materials Science Program

Lakehead University

Abstract

Multinuclear magnetic resonance imaging (MRI) is currently under extensive development. Although conventional proton MRI is mostly known as an anatomical medical imaging modality with an excellent soft tissue contrast, multinuclear MRI proves that MRI can provide researchers and clinicians with information about the internal organs function. This class of MRI techniques relies on imaging different nuclei than protons. A large part of multinuclear MRI includes fluorine-19 (^{19}F) and hyperpolarized (HP) xenon-129 (^{129}Xe) MRI. ^{19}F MRI is used for functional imaging of the lungs, molecular imaging of fluorinated biosensors, cell labeling, and drug metabolism investigation. On the other hand, HP ^{129}Xe can be used for functional brain imaging along with perfusion imaging of the brain and kidneys.

This thesis is focused on the development of HP ^{129}Xe Time-of-Flight (TOF) perfusion imaging technique, functional lung imaging using octafluorocyclobutane (OFCB), and colorectal adenocarcinoma resistivity detection to 5-fluorouracil (5-FU) using ^{19}F MRI. HP ^{129}Xe TOF pulse sequence is capable to map and measure perfusion quantitively was developed and evaluated in phantoms and healthy volunteers. As a representative application, HP ^{129}Xe TOF perfusion imaging was used to detect hemodynamic response to motor and visual stimuli in healthy brains. The performance of OFCB as a contrast agent has been evaluated in vitro and in vivo and compared to perfluoropropane, which is the most commonly used inhalation agent for ^{19}F lung MRI. Theoretical comparison between both gases was conducted as well. Finally, resistivity detection of human colorectal

adenocarcinoma to 5-FU was performed using ^{19}F chemical shift imaging to access chemotherapy retention in the colorectal cancer.

This work expands the arsenal of multinuclear MRI techniques with completely new approaches that can be readily applied for the current needs of neurology, pulmonology, and oncology.

Acknowledgements

I would like to thank my beloved wife, Mariia Yurchenko, for her patience and love. In the moments of doubts and disbelieve, she was always stoically there trying to cheer me up. I would never endure such a long path without her support. I am also grateful to all my family members for their continuous help and love during this long journey. This work would have never been possible without their support.

I would like to express my sincere gratitude to my supervisor Dr. Mitchell Albert for his guidance, methodological support, and inspiring discussions. Due to Dr. Albert's experienced supervision, I was able to successfully manage over the last four years and join the beauty of magnetic resonance imaging. I would also like to thank the members of my supervisory committee, Dr. Alla Reznik and Dr. Stephen Kinrade, who helped me and provided continued support through the past years. I also would like to deeply thank Dr. Reznik for numerous references that she wrote to different funding agencies.

I would like to thank Mr. Tao Li for his help with numerous experiments and for fascinating engineering and physics discussions.

I would like to thank Dr. Francis T. Hane for his support and his help with animal and human experiments. Also, I would like to thank Dr. Hane for fruitful discussions about the data analysis and statistics.

I would like to express my gratitude to Dr. Michael Campbell for his awesome guidance through the mysterious world of organic synthesis.

I would like to thank Mrs. Vira Grynko for her help with experimental design and conduction, productive discussion of numerous ideas, reviewing experimental results, and endless arguing regarding the desired accuracy of measurements.

I would like to acknowledge every present and past member of Dr. Albert's lab for their contribution to my research and for creating such a friendly and precious work environment. I would like to express endless gratitude to Ms. Martina Agostino, Ms. Elizabeth Turubchuk, and Mrs. Jennifer Plata for their work on managing an infinite amount of regulatory paperwork required for successful conduction of human experiments. Also, I would like to thank them for proofreading and grammar editing of numerous documents filled by me, my papers, and conference abstracts.

I am grateful for the financial support that made this work possible. All of the studies in this thesis were partially supported by the Thunder Bay Regional Health Research Institute. I am thankful for internal and external scholarships that allowed me to conduct these studies. I was supported by Lakehead University President's International Graduate Scholar Award for 2017-2020. I was also supported by an Ontario Graduate Scholarship (OGS) for 2018-2019, Mathematics of Information Technology and Complex Systems (Mitacs) Accelerate Grant for 2018, and Ontario Graduate Fellowship for 2020.

Finally, I would like to thank my cat Freya, my fluffy friend, who made sure that I rest from work playing with her.

List of Abbreviations

5-fluorouracil – 5-FU

Adenosine Tri-Phosphate – ATP

Alkali Metal – AM

Apparent Diffusion Coefficient – ADC

Arterial Spin Labeling – ASL

Bandwidth – BW

Blood Oxygenation Level Dependent – BOLD

Cerebral Blood Flow – CBF

Chemical Shift Imaging – CSI

Chemical Shift Saturation Recovery – CSSR

Computed tomography – CT

Data Acquisition – ACQ

Diffusion-Weighted Imaging – DWI

Dynamic Nuclear Polarization – DNP

Echo Time – TE

Flip Angle – FA

Free Induction Decay – FID

Functional MRI – fMRI

Glycerophosphocholine – GPC

Gradient Echo Pulse Sequence – GRE

Hemodynamic Response – HDR

Hounsfield Units – HU

Hyperpolarized – HP

Iterative Decomposition with Echo Asymmetry and Least Squares Estimation – IDEAL

Magnetic Resonance Imaging – MRI

Magnetic Resonance Spectroscopy – MRS

Nicotinamide Adenine Dinucleotide – NAD

Nuclear Magnetic Resonance – NMR

Number of Signal Averages – NSA

Octafluorocyclobutane – OFCB

Perfluoropropane – PFP

Phosphomonoesters – PME

Positron Emission Tomography – PET

Pseudo-continuous ASL – pCASL

Pulse Sequence Diagram – PSD

Radiofrequency – RF

Red Blood Cells – RBC

Region of Interest – ROI

Repetition Time – TR

Signal-to-Noise Ratio - SNR

Spin Exchange Optical Pumping – SEOP

Time-of-Flight – TOF

Ultrashort Echo Time – UTE

Ventilation/Perfusion Ratio – V/Q

Xenon - Xe

Xenon Transfer Contrast – XTC

List of Tables

List of Figures

Table of Content

Chapter 1: Introduction

1.1 Diagnostic Imaging

Nowadays diagnostic imaging is a vital part of any healthcare system. The use of medical imaging drastically increased over the past decades[3,4] due to the ability of providing anatomical and functional information mostly non-invasively. The main pillars of medical imaging are the following techniques: ultrasound, computed tomography (CT), positron emission tomography (PET),scintigraphy, single photon emission computed tomography (SPECT), and magnetic resonance imaging (MRI). Each of these imaging approaches is widely used for a variety of purposes from diagnostics to image guided surgeries[5–7] and biopsies[8–10]. All medical imaging modalities have some advantages and drawbacks which determine the areas of their application.

Ultrasound imaging relies on propagation of elastic waves in the human body, with frequencies in a range from 1 MHz to 20 MHz[11]. The image is formed based on the detection of the ultrasound waves reflected from the organs back to the transducer[12,13]. Currently this is the most frequently used medical imaging modality after X-rays, and one of the most cost efficient. In addition, usually ultrasound imaging systems are easily portable. However, the signal-to-noise ratio (SNR) of ultrasound images is generally low due to high distortion of sound waves during propagation through tissue and multiple noise sources affecting the detected signal[11]. In addition, the spatial resolution of ultrasound imaging is limited to one half of the spatial US wavelength[13,14], and usually does not exceed 300 um[13]. The main limitation of ultrasound imaging is the high number of image artifacts as well as difficulties of imaging structures behind the bones in the body.

CT reconstructs the image from multiple X-ray attenuation projections through the body under a variety of angles. The CT image is a tissue density map measured in Hounsfield units (HU). The HU value for water is zero, whereas air has a value of −1000.[15] High-density objects such as bones appear bright (HU >> 1) whereas low-density structures such as the lungs appear dark. Currently, CT images have the highest spatial resolution among all medical imaging modalities and it is usually about 30 um[16]. The main limitation of CT imaging is an extremely low contrast in the soft tissues due to their low radio-opacity[17]. Therefore, a variety of a contrast agents are used to overcome this issue. As an example, stable isotopes of xenon (Xe) gas are used for ventilation imaging[18] of the lungs and perfusion imaging[19]. Since Xe has high atomic number, it provides reasonable CT image enhancement, and since Xe easily dissolves in blood it allows further quantification of the blood flow[20]. The main issue associated with CT is the extremely high radiation dose delivered to the patient (10-20 mSV)[21].

PET utilizes the detection of the β^+-decay of radiolabeled tracers injected in the body. This imaging modality has the highest sensitivity[22] due to the absence of natural sources of gamma-rays in the living organism and to low attenuation of this type of radiation by the human body. Therefore, a small dose of radiopharmaceuticals is needed to achieve the image ($\sim 10^{-6}$ g)[23]. PET belongs to metabolic activity imaging and molecular imaging modalities. The following isotopes are most commonly used for PET imaging: ^{11}C, ^{18}F, ^{13}N, and ^{15}O. Although PET is extremely sensitive, the spatial resolution is lower compared to MRI and CT medical imaging modalities[24,25]. The physical limitation of spatial resolution of PET is caused by the positron (β^+) spread range. For example, the positron traveling range for ^{18}F isotope is 0.5 mm[26]. In addition, there are strong time limitations caused by the short half-life of the radiolabeled compounds[27].

SPECT relies on the detection of the γ-rays emitted by radiolabeled tracers (labeling is usually performed using ^{99m}Tc, ^{201}Tl, ^{123I}, ^{121}I)[28]. The data acquisition is performed by rotating the gamma camera around the patient. For accurate SPECT image reconstruction, the number of angular views should be at least equal to the projection image matrix size[28].

Although SPECT is an extremely sensitive medical imaging modality, the spatial resolution of it is even worst compared to PET due to the utilization of a single photon detection scheme. Another drawback of SPECT is utilization of ionizing radiation for imaging. SPECT is often used for perfusion imaging[29–31], molecular imaging[32,33], and pulmonary imaging[34,35].

MRI relies on the detection and localization of nuclear magnetic resonance (NMR) signals originating from the subject placed in a strong magnetic field (usually in a range between 1.5 and 7.0 T). This medical imaging modality produces images with excellent contrast between soft tissues and with a reasonable spatial resolution (~100 um). Furthermore, MRI does not involve ionizing radiation. However, MRI has poor sensitivity[36]. The MRI signal is directly proportional to the concentration of the signal nuclei and spin population excess at Zeeman energy levels. In conventional clinical MRI, the population excess is $\sim 10^{-5}$ which significantly limits MRI sensitivity. Clinical MRI mostly detects the signal of water protons (^{1}H) in the human body. Although conventional ^{1}H MRI is mostly used to provide anatomical information, techniques are also available to functionally image the brain[37] and lungs[38] as well as to image water diffusion[39].

1.2 ^{1}H Magnetic Resonance Imaging

Conventional MRI was invented in 1973 by Paul Lauterbur[40]. In his seminal work, the first two-dimensional back-projections of water capillary phantoms were acquired. This invention revolutionized the field of medical imaging due to its ability to create high-resolution images, good soft tissue contrast, and absence of harmful ionizing radiation.

Conventional MRI relies on Zeeman level splitting[41] of thermally polarized ^{1}H nuclei energy levels. (The MRI physics will be discussed in detail in Section1.4.) However, the population difference of the thermally polarized nuclei is only about 10^{-5}, and the MRI signal is proportional to this population excess[42]. Therefore, the MRI image voxel needs to be large enough to enclose numerous ^{1}H nuclei, limiting spatial resolution. The high soft tissue contrast of MRI originates from the different relaxation times of the nuclei in different tissues. Therefore, there are variety of techniques, suitable for selective imaging of the particular tissues based on the physical properties of the nuclei in that tissue[43–45].

Although conventional proton MRI is a clinically available imaging modality, it still has several challenges which limit its applications. Foremost, it is hard to image organs with low proton density like human lungs. In addition, signal voids and artifacts may result if the imaging area contains regions with large magnetic susceptibility differences. Human lungs are a good example of where tissue/air susceptibility differences yield signal voids on the MRI image[46–48]. Finally, physiological motions cause various image artifacts which should be eliminated from the MRI image. Therefore, respiratory and cardiac gating appear frequently in a clinical practice[49,50] and are essential for cardiac imaging and angiography.

1.3 Multinuclear Magnetic Resonance Imaging

Conventional ^{1}H MRI is a tremendously powerful medical imaging modality, but is still mostly known as an anatomical imaging modality with high soft-tissue contrast. On the other hand, functional information of the different organs sometimes is a key for a successful disease diagnostics and treatment monitoring. In order to acquire functional information, numerous techniques were developed for conventional MRI: diffusion-weighted imaging (DWI), blood oxygenation level dependent (BOLD) functional MRI, oxygen-enhanced MRI, etc.

Another approach, which demonstrated its capability to obtain information about organ function using MRI, relies on imaging different nuclei than protons which can be detected in the MRI scanner. ^{19}F, ^{31}P, ^{129}Xe, ^{3}He, and ^{13}C are the most commonly used nuclei for MRI imaging and spectroscopy (MRS). Each nucleus emits an MRI signal of a very specific frequency and, therefore, the resulting image demonstrates the distribution of desired nuclei.

^{31}P MRS/MRI is used often for detection and tracking of high-energy metabolites and membrane phospholipids such as adenosine tri-phosphate (ATP), phosphomonoesters (PME), glycerophosphocholine (GPC), nicotinamide adenine dinucleotide (NAD), etc[51–53] in human brains and muscles. ^{31}P MRS is widely used for studying brain tumors[54,55], Alzheimer's disease[52], diabetes[56], and muscle metabolism[57–59].

The primary application of ^{19}F MRI is functional imaging of the lungs. The detected MRI signal is produced by inert fluorinated gases which are used as inhalation contrast agents. The inert fluorinated gases are safe for inhalation[48,60,61] and are usually mixed with oxygen in order to prevent asphyxia[46,47,62,63]. ^{19}F MRI of the lungs produces ventilation images which can be used to calculate regional ventilation parameters such as ventilation defect percentage, ventilation volume, and forced exhalated volume during the first second. Furthermore, ^{19}F lung MRI allows measuring Apparent Diffusion Coefficient (ADC)[64,65] and ventilation/perfusion ratio (V/Q)[66] which are valuable parameters for diagnosis of pulmonary diseases. Currently, the most commonly used gases for functional ^{19}F MRI imaging of the lungs are perfluoropropane (PFP)[47,61,67,68] and sulfur hexafluoride (SF_6)[60,69–71]. Recently, octafluorocyclobutane (OFCB) has become of interest in the field of ^{19}F MRI imaging[72–74]. The main relative advantage of inert fluorinated gases is a short spin-lattice relaxation time which allows intensive signal averaging during a single breath-hold. In addition, inert fluorinated gases can be mixed with oxygen and, therefore, can be used for continuous breathing imaging protocols. The main challenge of performing inert fluorinated gas MRI is the short effective spin-spin relaxation time which significantly limits the amount of signal per acquisition.

Besides functional imaging of the lungs, ^{19}F MRI has been used for cell tracking and tumor metabolism investigations. The cell labeling can be conducted either *in situ,* via nonspecific uptake of intravenous tracers by phagocytes, or *ex vivo,* which is the most commonly used approach[75]. Transfection agents[76] and charged lipid incorporation[77] are commonly used to label living cells (even non-phagocytic cells) with perfluorocarbons which can be easily detected in MRI. The main applications of ^{19}F cellular MRI imaging are therapeutic cell migration tracking[78,79] and visualization of metastatic cancer cell distribution[80–82].

^{19}F MRI is also frequently used to study the metabolism of drugs[83]. Probably the most studied application of ^{19}F MRI for drug metabolism is the detection of 5-fluorouracil (5-FU)[84–86]. 5-FU is one of the most commonly used cytotoxic drugs for treatment of different types of solid cancers[87]. It metabolizes primarily in the liver and only a small portion of the administrated dosage enters the tumor. There, 5-FU metabolizes to fluorouridine triphosphate and fluorodeoxyuridine triphosphate which cause RNA and DNA damage respectively. Therefore, it is possible to study 5-FU metabolism and its effect on different tumors by monitoring the MRI signal evolution with time. Recently, ^{19}F MRS allowed tumor resistivity detection based on 5-FU signal evolution[86].

Another group of nuclei commonly used in MRI is the noble gases, particularly ^{3}He and ^{129}Xe[61,88]. These nuclei can be hyperpolarized (HP) which substantially increases their MRI signal[42] (for more information, the reader is referred to Section 1.7). Once polarized, ^{3}He and ^{129}Xe can be used for functional imaging of the lungs which remains the primary application of HP noble gas MRI. Indeed, conventional proton MRI is totally incapable of visualizing the lungs due to low proton density in lung parenchyma and large magnetic susceptibility mismatch between the lung tissue and the air in the airways. By contrast, after inhalation of HP gas, it is possible to acquire an MRI image which represents the gas ventilation regions. Similar to inert fluorinated gas MRI mentioned above, the obtained ventilation images can be used to obtain local distribution of ventilation defects, ventilation volume, and ADC of the gas which could be recalculated into the alveolar size. It should be mentioned, that HP lung MRI images have substantially higher SNR than ^{19}F lung MRI[60].

HP ^{3}He produces higher SNR than HP ^{129}Xe due to its higher gyromagnetic ratio[89]. HP ^{129}Xe can freely dissolve in the pulmonary blood and, therefore, be used to study gas transfer in the lungs and can be used for functional imaging of the highly perfused organs. A detailed discussion of HP ^{129}Xe imaging can be found in sections 1.7.3 and 1.7.4.

Overall, multinuclear MRI has become more and more popular over the last thirty years. Changing MRI signal source nuclei allowed researchers to transfer the MRI imaging from the field of mainly anatomical imaging into the area of functional imaging. Despite enormous development in the field, there are multiple challenges associated with different non-proton imaging techniques. The work presented in this thesis is focused on overcoming some of the challenges associated with ^{19}F and HP ^{129}Xe imaging.

1.4 Physics of Magnetic Resonance Imaging. Nuclear Magnetic Resonance

In order to facilitate the discussion of the MRI imaging methodologies developed in this thesis, the basic concepts of NMR are described in this section. For more details regarding the basic principles of MRI, the readers are referred to “MRI: The Basics, 2rd Edition” by Hashemi RH., et al.[90]. The readers who want to become familiar with advanced MRI principles and MRI physics are referred to “Magnetic Resonance Imaging: Physical Principles and Pulse Sequence Design” by Haacke et. al[91].

1.4.1 Nuclear Magnetic Moment and Magnetization

The nuclei with an odd number of protons and/or neutrons have intrinsic angular momentum given by:

$$\vec{J} = \hbar I, \qquad [1\text{-}1]$$

where $\hbar$ is the Dirac constant, and I is the nuclear spin. This angular momentum causes the nuclear magnetic moment:

$$\vec{\mu} = \gamma \vec{J}. \qquad [1\text{-}2]$$

Here, γ is gyromagnetic ratio, which physically characterizes the ratio of spin magnetic moment to the angular momentum and is unique for each nucleus. Since the vast majority of MRI techniques utilizes nuclei with a spin quantum number of ½, the ensuing discussion will pertain mainly to those nuclei. The gyromagnetic ratios of the most commonly used nuclei for MRI imaging are shown in Table 1-1.

Table 1-1: Gyromagnetic ratios of nuclei with ½ spin that are most commonly used for MRI imaging[1]

Nucleus	$\gamma, MHz \cdot rad \cdot T^{-1}$
^{1}H	267.519
^{19}F	251.818
^{129}Xe	-74.519
^{3}He	-202.814
^{31}P	108.291
^{13}C	67.262

Considering an arbitrary ensemble of N nuclei, it is convenient to describe its magnetic properties using the density of magnetic moments or magnetization. The magnetization of the spin system can be calculated as follows:

$$\vec{M} = \lim_{\Delta V \to 0} \frac{\sum_{i=1}^{N} \vec{\mu}}{\Delta V} \qquad [1\text{-}3]$$

This semi-classical approach is convenient for further discussion of the MRI physics. Once placed in an external magnetic field, the potential energy of the nuclear magnetic moment is defined as:

$$E = -\vec{\mu} \cdot \vec{B}_0; \qquad [1\text{-}4]$$

where $\vec{B}_0$ is the magnetic induction vector of the external magnetic field. Substituting Eq. [1-2] into Eq. [1-4], the following expression of the potential energy can be obtained:

$$E = -\gamma \hbar I B_0 \qquad [1\text{-}5]$$

The nuclear spin has a value of either ½ or -½. Therefore, in the presence of external magnetic field, the spin system can by described by two energy levels (Figure 1-1). The lower energy level (or "ground state") corresponds to the state in which the spin magnetic moment is aligned in parallel to the external magnetic field. On the contrary, the higher energy level is populated by nuclei with magnetic moment antiparallel to the external magnetic field. These two energy levels are degenerate in the absence of the external magnetic field. This physical phenomenon is known as Zeeman effect[41] or Zeeman energy level splitting. The energy gap between the two Zeeman levels is given by:

$$\Delta E = \gamma \hbar B_{0.} \qquad [1\text{-}6]$$

The spin population at each energy level obeys Boltzmann distribution:

$$N_i = N e^{-\frac{\Delta E}{kT}} \qquad [1\text{-}7]$$

where index *i* corresponds to the level number, *k* is Boltzmann's constant, and *T* is absolute temperature.

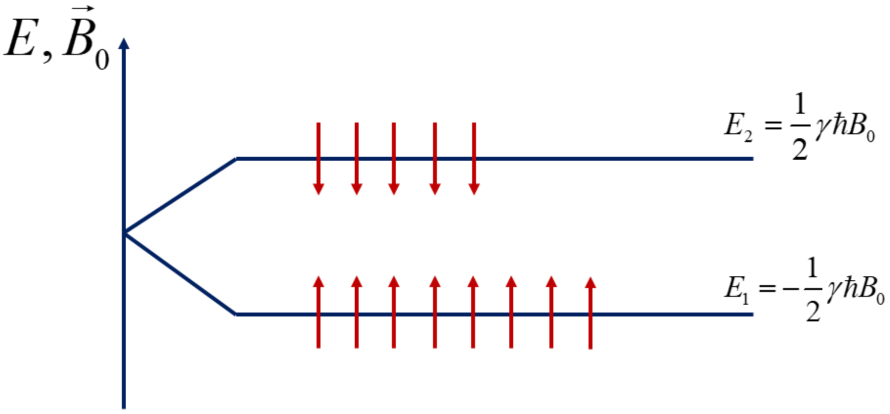

Figure 1-1: Energy diagram of the nuclear spins placed inside the external magnetic field.

It can be clearly seen that at the thermal equilibrium condition the ground state has an excess of spin population. The population difference can be expressed in terms of nuclear spin polarization:

$$P = \frac{N_1 - N_2}{N_1 + N_2} \qquad [1\text{-}8]$$

where N_1 is the number of spins in the ground state and N_2 is the number of spins in the higher energy state. Using the Boltzmann equation [1-8] and taking into account that $kT >> \hbar\gamma B_0$, the nuclear polarization can be calculated as follows:

$$P \approx \frac{\hbar\gamma B_0}{2kT} \qquad [1\text{-}9]$$

If we consider the conditions of normal body temperature and the presence of external magnetic field of 3T, the polarization of water protons in the body will be approximately 10^{-5}. The net magnetization can be expressed in terms of polarization in the following way:

$$\vec{M} = N_V \vec{\mu} P \approx \frac{N_V \hbar^2 \gamma^2 B_0}{4kT} \qquad [1\text{-}10]$$

where N_V is the number of nuclei per unit volume.

1.4.2 Magnetization dynamics in an external static magnetic field

In the presence of the external magnetic field, the magnetization vector experiences a torque:

$$\vec{\tau} = \vec{\mu} \times \vec{B}_0. \qquad [1\text{-}11]$$

which, by definition, is the change of angular momentum with time:

$$\frac{d}{dt}\vec{J}(t) = \vec{\mu}(t) \times \vec{B}_0(t). \qquad [1\text{-}12]$$

Multiplying Eq. [1-12] by the gyromagnetic ratio and taking into account Eqs. [1-2] and [1-3], the following equation which describes the dynamics of the net magnetization can be obtained:

$$\frac{d}{dt}\vec{M}(t)=\vec{M}(t)\times\gamma\vec{B}_0(t). \qquad [1\text{-}13]$$

It can be noted that the magnitude magnetization vector does not change with time according to Eq. [1-13]. The vector differential equation [1-13] can be rewritten as a system of scalar differential equations known as the phenomenological Bloch equations:

$$\begin{cases}\frac{d}{dt}M_x(t)=\gamma\left(M_y(t)B_z(t)-M_z(t)B_y(t)\right)\\ \frac{d}{dt}M_y(t)=\gamma\left(M_z(t)B_x(t)-M_x(t)B_z(t)\right)\\ \frac{d}{dt}M_z(t)=\gamma\left(M_x(t)B_y(t)-M_y(t)B_x(t)\right)\end{cases} \qquad [1\text{-}14]$$

Assuming $\vec{B}_0$ vector is aligned along the +z direction and translating to the complex variable $M_{xy}=M_x+iM_y$, the solution of system [1-14] can be obtained:

$$M_{xy}=\left(M_0\sin\theta\right)e^{-i\gamma B_0 t}, M_z=M_0\cos\theta \qquad [1\text{-}15]$$

where M_z is the projection of magnetization vector on the z axis and θ is the polar angle.

Overall, the solution [1-13] describes the precession of the net magnetization about the external magnetic field lines. The precession frequency, also known as Larmor frequency, can be calculated using the following equation:

$$\omega_0=\gamma B_0 \qquad [1\text{-}16]$$

The sign of gyromagnetic ratio determines the direction of the nuclear precession. If gyromagnetic ratio is positive, the magnetization precesses clockwise (for example, ^{1}H nuclei). On the contrary, the nuclei with a negative gyromagnetic ratio will experience counterclockwise nuclear precession (for example, ^{129}Xe nuclei). Since gyromagnetic ratio is unique property of each nucleus, the precession frequency will be unique as well.

1.4.3 Magnetization Dynamics in a Time-Varying Magnetic Field. NMR signal

In the previous section, we considered nuclear magnetization dynamics in the presence of the static external magnetic field. In order to understand the concept of NMR, the effect of a time-varying external magnetic field should be elaborated as well. Assuming the presence of an additional varying magnetic field $\vec{B}_1(t)$ which is orthogonal to the static magnetic field $\vec{B}_0$, the following expression can be written:

$$\vec{B}_1(t) = \left|\vec{B}_1\right| e^{-i\omega t}, \qquad [1\text{-}17]$$

Here, ω is the frequency of the time-varying magnetic field. Since $\vec{B}_1(t)$ field is rotating with frequency ω about z-axis, it is convenient to transform the laboratory frame of reference into a reference frame that rotates around the z axis at the same frequency. It is also convenient to calculate the net effective magnetic field as follows:

$$\vec{B}_{eff} = B_1\hat{i} + \gamma\left(\frac{B_0}{\gamma} - \omega\right)\hat{k}. \qquad [1\text{-}18]$$

It can be seen that, in the rotating frame of reference, $\vec{B}_1(t)$ is static along the abscissa, and the applicate component (z component) is reduced by a factor of ω/γ. If $\vec{B}_1(t)$ has frequency equal to the Larmor frequency, the effective magnetic field will be determined only by the time-varying magnetic field. Once the spin system described in 1.4.1 is placed in such a time-varying magnetic field, the electromagnetic energy will be absorbed by nuclei in the ground state. This energy will excite them to the upper energy level. Once the time-varying $\vec{B}_1(t)$ field is terminated, the excited nuclei will recover to the Boltzmann distribution through the emission of electromagnetic waves at their Larmor frequency. This effect is known as NMR.

Considering the perfect match between the Larmor frequency and the frequency of the varying external magnetic field, Eq. [1-13] can be written as follows:

$$\frac{d}{dt}\vec{M}(t) = \vec{M}(t) \times \gamma\vec{B}_1(t). \qquad [1\text{-}19]$$

Using the direct analogy with Eq. [1-13], the solution of [1-19] describes the rotation of the magnetization vector around the $\vec{B}_1$ vector. The rotation angle can be calculated using the following equation:

$$\theta = \int_0^\tau \gamma B_1(t)\,dt. \qquad [1\text{-}20]$$

As can be calculated from the γ values in Table 1-1, the Larmor frequency of the nuclei lies in a range of MHz radiofrequencies. Therefore, radiofrequency (RF) pulses are used to create the $\vec{B}_1(t)$ field in NMR and MRI. The RF pulses are frequently called by the rotation angle , or "flip angle" FA, of magnetization that they cause (for instance, a 90^{O} or 180^{O} pulse). After an RF pulse of FA θ has been applied, the magnetization vector position can be calculated by multiplying the initial vector by the rotation matrix:

$$\begin{pmatrix} M_x' \\ M_y' \\ M_z' \end{pmatrix} = \begin{pmatrix} 1 & 0 & 0 \\ 0 & \mathrm{Cos}\,\theta & \mathrm{Sin}\,\theta \\ 0 & -\mathrm{Sin}\,\theta & \mathrm{Cos}\,\theta \end{pmatrix} \begin{pmatrix} M_x \\ M_y \\ M_z \end{pmatrix}. \qquad [1\text{-}21]$$

Once the RF pulse is terminated, the magnetization rotation around the abscissa is terminated as well. However, the net magnetization vector is still precessing around the external static magnetic field. If an RF coil is placed orthogonal to the xy-plane (transverse plane), the precessing magnetization vector will produce a changing magnetic flux, Φ, through the coil contour. Since the coil surface is orthogonal to the transverse plane, only the M_{xy} component of magnetization will contribute to the Φ. The electromotive force induced in the coil provides a measurable NMR signal, also known as free induction decay (FID), and is given by Faraday's law of induction:

$$S(t) = -\frac{d\Phi(t)}{dt} = -\int_{V_s} \vec{B}_1(\vec{r})\cdot\left(\frac{d\vec{M}(\vec{r},t)}{dt}\right)dV, \qquad [1\text{-}22]$$

where $S(t)$ is the NMR signal in volts, $\vec{r}$ is radius vector, and V_s is a sample volume.

Taking into account that $\vec{M}(\vec{r},t)=\vec{M}(\vec{r})e^{-i\omega_0 t}$, Eq. [1-22] can be written as:

$$S(t)=i\omega_0 e^{-i\omega_0 t}\int_{V_s}\vec{M}(\vec{r})\vec{B}_1(\vec{r})dV. \qquad [1\text{-}23]$$

1.4.4 Spin-lattice Relaxation

Spin-lattice relaxation is the physical process that brings the spin system back to thermal equilibrium after excitation by the RF pulse. The spin system returns to thermal equilibrium through interaction with rapidly fluctuating magnetic fields induced by the random motions of magnetic moments. To account for spin-lattice (also known as longitudinal or T_1) relaxation, the magnetization dynamic equation should be modified as follows:

$$\frac{d}{dt}\vec{M}(t)=\gamma\left(\vec{M}(t)\times\vec{B}_0(t)\right)-\frac{M_z(t)-M_0}{T_1}\widehat{k}. \qquad [1\text{-}24]$$

In the rotating frame of reference in the absence of an RF pulse, Eq. [1-24] can be rewritten as:

$$\frac{dM_z}{dt}=-\frac{M_z-M_0}{T_1}, \qquad [1\text{-}25]$$

where $M_z(t)$ is the longitudinal magnetization (the applicate component of magnetization vector), T_1 is spin-lattice relaxation time constant, and M_0 is magnetization at thermal equilibrium. The solution of Eq. [1-25] describes the time evolution of longitudinal magnetization:

$$M_z(t)=M(0)e^{-\frac{t}{T_1}}+M_0\left(1-e^{-\frac{t}{T_1}}\right). \qquad [1\text{-}26]$$

M(0) is the magnetization at t=0 and itis determined by the FA of the applied RF pulse. Therefore, the spin-lattice relaxation of longitudinal magnetization can be described:

$$M_z(t) = M_0\left(1-(1-\cos\theta)e^{-\frac{t}{T_1}}\right). \qquad [1\text{-}27]$$

Generally speaking, T_1 relaxation time depends on the physical and chemical environment and can vary through the sample. Thus, the signal equation [1-23] must be modified to incorporate the effect of spin-lattice relaxation:

$$S(t) = i\omega_0 e^{-i\omega_0 t}\int_{V_s}\vec{M}(\vec{r})\vec{B}_1(\vec{r})\left(1-(1-\cos\theta)e^{-\frac{t}{T_1(\vec{r})}}\right)dV. \qquad [1\text{-}28]$$

The longitudinal magnetization dynamics following a 90^O RF pulse is demonstrated in Figure 1-2 for four different T_1 values: 50ms, 100 ms, 200 ms, and 300 ms.

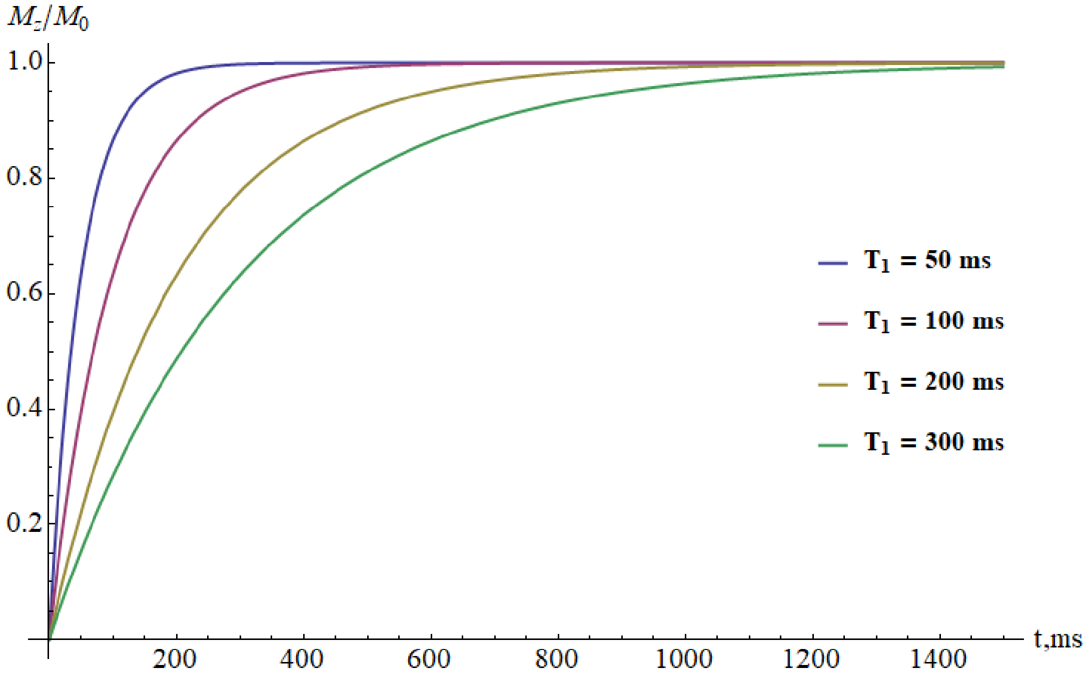

Figure 1-2. Longitudinal magnetization regrowth following a 90^O RF pulse for four different spin-lattice relaxation times.

From Figure 1-2 it is possible to notice that longitudinal magnetization fully recovers to thermal equilibrium after termination of a 90^O RF pulse in approximately $5T_1$. The exponential regrowth of the longitudinal component of net magnetization applies to all MRI that utilizes samples at thermal equilibrium. The difference in spin-lattice relaxation time of different tissues can be a source of MRI contrast.

1.4.5 Spin-Spin and Effective Spin-Spin Relaxation

Simultaneously with spin-lattice relaxation, the spin-spin relaxation (also known as transverse or T_2 relaxation) , causes decay of the magnetization component in a transverse plane. It originates from interaction between the magnetic moments of neighboring spins in the system. This interaction yields a loss in coherence between magnetic moments and thus in transverse magnetization destruction. After termination of the RF pulse, the evolution of transverse magnetization in the rotating frame of reference can be described by:

$$\frac{dM_{xy}}{dt} = -\frac{M_{xy}}{T_2}, \qquad [1\text{-}29]$$

where T_2 is the spin-spin relaxation time constant. The solution of Eq. [1-29] can be written as:

$$M_{xy}(t) = M(0)e^{-\frac{t}{T_2}}, \qquad [1\text{-}30]$$

where $M(0)$ is the transverse magnetization immediately following RF pulse termination. Besides direct spin-spin interaction, the inhomogeneities of the static magnetic field and the local differences in magnetic susceptibility of the sample contribute to transverse magnetization decay as well. Therefore, the transverse magnetization decay is characterized by effective, or apparent, spin-spin relaxation time (T_2^*) which is shorter than T_2 and is given by:

$$\frac{1}{T_2^*} = \frac{1}{T_2} + \frac{1}{T_2^B} + \frac{1}{T_{2,s}} \qquad [1\text{-}31]$$

where T_2^* is the effective spin-spin relaxation time constant, T_2^B is the transverse relaxation contribution from magnetic field inhomogeneities, and $T_{2,s}$ describes the contribution of local susceptibility differences of the sample. The difference between transverse magnetization decay caused by T_2 and T_2^* relaxation is exemplified in Figure 1-3.

Eq. [1-28] should be modified to include MRI signal decay owing to apparent spin-spin relaxation effects:

$$S(t) = i\omega_0 e^{-i\omega_0 t} \int_{V_s} \vec{M}(\vec{r})\vec{B}_1(\vec{r}) \left(1 - (1-\cos\theta) e^{-\frac{t}{T_1(\vec{r})}} \right) e^{-\frac{t}{T_2^*(\vec{r})}} dV \qquad [1\text{-}32]$$

Similar to spin-lattice effects, spin-spin relaxation varies as a function of coordinates and, therefore, can be used for MRI contrast generation.

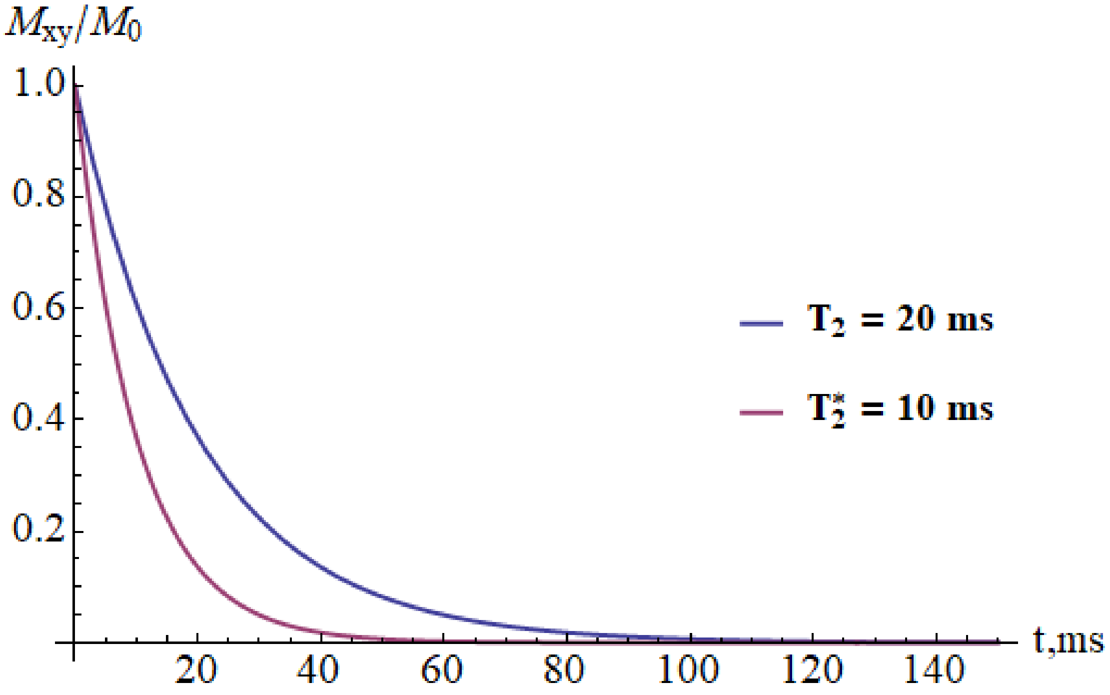

Figure 1-3. Transverse relaxation and apparent transverse relaxation following a 90^O RF pulse of an MRI sample.

1.4.6 Spatial localization of the MRI signal. Linear magnetic field gradients

Once generated, the MRI signal needs to be localized in order to acquire an MRI image. Spatial localization of the MRI signal is implemented through application of the linear gradients of the magnetic field. These gradients cause the spatial distribution of the Larmor frequencies resulting in specific frequency and phase encoding of the detected MRI signal. The magnetic field gradient vector is given as follows:

$$\vec{G}(\vec{r},t)=\frac{dB_z(t)}{dx}\hat{i}+\frac{dB_z(t)}{dy}\hat{j}+\frac{dB_z(t)}{dz}\hat{k}. \qquad [1\text{-}33]$$

Therefore, the magnetic field in the presence of the linear gradient can be expressed as follows:

$$\vec{B}(x,y,z)=B_0\hat{k}+\left(G_x x+G_y y+G_z z\right)\hat{k}. \qquad [1\text{-}34]$$

In general, the linear magnetic field gradients cause spatially distributed phase accumulation:

$$\Delta\varphi(\vec{r},t)=\gamma\int_0^t G(\vec{r},\tau)\cdot\vec{r}d\tau. \qquad [1\text{-}35]$$

It is useful to introduce *k*-space formalism in a similar way to the wave vectors:

$$\Delta\varphi(\vec{r},t)=2\pi\left(\vec{k}(t)\cdot\vec{r}\right)\Rightarrow\vec{k}(t)=\frac{\gamma}{2\pi}\int_0^t\vec{G}(\tau)d\tau. \qquad [1\text{-}36]$$

Taking into account Eq. [1-36], *k*-space can be interpreted as a space of the spatial frequencies. *k*-space is a conjugated space which can be transformed into the image space by Fourier transform.

The MRI signal can be expressed in terms of *k*-space formalism using the following equation:

$$S\left(\vec{k}\right)=i\omega_0 e^{-i\omega_0 t}\int_{V_S}\vec{M}(\vec{r})\cdot\vec{B}_1(\vec{r})\left(1-e^{-t/T_1(\vec{r})}\right)e^{-t/T_2^*(\vec{r})}e^{-i2\pi\left(\vec{k}\cdot\vec{r}\right)}dV. \qquad [1\text{-}37]$$

The MRI signal $S(t)$ becomes a function of the position in *k*-space and is gathered over the whole image space. Once the MRI signal is acquired, an MRI image can be reconstructed from the *k*-space using an inverse Fourier transform:

$$M_{eff}\left(\vec{r}\right)=\int_{k_s} S\left(\vec{k}\right)e^{2\pi i\left(\vec{k}\cdot\vec{r}\right)}dk, \qquad [1\text{-}38]$$

where $M_{eff}\left(\vec{r}\right)$ is an effective magnetization density that contains spin-lattice and spin-spin relaxations, RF magnetic field, and the phase effect. The effective magnetization now is a function of the image ("real") space and its distribution is represented as an MRI image.

In order to create a *k*-space prior to image reconstruction, MRI acquires data using specific sequences of RF pulses and magnetic field gradients. They are typically referred to as pulse sequences. A pulse sequence contains the information about the set of RF pulses, gradient waveforms, timing parameters, and signal sampling timing.

1.4.7 2D Gradient Echo Imaging Pulse Sequence

2D gradient echo (GRE) imaging pulse sequence shown in Figure 1 – 4 is one of the most commonly used MRI pulse sequences. The GRE pulse sequence can be divided into four separate parts: RF pulse, slice-selection, phase encoding, and frequency encoding.

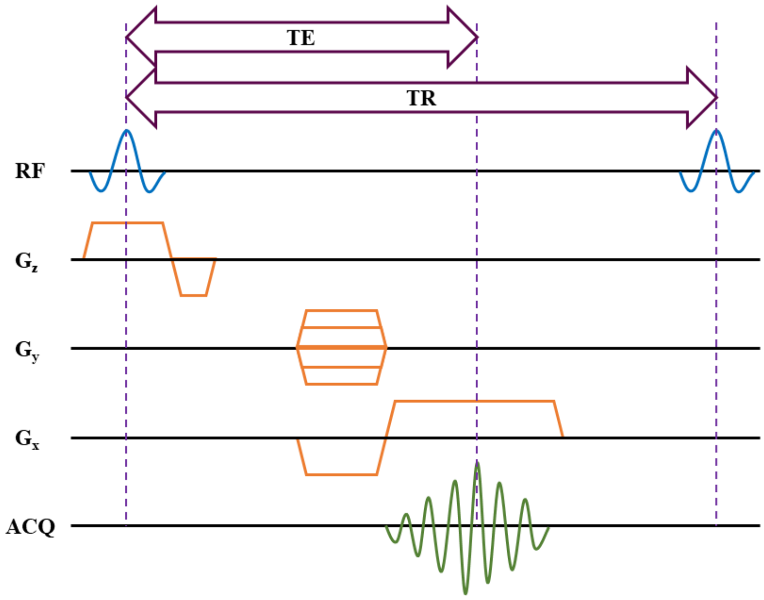

Figure 1–4. Pulse sequence diagram of 2D GRE. The repetition time and echo time are labeled.

Each pulse sequence begins with an excitation RF pulse to flip the longitudinal magnetization into the transverse plane. The time between two subsequent excitation RF pulses is called repetition time or TR. Although the flip angle θ can be arbitrary, there is a trade-off between the spin-lattice relaxation effect and the signal gain from using θ flip angle. The optimal flip angle for a given TR is given by Ernst angle equation:

$$\theta = \cos^{-1}\left(e^{-\frac{TR}{T_1}} \right). \qquad [1\text{-}39]$$

Use of the Ernst angle for the given TR allows SNR maximization. Each RF pulse can be characterized by associated bandwidth (BW) or range of processional frequencies that will be excited. The RF BW can be calculated by computing a Fourier transform of the RF pulse shape. If the RF spectrum of the pulse is infinite (as obtained with a rectangular RF pulse), the RF BW is associated with the frequency range containing approximately 95% of RF power. Although a RF pulse of arbitrary shape can be used, the excitation pulse is desired to have rectangular BW for accurate slice excitation. Therefore, a sinc-shaped RF pulse in the time domain is frequently used for spin excitation.

In order to excite a 2D slice of spins, the excitation pulse is initiated in the presence of a slice-select magnetic field gradient. The slice-select gradient is referred to as the z-gradient in Figure 1-4. Conventionally, the applicate axis (z axis) is aligned with the external magnetic field $\vec{B}_0$. There are three main slice orientations in the MRI depending on the slice-select gradient orientation: axial slice (gradient is applied along applicate), coronal (gradient is applied along abscissa), and sagittal (gradient is applied along ordinate). The thickness of the slice can be calculated using the following equation:

$$\Delta z = 2\pi \frac{BW_{ex}}{\gamma G_z}, \qquad [1\text{-}40]$$

where BW_{ex} is the excitation pulse bandwidth, and G_z is the strength of the slice-select gradient. Generally speaking, there are only two ways of adjusting the slice thickness: either changing RF excitation pulse BW or the strength of the slice-select gradient.

Following slice selection, the phase encoding is performed. On the pulse sequence diagram (PSD), phase encoding gradients are usually applied along ordinate axis (y direction). While the phase encoding gradient is on, the nuclear spins of the excited slice precess at the Larmor frequency which varies depending on spin location. This causes a phase accumulation and once the gradient is terminated, the spins retain the acquired phase. The position in *k*-space after phase encoding is given by:

$$k_y = \frac{\gamma}{4\pi}\left(T_p + t_f - t_s\right)G_y, \qquad [1\text{-}41]$$

where T_p is the duration of the phase encoding gradient, t_s is the time when the gradient strength reaches G_y, and t_f is the time when the current in the gradient coil is terminated. Eq. [1-41] assumes the trapezoidal gradient waveform which, in fact, is the most widely used in practice.

Conventional 2D GRE imaging acquires *k*-space data line-by-line (Cartesian trajectories). A single line of *k*-space is acquired during each repetition of the GRE pulse sequence. In order to do this, the phase encoding gradient strength is different during each repetition.

Following phase encoding, frequency encoding gradients are applied. The data acquisition (ACQ) is triggered in the presence of the frequency encoding gradient. Although frequency and phase encoding gradients are interchangeable, traditionally, the frequency encoding gradients are depicted along the *x*-axis on PSDs. The frequency encoding gradient in GRE starts with a negative lobe. It causes initial dephasing of the transverse magnetization. In order to create an echo, the following lobe of the frequency encoding gradient is positive with a twice larger area under the gradient waveform. The echo occurs during the readout where $k_x = 0$, and the time between the excitation pulse and the center of echo (maximum signal) is called the echo time (TE).

The field of view (FOV) of an MRI image can be calculated from the *k*-space data as:

$$FOV_{x,y} = \Delta k_{x,y}{}^{-1} \Rightarrow \begin{cases} FOV_y = \dfrac{2\pi}{\gamma \Delta G_y T_p} \\ FOV_x = \dfrac{2\pi}{\gamma G_x T_s} \end{cases}, \qquad [1\text{-}42]$$

where ΔG_y is the difference in the magnitude of G_y, and T_s is the signal sampling time.

The image resolution can be determined as follows:

$$\Delta x, y = \frac{1}{2k_{x,y}^{\max}}. \qquad [1\text{-}43]$$

1.4.8 Image SNR

One of the main characteristics of image quality is SNR. It is defined as the mean signal value divided by the standard deviation of the noise.

Noise in MRI is caused by the Brownian motion of electrons within the body's conducting tissue[92] and is described by the following equation[93,94]:

$$v_n = \sqrt{4kTR_s \Delta f}, \qquad [1.44]$$

where T is the sample temperature, R is the real part of the input impedance, and Δf is the frequency bandwidth. Taking into account Eqn. [1-37], MRI image SNR can be calculated as follows:

$$SNR = i \frac{\omega_0}{\sqrt{4kTR_s \Delta f}} e^{-i\omega_0 t} \int_{V_S} \vec{M}(\vec{r}) \cdot \vec{B}_1(\vec{r}) \left(1 - e^{-t/T_1(\vec{r})}\right) e^{-t/T_2^*(\vec{r})} e^{-i2\pi(\vec{k}\cdot\vec{r})} dV. \qquad [1.45]$$

The MRI signal is proportional to the Larmor frequency and, therefore, is proportional to B_0. In addition, the signal is proportional to the magnetization which, on its own, is proportional to the B_0 magnetic field. The combination of these two factors gives the B_0^2 dependance for the signal.

On the other hand, the frequency of the eddy currents which are caused by the Brownian motion of the body's electrons increases with increasing external magnetic field. Therefore, by Faraday's law of induction, the noise EMF increases in proportion to B_0. Thus, the image SNR should increase linearly with the strength of the external magnetic field.

In practice, however, in order to maintain the chemical shift effect at a constant number of pixels, the frequency encoding bandwidth is increased proportional to B_0 field[92]. Therefore, the image SNR increases only as $B_0^{1/2}$.

Generally speaking, the image SNR depends on numerous factors such as T_1, T_2^*, TR, TE and spin density. The SNR of the GRE image can be calculated as:

$$SNR \propto \frac{\left(1-e^{-TR/T_1}\right)e^{-TE/T_2^*}}{\left(1-\cos\theta e^{-TR/T_1}\right)}\sin\theta. \qquad [1\text{-}46]$$

On the other hand, the image SNR depends also on the voxel size and acquisition time as follows:

$$SNR \propto \Delta x \Delta y \sqrt{\frac{N_x N_y}{BW} NSA}, \qquad [1\text{-}47]$$

where $N_{x,y}$ is the number of phase encodings and readout points respectively, and NSA is the number of signal averages.

1.4.9 Chemical Shift Imaging

Chemical shift imaging (CSI) is one of the most commonly used localized spectroscopy techniques. CSI is also known as 2D spectroscopy MRI. The PSD of 2D CSI is shown on Figure 1-5. The main difference between 2D CSI and GRE imaging is the absence of the slice-select gradient. The RF pulse excites the entire MRI coil volume. Following the

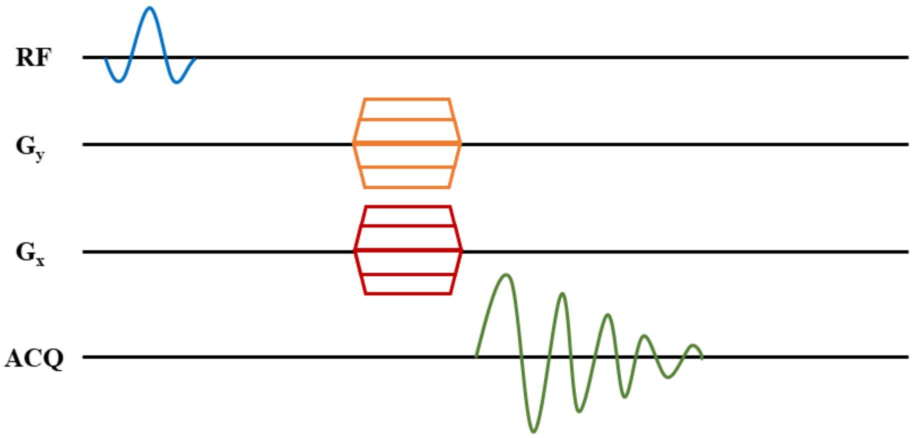

Figure 1-5. PSD of 2D CSI.

RF pulse, phase and frequency encoded gradients are applied in order to localize voxels in-plane. The FID is acquired, and the NMR spectrum is assigned for the localized voxel.

The main advantage of CSI over 2D GRE imaging is its superior sensitivity. In addition, because of the lack of a frequency encode gradient, the spectrum of the signal and the chemical shift information are preserved during CSI. Moreover, it is easier to detect the metabolites of drugs and to study drug metabolism in an organ with CSI. However, CSI images are slower to generate than GRE images of comparable resolution. Therefore, a separate CSI image can be reconstructed for each spectral component. A time series of CSI images allows one to evaluate the signal time evolution of different spectral peaks in different regions of the sample. This information reflects the metabolism of the compound which produces the tracked MRS spectral peak.

1.5 Arterial Spin Labeling MRI. Perfusion imaging

Arterial Spin Labeling (ASL) is an MRI technique used to assess the blood-flow and perfusion of internal organs[95–98]. This approach relies on the difference between spin-lattice relaxation of blood protons and tissue protons[97]. ASL requires acquisition of two MRI images subsequently. The first MRI image of the region of interest (ROI) is acquired using a conventional imaging pulse sequence without any modifications (“untagged” image). In order to acquire the second image, the initial selective 180^{O} RF inversion pulse is applied prior the excitation pulse. This inversion pulse is applied to a slice located closer to the heart compared to the ROI (a tagging region). The applied 180^{O} pulse inverts longitudinal magnetization of the arterial blood in the tagging region. Due to the spin-lattice relaxation, the longitudinal magnetization of the tagged blood grows back with time while flowing in the arteries to the ROI. The time delay between the inversion pulse and excitation pulse is chosen specifically to allow the tagged blood to reach the ROI and to allow the longitudinal magnetization of the arterial blood to reach approximately zero value. If the time delay is picked with high accuracy, the second "tagged" image of the ROI will have no contribution from the arterial blood washed-into the ROI. Therefore, the image acquired after subtraction of the "tagged" image from the "untagged" image represents the blood distribution throughout the ROI.

The obtained difference image can be recalculated into a perfusion image using the following equation[99]:

$$F = \frac{\Delta M e^{-TE \cdot R_{2b}}}{-2\alpha M_{0b}} \Big/ \left\{ \begin{array}{l} \left[e^{-wR_{1b}} - e^{\left(\min(\delta - w, 0) - \delta\right) R_{1b}} \right] e^{-TE \cdot R_{2b}} / R_{1b} + \\ +e^{-\delta R_{1b}} \left\{ \begin{array}{l} \dfrac{e^{-wR_{1t}}}{R_{1t}} \left[1 - e^{\min(\delta - \tau, 0) R_{1t}} \right] + \\ + \dfrac{1}{R_{1t}} \left[e^{\min(\delta - w, 0) R_{1t}} - e^{-wR_{1t}} \right] \end{array} \right\} e^{TE \cdot R_{2t}} \end{array} \right\}, \quad [1\text{-}48]$$

where ΔM is the measured difference in the MRI image signals, R_{ib} is the relaxation rate of blood, R_{it} is relaxation rate of tissue, α is labeling efficiency, δ is arterial transit time, w is post labeling delay time, and M_{0b} is an equilibrium longitudinal magnetization of the arterial blood. Eq. [1-48] illustrates one of the main issues associated with ASL perfusion images, which is the high number of parameters that influence the resulting image.

Usually, the signal difference ΔM is only a few percent for perfusion imaging[100]. Therefore, ASL perfusion imaging requires high NSA to ensure sufficient SNR of the resulting image. Moreover, there are technical difficulties associated with achieving complete saturation of the arterial blood in the "tagging" area. Although significant improvement in perfusion imaging was achieved with the invention of pseudo-continuous ASL (pCASL)[101–103], there are still multiple challenges in the field of ASL perfusion imaging, such as sensitivity to a motion[104], the lack of consensus about tagging strategy[103], complexity of the ASL perfusion model[103], and high sensitivity to the proton signal variation in the background signal[105].

1.6 Blood Oxygenation Level Dependent MRI. Hemodynamic Response and functional imaging of the human brain

Conventional proton MRI is sensitive to changes in blood oxygenation. This phenomenon is called Blood Oxygenation Level Dependence (BOLD)[106,107] and has been used to detect human brain function[108] as well as renal oxygenation[109].

BOLD imaging relies on the magnetic differences between oxyhemoglobin and deoxyhemoglobin[107]. Paramagnetic deoxyhemoglobin facilitates dephasing of the surrounding water spins and decreasing the apparent spin-spin relaxation. By contrast, the diamagnetic oxyhemoglobin does not affect the surrounding spins and causes no difference in T_2^* relaxation. Therefore, the MRI signal near the blood vessel with highly oxygenated blood will be higher compared to the same vessel containing deoxygenated blood. The main application of the BOLD effect is functional magnetic resonance imaging (fMRI) of the human brain. fMRI detects the change in the local blood-flow oxygenation in the activation regions of the human brain as well as changes in cerebral blood flow caused either by brain stimulation (conventional fMRI) or by the high regional oxygen metabolism (resting state fMRI).

If the brain region is stimulated, it will require a higher amount of oxygen in order to function properly. Therefore, the local blood flow will be increased in the area nearby the stimulated brain region, yielding a higher concentration of oxyhemoglobin compared to the resting state. This phenomenon of local blood flow increase as a result of regional brain activation is known as hemodynamic response (HDR)[110]. HDR is also known to be well correlated with neuronal activity and detection of the HDR during the brain stimulation can indicate directly the brain areas involved in the processing of the stimulus[110]. Therefore, the main aim of the fMRI is detection and localization of hemodynamic response.

In order to detect HDR, BOLD imaging is conducted. Taking into account the small difference in MRI signal caused by oxygenation change, conventional BOLD fMRI requires enormously high NSA. Furthermore, to validate the regional signal pile-up, BOLD fMRI requires calculation of statistical significance for the detected signal change. Only areas in which p value was estimated to be lower than the significance threshold will be considered as “activated”. Therefore, conventional BOLD fMRI utilizes the acquisition of a high number of scans during the resting state, with subsequent multiple image acquisitions during the stimulation. Although there are multiple different experimental designs for BOLD fMRI, the most commonly used are block design, event-related design, and mixed task design[111]. The schematic representation of these task designs is shown in Figure 1-6. During the block design the subject is exposed to a continuous stimulation during some amount of time (usually about 20-30 s) followed by the resting state for the same period of time. The stimulus/rest block is alternated during the fMRI study. Event-related task design can be described as repeated single activation events over the fMRI scan separated by the relatively long resting periods. Finally, mixed study design is a combination of the previous two.

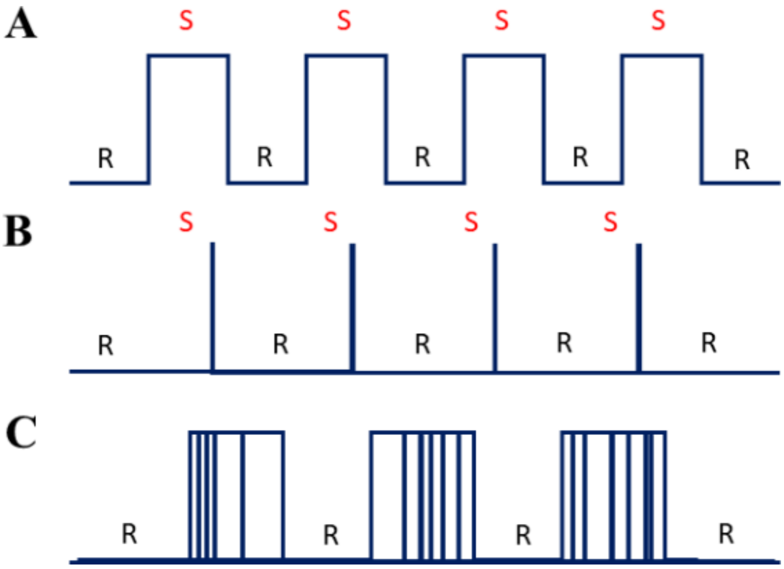

Figure 1–6. The most commonly used task designs for fMRI: A) block design; B) event-related design; C) mixed design. Red letters S demonstrate activation of stimulus, whereas black letters R represent resting state.

The BOLD signal change during an fMRI experiment is given by the Davis model[112]:

$$\frac{\Delta S}{S_0} = M\left\{1-\left(\frac{CMRO_2}{CMRO_2|_0}\right)^{\beta}\left(\frac{CBF}{CBF_0}\right)^{\alpha-\beta}\right\}, \qquad [1\text{-}49]$$

where $CMRO_2$ is the cerebral metabolic rate of oxygen consumption, CBF is the cerebral blood flow, α and β are numerical parameters, and M is a calibration parameter. Index 0 represents the parameters of the resting state. It can be seen that both blood flow and oxygenation contribute to the formation of the BOLD fMRI signal. The percent signal change due to the BOLD effect strongly depends on the external field strength[112] and does not exceed 10%[113].

It was observed that percent change of cerebral oxygen consumption is substantially lower compared to percent CBF change in response to brain stimulation[113–115]. Taking into account the low overall BOLD signal, the direct detection of HDR using ASL blood flow imaging was developed as another fMRI approach[112,116,117]. This ASL approach of fMRI demonstrated up to 50% signal enhancement[116], completely outperforming BOLD fMRI. Other advantages of the ASL-based fMRI approach are low sensitivity to susceptibility effect, possibility of signal quantification, and more accurate signal localization[117]. However, ASL-based fMRI has lower temporal resolution and lower image SNR compared to BOLD fMRI[117]. Therefore, ASL-based fMRI demonstrates better results with event-related task design.

Currently, BOLD fMRI is the commonly used fMRI technique since it is easy to implement on any MRI scanner without substantial RF and gradient pulse programming.

1.7 Hyperpolarized Noble Gas MRI

Conventional MRI utilizes NMR signals from thermally polarized nuclei. Thermally polarized nuclei have an extremely low value of polarization (~10^{-5} for protons in the body). Therefore, in order to achieve a signal level high enough to conduct MRI imaging, the imaged nuclei must have higher gyromagnetic ratio and high natural abundance. Furthermore, the concentration of signal nuclei in the sample must be sufficient. In order to increase the MRI signal even further, the population of polarized nuclei must somehow be increased beyond that at thermal equilibrium. This metastable state with high nuclear spin polarization is called the hyperpolarized (HP) state. The use of HP nuclei in MRI was first demonstrated by Albert et. al. in 1994[118].

In order to facilitate the discussion of the HP MRI imaging techniques developed in this thesis, the basic concepts of HP MRI are described in this section. There are two different techniques to create the HP state: spin exchange optical pumping (SEOP), metastable exchange optical pumping, and dynamic nuclear polarization (DNP). DNP is mainly used to produce HP ^{13}C and metastable exchange optical pumping is used to produce HP ^{3}He, therefore, will not be discussed here since this thesis is focused on use of HP ^{129}Xe gas. For more details regarding the basic principles of HP noble gas MRI, the readers are referred to "Hyperpolarized and Inert Gas MRI: From Technology To Application In Research And Medicine" by Albert and Hane[119].

1.7.1 Spin Exchange Optical Pumping

SEOP is the approach which allows production of HP noble gases with a sufficiently high level of polarization. HP metastable state is produced due to angular moment transition from circularly polarized laser light to alkali metal (AM) vapor with subsequent transfer of polarization from AM electrons to the noble gas nuclei. Although any AM can be used for SEOP, the most commonly used metal is rubidium (Rb) due to its low melting point, high spin-exchange cross-section for AM/noble gas, and the availability of high-power and narrow-bandwidth lasers tunable to the D_1 transition.

The initial stage of the SEOP is polarization of the s-shell of AM. The scheme of this process is shown in Figure 1-7 for the case of Rb vapor. The noble gas, rubidium vapor, and quenching gas (usually nitrogen) are confined in the polarization chamber. The circularly polarized light induces transition from the ground state $5S_{1/2}$ to the first excited state $5P_{1/2}$ of the AM. The selection rule indicating the possible electron transition is $\Delta m = \pm 1$, where m is magnetic quantum number. The left circularly polarized light induces transition from spin-down ground substate into spin-up excited substate (shown by red arrow in Figure 1-7). The right circular polarization will induce transition from the spin-up ground substate into spin-down excited substate. Once the electron is excited, it will relax back to the initial ground state. Collisions with noble gas atoms rapidly equalize the population of the $5P_{1/2}$ sublevels. Once excited, the electrons of the AM relax back to the ground state. This transition occurs in accordance with the selection rule mentioned above.

However, to facilitate the polarization of AM vapor, the polarization chamber contains quenching N_2 gas. Due to collisions with N_2 molecules, the electron transition between the

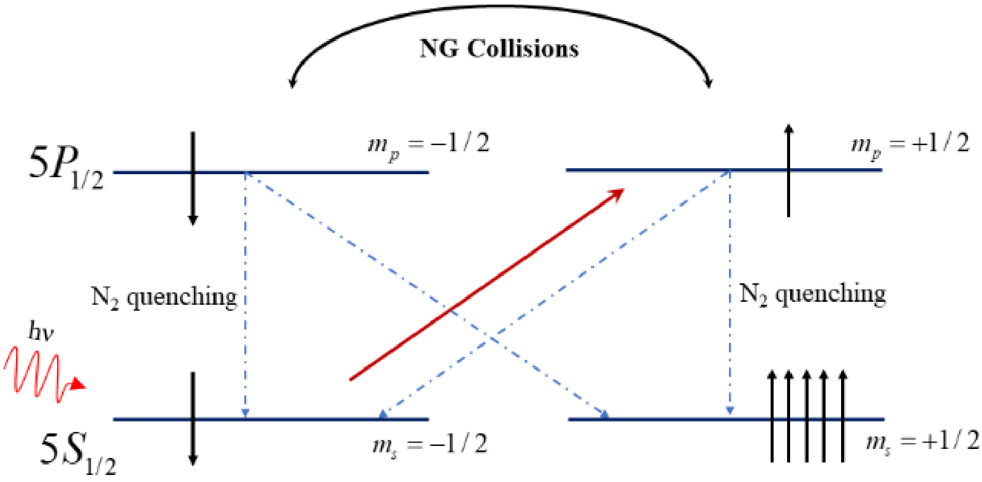

Figure 1-7. The transition scheme of Rb electrons during the SEOP process. The red arrow indicates the transition caused by circularly polarized light absorption.

excited state and the ground state of the same spin orientation are induced. The processes described above continue until all of the AM vapor becomes spin-polarized.

Once the AM vapor is spin-polarized, the angular momentum can be transferred from the s-shell electrons of AM to the noble gas nuclei through hyperfine Fermi interaction. The spin-exchange process can occur either through two-body or three-body non-elastic collisions. Two body collision is a dominant process at the higher noble gas pressures (~760 Torr). The spin exchange in this case happens during collisions between AM atoms and noble gas. On the contrary, at low pressures (~10-100 Torr), the dominant mechanism of spin-exchange appears to be creation of van der Waals molecules from AM and noble gas atoms. Although van der Waals molecules are destroyed due to collisions with N_2 molecules, their lifetime is long enough $(\geq ns)$ for efficient transfer of AM electron spin to the noble gas nuclei.

Overall, the probability of successful spin-exchange transfer is low due to often non-spin-conservative AM/noble gas interaction. Nevertheless, the polarization of AM vapor is rapidly restored due to constant irradiation of the chamber with circularly polarized photons. AM atoms with recovered spin polarization continue to interact with the remaining non-polarized noble gas molecules, increasing noble gas nuclear polarization over time.

1.7.2 Physical properties of HP nuclei. Imaging pulse sequences

Since HP is a non thermally-equilibrium state, the nuclear magnetic properties of the HP nuclei are dramatically different from those of thermally polarized nuclei.

As was discussed in section 1.4, spin-lattice relaxation brings the nuclear magnetization to the thermal equilibrium state. Therefore, it causes regrowth of the longitudinal magnetization with time. On the contrary, in case of HP nuclei, bringing the system to thermal equilibrium means decay of the longitudinal magnetization. The first term in Eq. [1-26] becomes dominant $\left(M(0) \gg M_0\right)$ due to the large population excess of one of the Zeeman levels, and the equation for T_1 relaxation can be written as follows:

$$M_z(t) = M(0)e^{-t/T_1}. \tag{1-50}$$

This T_1-associated exponential decay of longitudinal magnetization causes inapplicability of the conventional MRI imaging pulse sequences for HP imaging case.

Generally speaking, there are two approaches to HP imaging. The first is to use low FA excitation pulses for each line of k-space. This technique preserves longitudinal magnetization for further RF excitation. However, the MRI signal is significantly lower compared to the possible signal acquired following 90^{O} FA pulses. Furthermore, the loss of magnetization accumulates over the *k*-space trajectories, resulting in image blurring. In order to prevent blurring and image artifacts, variable FA can be used to compensate the signal loss between different *k*-space lines. On the other hand, if the FA is constant, each *k*-space trajectory can be corrected with respect to the magnetization loss due to the series of flip angles. This *k*-space correction overcomes the blurring issue as well.

Another HP image acquisition technique utilizes an initial 90^O excitation pulse. Once the first *k*-space trajectory is collected, magnetization is quickly tipped back to the z-axis for the next *k*-space line acquisition. The key advantage of this HP imaging technique is a substantial increase in image SNR as compared with low FA imaging. However, the spin-spin relaxation time of the HP media must be long relative to the acquisition time. This imaging approach also extremely sensitive to B_1 and B_0 inhomogeneities, resulting in image artifacts.

Due to the non-renewable nature of magnetization in the HP state, there is no need to use a long TR for image acquisition. Therefore, HP MRI scans are often fast and time efficient.

1.7.3 HP ^{129}Xe functional imaging of the lungs

The first demonstration of HP MRI imaging principles was done using ^{129}Xe gas. Over the whole history of HP MRI, ^{129}Xe remains the most popular and commonly used gas for preclinical and clinical HP MRI imaging.

HP ^{129}Xe is safe for inhalation. Although Xe is a general anesthetic agent, it can be safely inhaled if the total concentration of the ^{129}Xe gas in the lung is kept below 50%[120]. The most commonly used breathing protocol for HP ^{129}Xe, is a single breath-hold inhalation of 1L of HP ^{129}Xe[121–123]. This protocol keeps the lung concentration of ^{129}Xe below 50% and has no reported serious adverse effects.

The overall physical properties of HP ^{129}Xe are summarized in Table 1-2. The natural abundance of ^{129}Xe is 26% which is sufficient for human lung imaging. Images acquired after breath-hold initiation reveal the lung areas which are well-ventilated. Signal voids are caused by ventilation defects and lung obstructions. HP ^{129}Xe ventilation imaging allows calculation of ventilation volume and ventilation defect percentage (1 – ventilation volume) which are well-known biomarkers for pulmonary disorders. In addition to ventilation parameters, HP ^{129}Xe lung imaging is capable of probing the lung microstructure and alveolar size. This is typically done by HP ^{129}Xe DWI[124,125]. The resulting ADC of inhaled ^{129}Xe is used for regional calculation of the alveolar size, providing researchers with an important metric for lung microstructure.

Table 1-2: Physical properties of HP ^{129}Xe[2]

Nuclear spin	1/2
Gyromagnetic ratio, MHz·rad/T	-74.519
Natural abundance, %	26
Chemical shift range, ppm	250
T_1 in lungs, s	20
Ostwald solubility, L	0.17
Self-diffusion coefficient, cm^{2}s^{-1}	0.061

Due to relatively high Oswald solubility, HP ^{129}Xe freely dissolves in blood[126]. In addition, because of its large electron cloud, HP ^{129}Xe is highly sensitive to the change in physical and chemical environment, resulting in distinct chemical shift due to dissolution in blood and different tissues. Therefore, HP ^{129}Xe has been used to study gas transfer in the lungs. There are two different techniques capable of gas transfer assessment that are commonly used: chemical shift saturation transfer (CSSR), and xenon transfer contrast (XTC).

CSSR is an MRS technique which measures the average gas transfer time of HP ^{129}Xe from the gas phase through lung parenchyma into the alveolar blood[127]. The narrow BW 90^{O} saturation pulse is applied to the dissolved HP ^{129}Xe at the beginning of the CSSR sequence.

Since the HP state is non-recoverable, this initial RF pulse destroys the NMR signal from the dissolved ^{129}Xe. Due to the constant exchange between the gas phase and the dissolved phase, the signal of dissolved HP ^{129}Xe will recover after some time. This recovery time is measured and frequently called the transfer time. The measured HP ^{129}Xe transfer time was shown to correlate with lung parenchyma thickness[128] and was proposed as a biomarker for asthma[128], chronic obstructive pulmonary disorder[129], and radiation induced lung injury[130].

XTC images gas transfer through the acquisition of numerous time-resolved depolarization maps of the HP ^{129}Xe in the gas phase[131,132]. In the XTC experiment, multiple depolarization pulses are applied at the Larmor frequency of HP ^{129}Xe dissolved in blood and lung tissue. Similar to the CSSR experiment, some amount of HP nuclei from the gas phase will replace depolarized nuclei due to constant exchange between the gas phase and dissolved phase. This replacement results in gas phase signal depletion which is mapped during the XTC imaging. The produced depolarization map allows localization of lung tissue heterogeneity.

1.7.4 HP ^{129}Xe imaging of the brain

Functional imaging of the lungs remains the main practical application of HP ^{129}Xe MRI. However, once HP ^{129}Xe is dissolved in blood, it distributes to the highly perfused organs such as brain and kidneys. Therefore, it is possible to use HP ^{129}Xe as an inhalation contrast agent for imaging of highly perfused organs since HP ^{129}Xe has sufficiently long T_1 relaxation time in blood[133,134]. Furthermore, HP ^{129}Xe can be used for perfusion imaging as well... Since concentration of HP ^{129}Xe dissolved in blood is low[135,136], isotopically enriched HP ^{129}Xe is commonly used for imaging of the dissolved phase[122,123,137,138] in order to increase the image SNR significantly.

HP ^{129}Xe imaging of the human brain has been developed extensively over the past twenty years. Starting from the pioneering MRS experiments in animals[139–143], five spectral peaks were observed in the HP ^{129}Xe brain spectrum. Further spectroscopy studies in humans[137] confirmed findings of the animal experiments. The strongest peak at +198 ppm with respect to the gas phase was associated with grey matter. The spectral peak at +192 ppm originates from white matter. A peak at +188 ppm was associated with soft muscle tissue whereas the signal at +200 ppm originated from plasma. The last peak at +217 ppm was associated with HP ^{129}Xe dissolved in red blood cells (RBC).

The first HP ^{129}Xe image of the human brain was obtained in 2015.[144] Subsequently, the correlation between cerebral perfusion and HP ^{129}Xe signal in the brain was realized. The possibility of using HP ^{129}Xe brain imaging for cerebral perfusion imaging was demonstrated in healthy volunteers[145] and stroke patients[121]. However, HP ^{129}Xe imaging without appropriate image post-processing resulted only in qualitative agreement between the HP ^{129}Xe brain image and CBF images acquired with ASL.

In order to conduct quantitative perfusion imaging of the human brain, the dynamic acquisition of multiple images over the breath hold is required. This dynamic imaging approach was successfully implemented for imaging patients with Alzheimer's disease[122] for which the HP ^{129}Xe wash-out time was proposed as a potential biomarker. In addition, the dynamic imaging of HP ^{129}Xe dissolved in the brain was successfully used for quantitative imaging of the cerebral perfusion in healthy volunteers[123].

Most recently, HP ^{129}Xe brain imaging was shown to be capable of detecting the hemodynamic response to visual and motor stimuli and, thus, of conducting fMRI studies[123]. Despite the lower spatial resolution of HP ^{129}Xe fMRI compared to proton fMRI, the image acquisition time is substantially shorter making HP ^{129}Xe fMRI the fastest fMRI technique.

Despite numerous advances made in HP ^{129}Xe brain imaging, the technique remains extremely challenging. The major issue is associated with the low concentration (~1 μM[135]) of HP ^{129}Xe in the brain. In addition, this concentration tends to vary between subjects due to interpersonal pulmonological differences. This raises a question about the repeatability of HP ^{129}Xe brain imaging and makes image comparison between subjects difficult.

1.8 Thesis Outline

Chapter 1 has described the background of multinuclear MRI, its advantages over conventional proton MRI, and potential challenges. A brief overview of functional multinuclear MRI application was presented. The basic principles of MRI physics were presented as well as basic principles of HP MRI, followed by an overview of HP ^{129}Xe MRI for lung and brain imaging.

Chapters 2 through 4 are briefly described below; these chapters demonstrate work completed in partial fulfillment of the requirements for the degree of Doctor of Philosophy in Chemistry and Materials Science at Lakehead University.

Chapter 2 describes the application of ^{19}F CSI for the cancer resistivity detection to 5-fluorouracil chemotherapy. In this work, 2D ^{19}F CSI imaging was performed in groups of mice bearing two different types of human colorectal adenocarcinoma. By measuring the chemotherapy retention in the tumor, the resistive type of adenocarcinoma was successfully identified. This work was published in *Nature Scientific Reports* (peer-reviewed journal) in 2019.[86]

Chapter 3 discusses the potential of octafluorocyclobutane as an inhalation agent for ^{19}F lung MRI. In this work, octafluorocyclobutane was theoretically and experimentally compared to the most commonly used inert fluorinated inhalation agent – perfluoropropane. This study was conducted in a healthy rat cohort. Octafluorocyclobutane ventilation images demonstrated superior SNR compared to perfluoropropane images for both single breath-hold and continuous breathing protocols. This work was published in *Magnetic Resonance in Medicine* (peer-reviewed journal) in 2020.[72]

Chapter 4 describes the novel HP ^{129}Xe Time-of-Flight pulse sequence which is capable of measuring perfusion quantitatively. This imaging technique was tested on phantoms followed by imaging of healthy volunteers' brains. The mathematical model and the algorithm for image processing was developed as well. As an example of the application of the HP ^{129}Xe Time-of-Flight technique, the hemodynamic response to visual and motor stimuli was detected and correlated to proton BOLD fMRI images. All HP ^{129}Xe HDR maps correlated well with conventional fMRI images. This work was published in *Diagnostics* (peer-reviewed journal) in 2020.[123]

Chapter 5 provides a brief overall summary of my thesis work and discusses possible future advances and research directions.

1.9 References

1. Rumble, J. *CRC Handbook of Chemistry and Physics 101st Edition,2020-2021.*
2. Couch, M. *et al.* Inert fluorinated gas MRI: a new pulmonary imaging modality. *NMR Biomed.* **27**, 1525–1534 (2014).
3. Smith-Bindman, R., Miglioretti, D. L. & Larson, E. B. Rising use of diagnostic medical imaging in a large integrated health system. *Health Aff.* **27**, 1491–1502 (2008).
4. Bercovich, E. & Javitt, M. C. Medical Imaging: From Roentgen to the Digital Revolution, and Beyond. *Rambam Maimonides Med. J.* **9**, e0034 (2018).
5. Kubben, P. L. *et al.* Intraoperative MRI-guided resection of glioblastoma multiforme: a systematic review. *Lancet Oncol.* **12**, 1062–1070 (2011).
6. Quak, E. *et al.* F18-choline PET/CT guided surgery in primary hyperparathyroidism when ultrasound and MIBI SPECT/CT are negative or inconclusive: the APACH1 study. *Eur. J. Nucl. Med. Mol. Imaging* **45**, 658–666 (2018).
7. Haloua, M. H. *et al.* Ultrasound-guided surgery for palpable breast cancer is cost-saving: Results of a cost-benefit analysis. *Breast* **22**, 238–243 (2013).

8. Zhou, J. *et al.* Contrast-Enhanced Ultrasound Improves the Pathological Outcomes of US-Guided Core Needle Biopsy That Targets the Viable Area of Anterior Mediastinal Masses. *Biomed Res. Int.* **2018**, (2018).
9. Wu, M. H. *et al.* PET/CT-guided versus CT-guided percutaneous core biopsies in the diagnosis of bone tumors and tumor-like lesions: Which is the better choice? *Cancer Imaging* **19**, (2019).
10. Jayadevan, R. *et al.* Magnetic Resonance Imaging-Guided Confirmatory Biopsy for Initiating Active Surveillance of Prostate Cancer. *JAMA Netw. open* **2**, e1911019 (2019).
11. Contreras Ortiz, S. H., Chiu, T. & Fox, M. D. Ultrasound image enhancement: A review. *Biomed. Signal Process. Control* **7**, 419–428 (2012).
12. Dance, D. R., Christofides, S., Maidment, A. D. A., Mclean, I. D. & Ng, K. H. *Diagnostic Radiology Physics A Handbook for Teachers and Students*. (International Atomic Energy Agency, 2014).
13. Bushberg, J., Seibert, J., Leidholdt, E. & Boone, J. *The Essential Physics of Medical Imaging 2nd Edition*. (Lippincott Williams & Wilkins, 2002).
14. Ng, A. & Swanevelder, J. Resolution in ultrasound imaging. *Contin. Educ. Anaesthesia, Crit. Care Pain* **11**, 186–192 (2011).
15. Schreiber, J. J., Anderson, P. A., Rosas, H. G., Buchholz, A. L. & Au, A. G. Hounsfield units for assessing bone mineral density and strength: A tool for osteoporosis management. *J. Bone Jt. Surg. - Ser. A* **93**, 1057–1063 (2011).
16. Onishi, H. *et al.* Phantom Study of In-Stent Restenosis at High-Spatial-Resolution CT. *Radiology* **289**, 255–260 (2018).
17. Wathen, C. A. *et al.* In vivo X-ray computed tomographic imaging of soft tissue with native, intravenous, or oral contrast. *Sensors (Switzerland)* vol. 13 6957–6980 (2013).

18. Hoag, J. B., Fuld, M., Brown, R. H. & Simon, B. A. Recirculation of Inhaled Xenon Does Not Alter Lung CT Density. *Acad. Radiol.* **14**, 81–84 (2007).

19. Yonas, H., Darby, J. M., Marks, E. C., Durham, S. R. & Maxwell, C. CBF Measured by Xe-CT: Approach to Analysis and Normal Values. *J. Cereb. Blood Flow Metab.* **11**, 716–725 (1991).

20. Gur, D., Good, W. F., Wolfson, S. K., Yonas, H. & Shabason, L. In vivo mapping of local cerebral blood flow by xenon-enhanced computed tomography. *Science (80-.).* **215**, 1267–1268 (1982).

21. Smith-Bindman, R. *et al.* Radiation dose associated with common computed tomography examinations and the associated lifetime attributable risk of cancer. *Arch. Intern. Med.* **169**, 2078–2086 (2009).

22. Behzadi, A., Ung, Y., Lowe, V. & Deschamps, C. The role of positron emission tomography in the management of non-small cell lung cancer. *Can. J. Surg.* **52**, 235–42 (2009).

23. Chiotis, K. *et al.* Dual tracer tau PET imaging reveals different molecular targets for 11 C-THK5351 and 11 C-PBB3 in the Alzheimer brain. *Eur. J. Nucl. Med. Mol. Imaging* **45**, 1605–1617 (2018).

24. Yeo, S. K., Shepelytskyi, Y., Grynko, V. & Albert, M. S. Molecular Imaging of Fluorinated Probes for Tau Protein and Amyloid-β Detection. *Molecules (Basel, Switzerland)* vol. 25 3413 (2020).

25. Hane, F. T. *et al.* Recent Progress in Alzheimer’s Disease Research, Part 3: Diagnosis and Treatment. *J. Alzheimer’s Dis.* **57**, 645–665 (2017).

26. Bai, B., Ruangma, A., Laforest, R., Tai, Y.-C. & Leahy, R. M. Positron Range Modeling for Statistical PET Image Reconstruction. *IEEE Nucl. Sci. Symp.* **4**, 2501–2505 (2004).

27. Duncan, K. Radiopharmaceuticals in PET Imaging. *J Nucl Med Techno* **26**, 228–234 (1998).

28. Groch, M. W. & Erwin, W. D. SPECT in the Year 2000: Basic Principles. *J Nucl Med Technol* **28**, 233–244 (2000).

29. Van Patten, R., Greif, T., Britton, K. & Tremont, G. Single-photon emission computed tomography (SPECT) perfusion and neuropsychological performance in mild cognitive impairment. *J. Clin. Exp. Neuropsychol.* **41**, 530–543 (2019).

30. Spencer, S. S. *The Relative Contributions of MRI, SPECT, and PET Imaging in Epilepsy*. *Epilepsia* vol. 35 (1994).

31. Ito, H. *et al.* Database of normal human cerebral blood flow measured by SPECT: I. Comparison between 1-123-IMP, Tc-99m-HMPAO, and Tc-99m-ECD as referred with O-15 labeled water PET and voxel-based morphometry. *Ann. Nucl. Med.* **20**, 131–138 (2006).

32. Areses, P. *et al.* Molecular imaging techniques to study the biodistribution of orally administered 99mTc-labelled naive and ligand-tagged nanoparticles. *Mol. Imaging Biol.* **13**, 1215–1223 (2011).

33. Yang, Y. & Cui, M. Radiolabeled bioactive benzoheterocycles for imaging β-amyloid plaques in Alzheimer's disease. *Eur. J. Med. Chem.* **84**, 703–721 (2014).

34. Bauman, G. *et al.* Pulmonary Functional Imaging: Qualitative Comparison of Fourier Decomposition MR Imaging with SPECT/CT in Porcine Lung. *Radiology* **260**, 551–559 (2011).

35. Petersson, J. & Glenny, R. W. Imaging regional PAO2 and gas exchange. *J. Appl. Physiol.* **113**, 340–352 (2012).

36. Moser, E., Laistler, E., Schmitt, F. & Kontaxis, G. Ultra-High Field NMR and MRI—The Role of Magnet Technology to Increase Sensitivity and Specificity. *Front. Phys.*

5, 33 (2017).

37. Logothetis, N. K. What we can do and what we cannot do with fMRI. *Nature* **453**, 869–878 (2008).
38. Kruger, S. J., Fain, S. B., Johnson, K. M., Cadman, R. V. & Nagle, S. K. Oxygen-enhanced 3D radial ultrashort echo time magnetic resonance imaging in the healthy human lung. *NMR Biomed.* (2014) doi:10.1002/nbm.3158.
39. Partridge, S. C., Nissan, N., Rahbar, H., Kitsch, A. E. & Sigmund, E. E. Diffusion-weighted breast MRI: Clinical applications and emerging techniques. *Journal of Magnetic Resonance Imaging* vol. 45 337–355 (2017).
40. Lauterbur, P. C. Image formation by induced local interactions: Examples employing nuclear magnetic resonance. *Nature* **242**, 190–191 (1973).
41. Zeeman, P. The effect of magnetisation on the nature of light emitted by a substance. *Nature* **55**, 347 (1897).
42. Albert, M. S. *et al.* Biological magnetic resonance imaging using laser-polarized 129Xe. *Nature* **370**, 199–201 (1994).
43. Hajnal, J. *et al.* Use of fluid attenuation inversion recovery (FLAIR) pulse sequence in MRI of the Brain. *J. Comput. Assist. Tomogr.* **16**, 841–844 (1992).
44. Reeder, S. B. *et al.* Iterative decomposition of water and fat with echo asymmetry and least-squares estimation (IDEAL): Application with fast spin-echo imaging. *Magn. Reson. Med.* (2005) doi:10.1002/mrm.20624.
45. Hoh, H. B. *et al.* The stir sequence MRI in the assessment of extraocular muscles in thyroid eye disease. *Eye* **8**, 506–510 (1994).
46. Obert, A. J. *et al.* 1H-guided reconstruction of 19F gas MRI in COPD patients. *Magn. Reson. Med.* (2020) doi:10.1002/mrm.28209.
47. Couch, M. J. *et al.* Pulmonary ultrashort echo time 19F MR imaging with inhaled

fluorinated gas mixtures in healthy volunteers: feasibility. *Radiology* **269**, 903–9 (2013).

48. Couch, M. J. *et al.* Inert fluorinated gas MRI: a new pulmonary imaging modality. *NMR Biomed.* **27**, 1525–1534 (2014).

49. Wiesmann, F. *et al.* High-resolution MRI with cardiac and respiratory gating allows for accurate in vivo atherosclerotic plaque visualization in the murine aortic arch. *Magn. Reson. Med.* **50**, 69–74 (2003).

50. Garbow, J. R., Dugas, J. P., Song, S. K. & Conradi, M. S. A Simple, robust hardware device for passive or active respiratory gating in MRI and MRS experiments. *Concepts Magn. Reson. Part B Magn. Reson. Eng.* **21**, 40–48 (2004).

51. Santos-Díaz, A. & Noseworthy, M. D. Phosphorus magnetic resonance spectroscopy and imaging (31P-MRS/MRSI) as a window to brain and muscle metabolism: A review of the methods. *Biomed. Signal Process. Control* **60**, 101967 (2020).

52. Rijpma, A., van der Graaf, M., Meulenbroek, O., Olde Rikkert, M. G. M. & Heerschap, A. Altered brain high-energy phosphate metabolism in mild Alzheimer’s disease: A 3-dimensional 31P MR spectroscopic imaging study. *NeuroImage Clin.* **18**, 254–261 (2018).

53. Kemp, G. J., Meyerspeer, M. & Moser, E. Absolute quantification of phosphorus metabolite concentrations in human muscle in vivo by 31P MRS: A quantitative review. *NMR Biomed.* **20**, 555–565 (2007).

54. Mirkes, C. *et al.* 31P CSI of the human brain in healthy subjects and tumor patients at 9.4 T with a three-layered multi-nuclear coil: initial results. *Magn. Reson. Mater. Physics, Biol. Med.* **29**, 579–589 (2016).

55. Ren, J., Shang, T., Sherry, A. D. & Malloy, C. R. Unveiling a hidden 31 P signal coresonating with extracellular inorganic phosphate by outer-volume-suppression and

localized 31 P MRS in the human brain at 7T. *Magn. Reson. Med.* **80**, 1289–1297 (2018).

56. Liu, Y., Mei, X., Li, J., Lai, N. & Yu, X. Mitochondrial function assessed by 31P MRS and BOLD MRI in non-obese type 2 diabetic rats. *Physiol. Rep.* **4**, (2016).

57. Meyerspeer, M. *et al.* ^{31} P magnetic resonance spectroscopy in skeletal muscle: Experts' consensus recommendations. *NMR Biomed.* (2020) doi:10.1002/nbm.4246.

58. Niess, F. *et al.* Interleaved ^{31} P MRS/ ^{1} H ASL for analysis of metabolic and functional heterogeneity along human lower leg muscles at 7T. *Magn. Reson. Med.* **83**, 1909–1919 (2020).

59. Valkovič, L., Chmelík, M. & Krššák, M. In-vivo 31P-MRS of skeletal muscle and liver: A way for non-invasive assessment of their metabolism. *Anal. Biochem.* **529**, 193–215 (2017).

60. Couch, M. J. *et al.* 19F MRI of the Lungs Using Inert Fluorinated Gases: Challenges and New Developments. *J. Magn. Reson. Imaging* **49**, 343–354 (2018).

61. Kruger, S. J. *et al.* Functional imaging of the lungs with gas agents. *J. Magn. Reson. Imaging* **43**, 295–315 (2016).

62. Neal, M. A. *et al.* Optimized and accelerated 19F-MRI of inhaled perfluoropropane to assess regional pulmonary ventilation. *Magn. Reson. Med.* **82**, 1301–1311 (2019).

63. Neal, M. A., Pippard, B. J., Simpson, A. J. & Thelwall, P. E. Dynamic susceptibility contrast 19F-MRI of inhaled perfluoropropane: a novel approach to combined pulmonary ventilation and perfusion imaging. *Magn. Reson. Med.* **83**, 452–461 (2020).

64. Carrero-González, L., Kaulisch, T. & Stiller, D. In vivo diffusion-weighted MRI using perfluorinated gases: ADC comparison between healthy and elastase-treated rat lungs. *Magn. Reson. Med.* **70**, 1761–1764 (2013).

65. Jacob, R. E. *et al.* 19F MR imaging of ventilation and diffusion in excised lungs.

Magn. Reson. Med. **54**, 577–585 (2005).

66. Adolphi, N. L. & Kuethe, D. O. Quantitative mapping of ventilation-perfusion ratios in lungs by 19F MR imaging of T1 of inert fluorinated gases. *Magn. Reson. Med.* **59**, 739–746 (2008).

67. Halaweish, A. F. *et al.* Perfluoropropane gas as a magnetic resonance lung imaging contrast agent in humans. *Chest* **144**, 1300–1310 (2013).

68. Maunder, A., Rao, M., Robb, F. & Wild, J. M. Optimization of steady-state free precession MRI for lung ventilation imaging with 19F C3F8 at 1.5T and 3T. *Magn. Reson. Med.* **81**, 1130–1142 (2019).

69. Couch, M. J. *et al.* Fractional ventilation mapping using inert fluorinated gas MRI in rat models of inflammation and fibrosis. *NMR Biomed.* **29**, 545–552 (2016).

70. Kuethe, D. O., Scholz, M. D. & Fantazzini, P. Imaging inert fluorinated gases in cracks: perhaps in David's ankles. *Magn. Reson. Imaging* **25**, 505–508 (2007).

71. Wolf, U., Scholz, A., Heussel, C. P., Markstaller, K. & Schreiber, W. G. Subsecond fluorine-19 MRI of the lung. *Magn. Reson. Med.* (2006) doi:10.1002/mrm.20859.

72. Shepelytskyi, Y. *et al.* Evaluation of fluorine-19 magnetic resonance imaging of the lungs using octafluorocyclobutane in a rat model. *Magn. Reson. Med.* **85**, 987–994 (2020).

73. Pavlova, O. S. *et al.* 19F MRI of human lungs at 0.5 Tesla using octafluorocyclobutane. *Magn. Reson. Med.* (2020) doi:10.1002/mrm.28270.

74. Wolf, U. *et al.* Visualization of inert gas wash-out during high-frequency oscillatory ventilation using fluorine-19 MRI. *Magn. Reson. Med.* **64**, 1479–1483 (2010).

75. Srinivas, M., Heerschap, A., Ahrens, E. T., Figdor, C. G. & de Vries, I. J. M. 19F MRI for quantitative in vivo cell tracking. *Trends in Biotechnology* vol. 28 363–370 (2010).

76. Ahrens, E. T., Flores, R., Xu, H. & Morel, P. A. In vivo imaging platform for tracking

immunotherapeutic cells. *Nat. Biotechnol.* **23**, 983–987 (2005).

77. Hingorani, D. V. *et al.* Cell penetrating peptide functionalized perfluorocarbon nanoemulsions for targeted cell labeling and enhanced fluorine-19 MRI detection. *Magn. Reson. Med.* **83**, 974–987 (2020).
78. Fink, C. *et al.* Quantification and characterization of granulocyte macrophage colony-stimulating factor activated human peripheral blood mononuclear cells by fluorine-19 cellular MRI in an immunocompromised mouse model. *Diagn. Interv. Imaging* **101**, 577–588 (2020).
79. Fink, C. *et al.* Fluorine-19 Cellular MRI Detection of In Vivo Dendritic Cell Migration and Subsequent Induction of Tumor Antigen-Specific Immunotherapeutic Response. *Mol. Imaging Biol.* **22**, 549–561 (2020).
80. Parkins, K. M. *et al.* Cellular MRI reveals altered brain arrest of genetically engineered metastatic breast cancer cells. *Contrast Media Mol. Imaging* **2019**, (2019).
81. Parkins, K. M. *et al.* Multimodality cellular and molecular imaging of concomitant tumour enhancement in a syngeneic mouse model of breast cancer metastasis. *Sci. Rep.* **8**, 1–10 (2018).
82. Makela, A. V. & Foster, P. J. Imaging macrophage distribution and density in mammary tumors and lung metastases using fluorine-19 MRI cell tracking. *Magn. Reson. Med.* **80**, 1138–1147 (2018).
83. Reid, D. G. & Murphy, P. S. Fluorine magnetic resonance in vivo: A powerful tool in the study of drug distribution and metabolism. *Drug Discovery Today* vol. 13 473–480 (2008).
84. McIntyre, D. J. O. *et al.* Can localised 19F magnetic resonance spectroscopy pharmacokinetics of 5FU in colorectal metastases predict clinical response? *Cancer Chemother. Pharmacol.* **68**, 29–36 (2011).

85. Doi, Y., Shimmura, T., Kuribayashi, H., Tanaka, Y. & Kanazawa, Y. Quantitative 19F imaging of nmol-level F-nucleotides/-sides from 5-FU with T2 mapping in mice at 9.4T. *Magn. Reson. Med.* **62**, 1129–1139 (2009).

86. Shepelytskyi, Y. *et al.* In-Vivo Retention of 5-Fluorouracil Using 19F Magnetic Resonance Chemical Shift Imaging in Colorectal Cancer in a Murine Model. *Sci. Rep.* **9**, 13244 (2019).

87. Longley, D. B., Harkin, D. P. & Johnston, P. G. 5-Fluorouracil: mechanisms of action and clinical strategies. *Nat. Rev. Cancer* **3**, 330–338 (2003).

88. Couch, M. J. *et al.* Hyperpolarized and Inert Gas MRI: The Future. *Mol. Imaging Biol.* **17**, 149–162 (2015).

89. Svenningsen, S. *et al.* Hyperpolarized 3He and 129Xe MRI: Differences in asthma before bronchodilation. *J. Magn. Reson. Imaging* **38**, 1521–1530 (2013).

90. Hashemi, E., Hashman, R., William, G. & Christopher, J. *MRI:The Basics*. (Lippincott Williams & Wilkins, 2011).

91. Haacke, E., Brown, R., Thompson, M. & Venkatesan, R. *Magnetic Resonance Imaging: Physical Principles and Pulse Sequence Design*. (Wiley-Liss, 1999).

92. Redpath, T. W. Signal-to-noise ratio in MRI. *Br. J. Radiol.* **71**, 704–707 (1998).

93. Hoult, D. I. & Lauterbur, P. C. The Sensitivity of the Zeugmatographic Experiment Involving Human Samples. *J. Magn. Reson.* **34**, 425–433 (1979).

94. Ocali, O. & Atalar, E. Ultimate Intrinsic Signal-to-Noise Ratio in MRI. *Magn. Reson. Med.* **39**, 462–473 (1998).

95. Hartkamp, N. S., van Osch, M. J. P., Kappelle, J. & Bokkers, R. P. H. Arterial spin labeling magnetic resonance perfusion imaging in cerebral ischemia. *Curr. Opin. Neurol.* **27**, 42–53 (2014).

96. Gillis, K. A. *et al.* Non-Contrast Renal Magnetic Resonance Imaging to Assess

Perfusion and Corticomedullary Differentiation in Health and Chronic Kidney Disease. *Nephron* **133**, 183–192 (2016).

97. Günther, M. Perfusion Imaging. *J. Magn. Reson. Imaging* **40**, 269–279 (2014).
98. Odudu, A. *et al.* Arterial spin labelling MRI to measure renal perfusion: a systematic review and statement paper. *Nephrol. Dial. Transplant* **33**, ii15–ii21 (2018).
99. Wu, W.-C., St Lawrence, K. S., Licht, D. J. & Wang, D. J. J. Quantification Issues in Arterial Spin Labeling Perfusion Magnetic Resonance Imaging. *Top. Magn. Reson. Imaging* **21**, 65–73 (2010).
100. Golay, X. & Petersen, E. T. Arterial Spin Labeling: Benefits and Pitfalls of High Magnetic Field. *Neuroimaging Clin. N. Am.* **16**, 259–268 (2006).
101. Dai, W., Garcia, D., De Bazelaire, C. & Alsop, D. C. Continuous flow-driven inversion for arterial spin labeling using pulsed radio frequency and gradient fields. *Magn. Reson. Med.* **60**, 1488–1497 (2008).
102. Harteveld, A. A. *et al.* Comparison of multi-delay FAIR and pCASL labeling approaches for renal perfusion quantification at 3T MRI. *Magn. Reson. Mater. Physics, Biol. Med.* **33**, 81–94 (2020).
103. Nery, F., Gordon, I. & Thomas, D. Non-Invasive Renal Perfusion Imaging Using Arterial Spin Labeling MRI: Challenges and Opportunities. *Diagnostics* **8**, 2 (2018).
104. Petersen, E. T., Zimine, I., Ho, Y.-C. L. & Golay, X. Non-invasive measurement of perfusion: a critical review of arterial spin labelling techniques. *Br. J. Radiol.* **79**, 688–701 (2006).
105. Maleki, N., Dai, W. & Alsop, D. C. Optimization of background suppression for arterial spin labeling perfusion imaging. *Magn. Reson. Mater. Physics, Biol. Med.* **25**, 127–133 (2012).
106. Ogawa, S., Lee, T. M., Kay, A. R. & Tank, D. W. Brain magnetic resonance imaging

with contrast dependent on blood oxygenation. *Proc. Natl. Acad. Sci. U. S. A.* **87**, 9868–9872 (1990).

107. Ogawa, S., Lee, T. M., Nayak, A. S. & Glynn, P. Oxygenation-sensitive contrast in magnetic resonance image of rodent brain at high magnetic fields. *Magn Reson Med* **14**, 68–78 (1990).

108. Kim, S.-G. & Ugurbil, K. Comparison of Blood Oxygenation and Cerebral Blood Flow Effects in fMRI: Estimation of Relative Oxygen Consumption Change Seong-Gi Kim, Kamil Ugurbil. *Magn. Reson. Med.* **38**, 59–65 (1997).

109. Prasad, P. V. Functional MRI of the kidney: tools for translational studies of pathophysiology of renal disease. *Am J Physiol Ren. Physiol* **290**, F958–F974 (2006).

110. Johnson, S. C. *et al.* The Relationship between fMRI Activation and Cerebral Atrophy: Comparison of Normal Aging and Alzheimer Disease. *Neuroimage* **11**, 179–187 (2000).

111. Amaro, E. & Barker, G. J. Study design in fMRI: Basic principles. in *Brain and Cognition* vol. 60 220–232 (Academic Press, 2006).

112. Hare, H. V., Blockley, N. P., Gardener, A. G., Clare, S. & Bulte, D. P. Investigating the field-dependence of the Davis model: Calibrated fMRI at 1.5, 3 and 7T. *Neuroimage* **112**, 189–196 (2015).

113. Perthen, J. E., Lansing, A. E., Liau, J., Liu, T. T. & Buxton, R. B. Caffeine-induced uncoupling of cerebral blood flow and oxygen metabolism: A calibrated BOLD fMRI study. *Neuroimage* **40**, 237–247 (2008).

114. Mayhew, J. *et al.* Increased oxygen consumption following activation of brain: Theoretical footnotes using spectroscopic data from barrel cortex. *Neuroimage* **13**, 975–987 (2001).

115. Hoge, R. D. *et al.* Investigation of BOLD signal dependence on cerebral blood flow

and oxygen consumption: The deoxyhemoglobin dilution model. *Magn. Reson. Med.* **42**, 849–863 (1999).

116. Wang, J. *et al.* Arterial spin labeling perfusion fMRI with very low task frequency. *Magn. Reson. Med.* **49**, 796–802 (2003).

117. Borogovac, A. & Asllani, I. Arterial spin labeling (ASL) fMRI: Advantages, theoretical constrains and experimental challenges in neurosciences. *Int. J. Biomed. Imaging* **2012**, 818456 (2012).

118. Albert, M. S. *et al.* Biological Magnetic Resonance Imaging Using Laser-Polarized 129Xe. *Nature* **370**, 199–201 (1994).

119. Albert, M. S. & Hane, F. T. *Hyperpolarized and Inert Gas MRI From Technology To Application In Research And Medicine*. (Elsevier, 2017).

120. Luttropp, H. H., Thomasson, R., Dahm, S. & Persson, J. Clinical experience with minimal flow xenon anesthesia. *Acla Anaesihessiol Scand* **38**, 121–125 (1994).

121. Rao, M. R. *et al.* Assessment of brain perfusion using hyperpolarized 129Xe MRI in a subject with established stroke. *J. Magn. Reson. Imaging* **50**, 1002–1004 (2019).

122. Hane, F. T. *et al.* Inhaled Xenon Washout as a Biomarker of Alzheimer's Disease. *Diagnostics* **8**, E41 (2018).

123. Shepelytskyi, Y. *et al.* Hyperpolarized 129Xe Time-of-Flight MR Imaging of Perfusion and Brain Function. *Diagnostics* **10**, 630 (2020).

124. Ouriadov, A. *et al.* Lung morphometry using hyperpolarized 129Xe apparent diffusion coefficient anisotropy in chronic obstructive pulmonary disease. *Magn. Reson. Med.* **70**, 1699–1706 (2013).

125. Kirby, M. *et al.* Hyperpolarized 3He and 129Xe MR imaging in healthy volunteers and patients with chronic obstructive pulmonary disease. *Radiology* **265**, 600–10 (2012).

126. Chang, Y. V. MOXE: A model of gas exchange for hyperpolarized 129Xe magnetic

resonance of the lung. *Magn. Reson. Med.* **69**, 884–890 (2013).

127. Driehuys, B. *et al.* Imaging alveolar-capillary gas transfer using hyperpolarized 129Xe MRI. *Proc Natl Acad Sci U S A* **103**, 18278–18283 (2006).

128. Qing, K. *et al.* Assessment of lung function in asthma and COPD using hyperpolarized 129Xe chemical shift saturation recovery spectroscopy and dissolved-phase MRI. *NMR Biomed.* **27**, 1490–1501 (2014).

129. Kern, A. L. *et al.* Regional investigation of lung function and microstructure parameters by localized 129 Xe chemical shift saturation recovery and dissolved-phase imaging: A reproducibility study. *Magn. Reson. Med.* **81**, 13–24 (2019).

130. Fox, M. S. *et al.* Detection of radiation induced lung injury in rats using dynamic hyperpolarized ^{129} Xe magnetic resonance spectroscopy. *Med. Phys.* **41**, 072302 (2014).

131. Ruppert, K., Brookeman, J. R., Hagspiel, K. D. & Mugler, J. P. Probing lung physiology with xenon polarization transfer contrast (XTC). *Magn. Reson. Med.* **44**, 349–357 (2000).

132. Dregely, I. *et al.* Multiple-exchange-time xenon polarization transfer contrast (MXTC) MRI: Initial results in animals and healthy volunteers. *Magn. Reson. Med.* **67**, 943–953 (2012).

133. Albert, M. S., Kacher, D. F., Balamore, D., Venkatesh, A. K. & Jolesz, F. A. T 1 of 129 Xe in Blood and the Role of Oxygenation. *J. Magn. Reson.* **140**, 264–273 (1999).

134. Albert, M. S., Balamore, D., Kacher, D. F., Venkatesh, A. K. & Jolesz, F. A. Hyperpolarized 129XE T1 in oxygenated and deoxygenated blood. *NMR Biomed.* **13**, 407–414 (2000).

135. Kilian, W., Seifert, F. & Rinneber, G. Dynamic NMR spectroscopy of hyperpolarized 129Xe in human brain analyzed by an uptake model. *Magn. Reson. Med.* **51**, 843–847

(2004).

136. Ruppert, K., Brookeman, J. R., Hagspiel, K. D., Driehuys, B. & Mugler, J. P. NMR of hyperpolarized 129Xe in the canine chest: Spectral dynamics during a breath-hold. *NMR Biomed.* **13**, 220–228 (2000).

137. Rao, M., Stewart, N. J., Norquay, G., Griffiths, P. D. & Wild, J. M. High Resolution Spectroscopy and Chemical Shift Imaging of Hyperpolarized 129 Xe Dissolved in the Human Brain In Vivo at 1.5 Tesla. *Magn. Reson. Med.* **75**, 2227–2234 (2016).

138. Chacon-Caldera, J. *et al.* Dissolved hyperpolarized xenon-129 MRI in human kidneys. *Magn. Reson. Med.* **83**, 262–270 (2019).

139. Swanson, S. D. *et al.* Brain MRI with Laser-Polarized 129Xe. *Magn. Reson. Med.* **38**, 695–698 (1997).

140. Swanson, S. D., Rosen, M. S., Coulter, K. P., Welsh, R. C. & Chupp, T. E. *Distribution and Dynamics of Laser-Polarized 129 Xe Magnetization In Vivo*. *Magn Reson Med* vol. 42 (1999).

141. Duhamel, G. *et al.* Xenon-129 MR Imaging and Spectroscopy of Rat Brain Using Arterial Delivery of Hyperpolarized Xenon in a Lipid Emulsion. *Magn. Reson. Med.* **46**, 208–212 (2001).

142. Nakamura, K. *et al.* 129Xe spectra from the heads of rats with and without ligation of the external carotid and pterygopalatine arteries. *Magn. Reson. Med.* **53**, 528–534 (2005).

143. Kershaw, J. *et al.* Confirming the existence of five peaks in129Xe rat head spectra. *Magn. Reson. Med.* **57**, 791–797 (2007).

144. Rao, M., Stewart, N., Norquay, G., Griffiths, P. & Wild, J. Imaging the human brain with dissolved xenon MRI at 1 . 5T. in *Intl. Soc. Mag. Reson. Med 23* (2015).

145. Rao, M. R., Stewart, N. J., Griffiths, P. D., Norquay, G. & Wild, J. M. Imaging Human

Brain Perfusion with Inhaled Hyperpolarized 129 Xe MR Imaging. *Radiology* **286**, 659–665 (2017).

Chapter 2: Detection of colorectal adenocarcinoma resistivity to 5-fluorouracil using fluorine-19 MRI

This topic has been elaborated in the following publication: **Shepelytskyi Y.**, Fox MS., Davenport K., Li T., Albert MS., Davenport E "***In-vivo*** **Retention of 5-Fluorouracil Using 19F Magnetic Resonance Chemical Shift Imaging in Colorectal Cancer in a Murine Model**" published in *Scientific Reports*, volume 9, Article number: 13244 (2019). The publication text is listed below.

In-Vivo Retention of 5-Fluorouracil Using 19F Magnetic Resonance Chemical Shift Imaging in Colorectal Cancer in a Murine Model

Yurii Shepelytskyi[1], Matthew S. Fox[2], Karen Davenport[3], Tao Li[4], Mitchell S. Albert[3,4,5,*] & Eric Davenport[6]

1. Chemistry and Materials Science program, Lakehead University, 955 Oliver Rd., Thunder Bay, ON, P7B 5E1, Canada.
2. Lawson Health Research Institute, 750 Base Line Road East, London, ON, N6C 2R5, Canada.
3. Thunder Bay Regional Health Research Institute, 980 Oliver Rd., Thunder Bay, ON, P7B 5E1, Canada.
4. Chemistry Department, Lakehead University, 955 Oliver Rd., Thunder Bay, ON, P7B 5E1, Canada.
5. Northern Ontario School of Medicine, 955 Oliver Rd., Thunder Bay, ON, P7B 5E1, Canada.
6. Thunder Bay Regional Health Science Centre, 980 Oliver Rd., Thunder Bay, ON, P7B 6V4, Canada.

*Correspondence and requests for materials should be addressed malbert1@lakeheadu.ca.

Abstract

Colorectal cancer is the third leading cause of cancer death worldwide. 5-Fluorouracil (5-FU) is one of the most commonly used chemotherapies for treatment of solid tumours, including colorectal cancer. The efficacy of treatment is dependent on tumour type and can only be determined six weeks after beginning chemotherapy, with only 40–50% of patients responding positively to the 5-FU therapy. In this paper, we demonstrate the potential of using Magnetic Resonance (MR) Chemical Shift Imaging (CSI) for in-vivo monitoring of 5-FU tumor-retention in two different colorectal tumour types (HT-29 & H-508). Time curves for 5-FU signals from the liver and bladder were also acquired. We observed significant differences ($p < 0.01$) in 5-FU signal time dependencies for the HT-29 and H-508 tumours. Retention of 5-FU occurred in the H-508 tumour, whereas the HT-29 tumour is not expected to retain 5FU due to the observation of the negative b time constant indicating a decline in 5FU within the tumour. This study successfully demonstrates that CSI may be a useful tool for early identification of 5-FU responsive tumours based on observed tumour retention of the 5-FU.

Introduction

Colorectal cancer is the third most common cause of cancer death worldwide according to the World Healthcare Organization[1] and is the second most commonly diagnosed cancer in Canada according to the Canadian Cancer Society[2]. Colorectal cancer is responsible for approximately 14% of new cancer cases and 12% of cancer deaths in Canada[3]. According to Canadian Cancer Statistics (2016), 7% of men and 6% of women are expected to develop colorectal cancer during their lifetimes[2]. Moreover, an increasing incidence of colorectal cancer among young adults in Canada has been observed[4].

5-Fluorouracil (5-FU) is one of the most widely used cytotoxic chemotherapies for treatment of a variety of solid tumours, including colorectal and breast cancer[5–9]. However, the treatment response rate (percentage of patients whose tumour shrinks or disappeared after treatment) for 5-FU based chemotherapy are relatively low[5,10]. Biochemical modulation of 5-FU has increased response rates up to 40–50%[5,11,12], while the influence on overall survival has been limited[8]. The improvement in overall survival was observed when 5-FU was modulated with irinotecan[13,14]. The current colorectal cancer mortality rates reflect – at least in part – resistance of individual tumours to 5-FU treatment. It has been clinically demonstrated that the "trapping phenomenon" (the half-life of drug in the tumour is longer than 20 minutes) correlates with the clinical effectiveness of 5-FU chemotherapy[15]. Thus, a method to detect the responsiveness of a tumor to 5-FU in the earliest stages of treatment (i.e., sooner than six weeks) may enable effective targeting of 5-FU therapy to responsive tumours and also may prevent unnecessary exposure to cytotoxic chemotherapy in patients with 5-FU resistant tumours.

It is hoped that early identification of 5-FU resistant colorectal tumours will enable oncologists to choose treatment strategies more likely to improve patient survival and minimize unnecessary morbidity.

Several previous studies using MRI were conducted using Diffusion-Weighted Imaging (DWI) for early detection of the treatment response in patients with colorectal cancer[16–18]. It was found that the increase in Apparent Diffusion Coefficient (ADC) of tissue water within the tumour was significantly higher in responders compared to non-responders[16]. Marugami et al. was able to distinguish responders from non-responders 9 days after the initiation of chemotherapy based on the ADC changes in liver methastasis[17]. However, patients already received two infusions of 5-FU. Similar result was obtained by Lavdas et al.[18]. Although these results can be considered as an early detection of the tumour response, there are several limitations associated with DWI. Due to power requirements, hardware limitations and other external factors DWI accuracy is limited and the image quality is low[19]. Furthermore, DWI image are often susceptible to various artifacts like ghosting, blurring, ringing, distortions etc[19,20].

It is hypothesized that the early monitoring of 5-FU retention at the site of colorectal tumours can indicate the tumour responsiveness to 5-FU chemotherapy. 5-FU metabolizes into fluorinated nucleotides (Fnuc) and α-fluoro-β-alanine (Fbal) that each display a different chemical shift (i.e., 5-FU and its metabolites have different resonant frequencies in the ^{19}F magnetic resonance (MR) spectrum[21–28]. All of them can be visualized using Magnetic Resonance Imaging (MRI). Chemical-Shift Selective images of 5-FU and its metabolites have been previously acquired in a rat model[22–25] and in a mouse model[26–28]. The high natural abundance (approximately 100%) and large gyromagnetic ratio of Fluorine-19 (^{19}F) lead to a strong observed signal of 5-FU. ^{19}F MRI is a non-invasive and non-ionizing imaging technique. Another significant benefit of using ^{19}F MRI is the absence of fluorinated compounds in the human body, thus there is no natural background signal. These characteristics together, make ^{19}F MRI a promising method for monitoring 5-FU retention immediately following a single chemotherapy treatment. This would be a significant improvement to the current method for evaluating the efficacy of chemotherapy based on the observation of reduced tumour size after prescribed chemotherapy treatment.

Chemical Shift Imaging (CSI) is an extension of MR spectroscopy (MRS), allowing metabolite information to be measured. This technique has already been used for imaging the small intestines of mice with orally administrated 5-FU[28]. Also, CSI has been used for imaging the liver of patients with colorectal cancer and breast cancer[29] and to study the metabolism of 5-FU in liver metastasis[30,31]. Although the metabolism of 5-FU was studied within tumours[27,28,32] and liver[29], the CSI imaging technique of 5-FU was not used for tumour resistivity detection. In addition, ^{19}F CSI of 5-FU was not implemented as a clinical diagnostic modality.

The purpose of this study was to determine if there were observable differences between the signal to noise ratio (SNR) from colorectal tumours that are insensitive (HT-29)[33,34] and sensitive (H-508)[35] to 5-FU administration as a function of time. Significant differences between SNR values allow us to infer the potential utility of ^{19}F CSI to detect resistance of colorectal cancer to 5-FU treatment and potentially guide clinical personalized medicine.

Results

A total of 23 mice were imaged: 9 mice with the HT-29 tumour (non-responder), 9 mice with the H-508 tumour (responder), and 5 mice with both tumour types. For each animal, the SNR from the tumour, bladder and liver voxels were calculated.

The obtained values were used for plotting the SNR time-dependence curves to detect the presence or absence of 5-FU retention in given tumours. If any organ or tumor was bigger than a single voxel, a mean value of the SNR from all voxels containing the organ or tumor was calculated and used in the subsequent analysis.

Figure 2-1 represents the ^{19}F CSI images acquired at 7.5(a & b) and 40 minutes (c & d) after bolus injection, superimposed on the ^{1}H scans for two representative mice. HT-29 tumour cells were injected into mouse 1 (Fig. 2-1a,c), whereas mouse 2 (Fig. 2-1b,d) received H-508 tumour cells. 19F SNR values higher than 50 (attributed to bladder uptake) were thresholded to create necessary contrast in tumour voxels between the images acquired at 7.5 and 40 minutes after bolus injection.

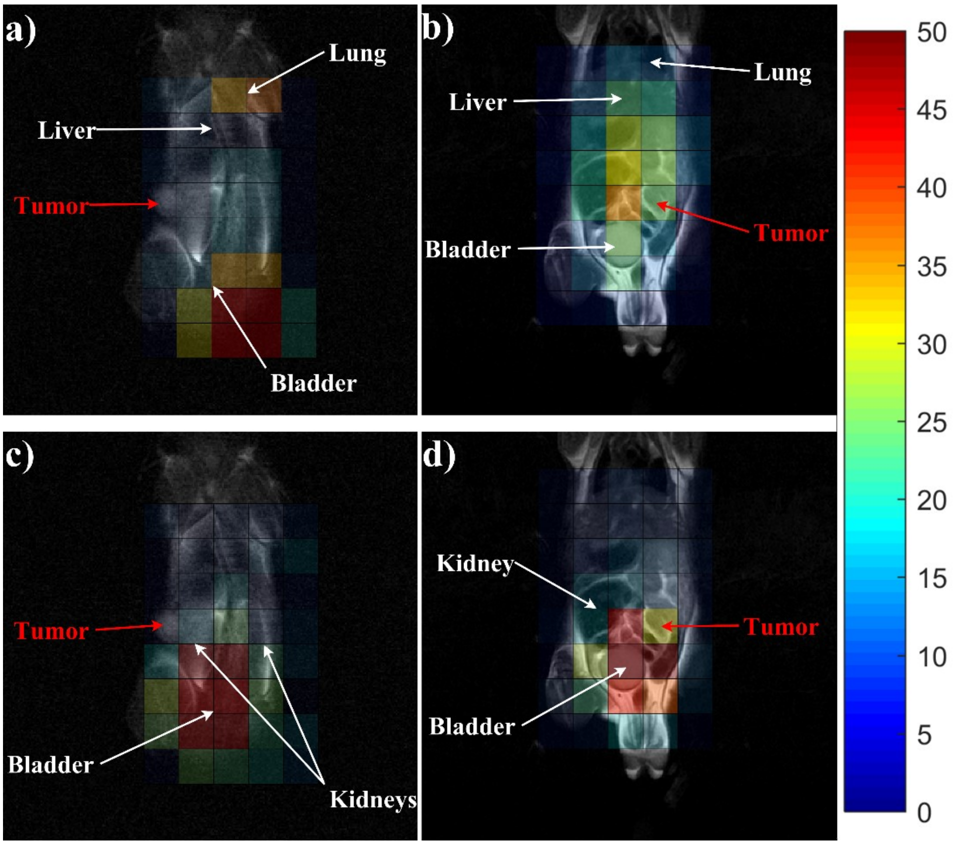

Figure 2 – 1. ^{19}F CSI superimposed onto ^{1}H localizer images. (a,c) represent ^{19}F CSI of the HT-29 (non 5-FU responsive) tumour mouse. (b,d) correspond to CSI of the H-508 (5-FU responsive) tumour mouse. The colour bar represents 5-FU SNR. (a,b) were acquired at 7.5 minutes after bolus injection, whereas (c,d) were acquired at 40 minutes after 5-FU injection. At 40 minutes, the signal was concentrated in the H-508 tumor, bladder and kidneys. Notice that the SNR from the H-508 tumour in (d) increased by 36% after 40 minutes.

The SNR of the HT-29 tumor was 9 at 7.5 minutes after injection (Fig. 2-1a). The SNR from the H-508 tumour voxel was 22.6 at the same time (Fig. 2-1b). After 40 minutes, the SNR value from the H-29 tumour decreased slightly and was equal to 7.2 (Fig. 2-1c), whereas the H-508 tumour SNR increased by 36% and was equal to 30.8 (Fig. 2-1d).

The liver SNR from the H-508 mouse decreased gradually from 17.8 to 8.3 throughout time. However, the SNR from the liver voxels in mouse 1 was equal to approximately 11 at 7.5 minutes after bolus and 10 at 40 minutes after injection. Bladder SNR was equal to 24.7 and 25.7 for mouse 1 and mouse 2 respectively at 7.5 minutes after injection. At the end of the time period, bladder SNR was equal to 86 for the HT-29 mouse and 58 for the H-508 mouse.

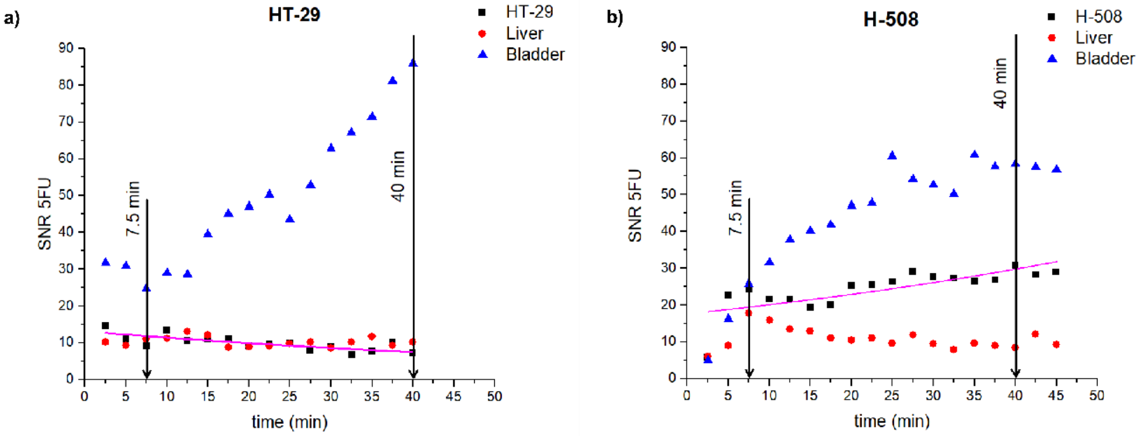

Figure 2 – 2. Time course of 5-FU SNR from the tumour, liver, and bladder voxels for representative mouse with a HT-29 tumour (a) and mouse with a H-508 tumour. (b) The HT-29 (non-responder) SNR steady decreased throughout the time interval (a), whereas SNR from the H-508 (tumor responder) voxel increased gradually. (b) The pink curve represents the exponential fit (Eq. [2-1]) of the tumour SNR curves.

Figure 2-2 illustrates the 5-FU SNR time dependences in the tumour, liver, and bladder voxels from representative images of HT–29 (Fig. 2-2a) and H-508 (Fig. 2-2b) tumours shown in Fig. 1-9. The HT-29 tumour SNR decreased steadily throughout time. On the contrary, the SNR from the H-508 tumour voxel grew gradually. The bladder signal steadily increased over time. The liver signal from the HT-29 mouse slightly oscillated around the mean value, which was equal to 10. However, the SNR of the liver voxels of mouse 2 significantly grew from 2.5 to 7.5 minutes after bolus. After 7.5 minutes, the SNR declined gradually.

Figure 2-3 shows the ^{19}F CSIs of mouse 3 superimposed on proton scans. This mouse had both tumour types. The HT-29 tumour was injected into the left flank of the animal whereas the H-508 colorectal adenocarcinoma was injected into the right flank. There are no liver voxels on these CSI images. ^{19}F SNR values higher than 50 were thresholded to visually create necessary contrast in tumor voxels between the figures acquired at different times.

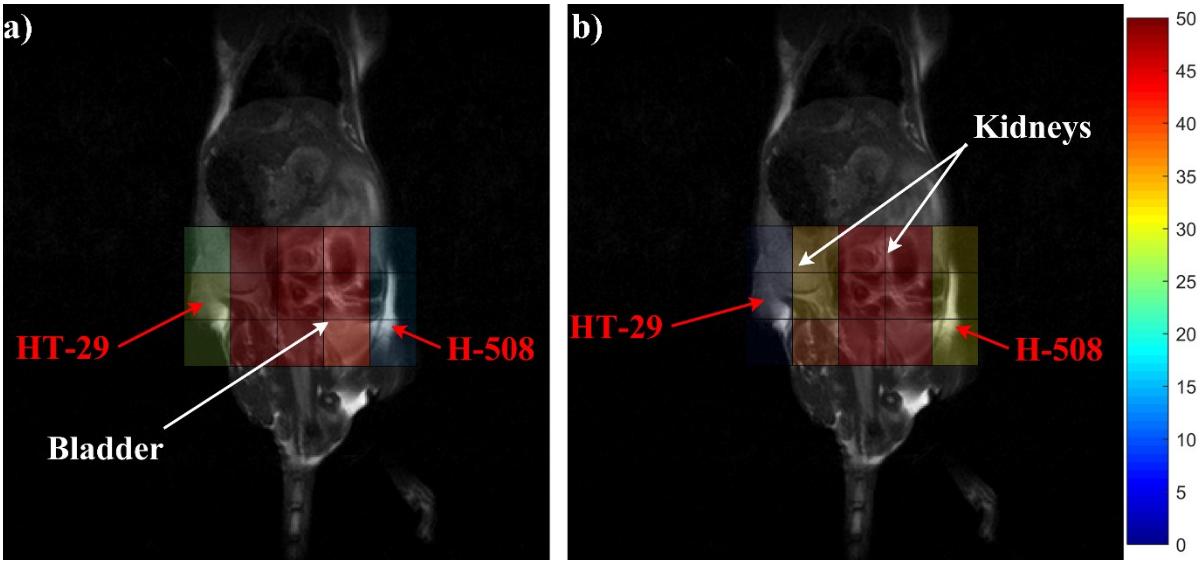

Figure 2-3. 19F CSI superimposed onto 1H localizer images. Images (a,b) show a representative mouse with both HT-29 (non 5-FU responsive, injected in the left flank of the animal) and H-508 (5-FU responsive, right flank) tumours at 5 and 70 minutes after 5-FU injection, respectively. The colour bar represents 5-FU SNR. After 70 minutes, high 5-FU signal was acquired from the H-508 tumour, kidneys and bladder. (b) Note that the H-508 SNR after 70 minutes was approximately two times higher than at the beginning of study, whereas HT-29 SNR dropped more than 3 times (b) comparing to the initial value (a).

Figure 2-3a,b were acquired at 5 and 70 minutes after bolus injection. The SNRs from the HT-29 and the H-508 voxels at 5 minutes after injection were 26.6 and 12.8 respectively (Fig. 2-3a). After 70 minutes, the SNR from the HT-29 tumor was 3.4-fold lower than the initial value and equal to 7.9. However, SNR from the H-508 tumour was equal to 31.1 at 70 minutes after bolus. The SNR from the bladder voxels in Fig. 2-3a was approximately 44, whereas after 70 minutes the SNR was 81.4, which is almost 2 times higher than the signal obtained at 5 minutes after the bolus (Fig. 2-3b).

Figure 2-4 shows the time curve evolution of SNR from both tumour types and the bladder. The HT-29 tumour signal increased during the first 10 minutes after 5-FU injection. Nevertheless, SNR decreased steadily throughout time from 10 to 70 minutes after bolus. On the contrary, the signal from the H-508 tumor increased gradually up to 22.5 minutes. The bladder signal grew steadily throughout the first 30 minutes and then leveled. The difference between the HT-29 and the H-508 SNR time curves was statistically significant according to

Wilcoxon signed rank test ($p < 0.01$). After 30 minutes, bladder time dependency plateaued at a value of 83 with minor oscillations.

All tumour SNR time curves were fitted using an exponential function with two fitting parameters – amplitude "a" and time constant "b" (Eq. [2-1]). One HT-29 tumour curve was excluded from analysis due to poor good- ness of fit. In one of the animals which was injected with both tumour types, the H-508 tumour was not detected. Therefore, just the HT-29 tumour curve was measured. Table 2-1 represents the values of the time constants "b" obtained for the HT-29 and H-508 singe-tumour mice. The values shown in Table 2-1 has been used for statistical evaluation of the obtained results. If the mean value of the observed time constants is positive and significantly different from a zero value, the tumour can successfully retain 5-FU.

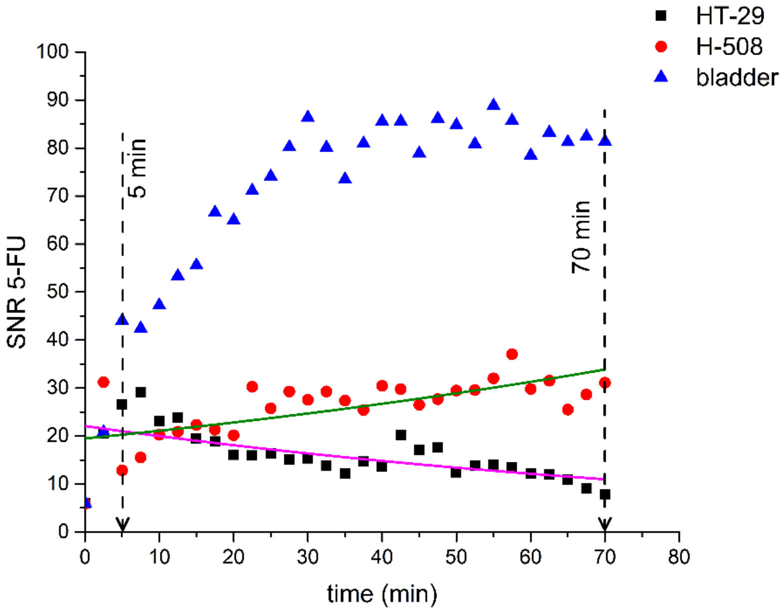

Figure 2-4. 5-FU SNR time curves from the HT-29 (left tumour) (Fig. 2-3a), the H-508 (right tumour) (Fig. 2-3b) and the bladder of representative mouse which had both tumor types. The pink and green curves correspond to the exponential fit of the HT-29 and H-508 SNR values respectively. Notice that the HT-29 (non 5-FU responsive tumour) SNR dropped gradually during time period from 10 to 70 minutes after bolus. On the contrary, the H-508 (5-FU responsive tumour) SNR grew steadily throughout the first 22.5 minutes.

Table 2-1. The time constants "b" (min^{-1}) obtained from the exponential fit of HT-29 and H-508 SNR time curves of single-tumour mice.

	HT-29	H-508
1	-0.014 ± 0.003	0.013 ± 0.006
2	-0.006 ± 0.005	0.028 ± 0.007
3	0.007 ± 0.004	0.013 ± 0.003
4	-0.011 ± 0.0004	0.044 ± 0.008
5	0.0003 ± 0.001	0.005 ± 0.006
6	0.009 ± 0.002	0.034 ± 0.008
7	-0.007 ± 0.003	0.011 ± 0.009
8	-0.006 ± 0.003	-0.002 ± 0.001
9	-0.012 ± 0.002	0.017 ± 0.003
Mean ± SD	-0.004 ± 0.008	0.018 ± 0.015

The mean value + /− one standard deviation of the time constants for the HT-29 tumour in single-tumor mice was equal to -0.004 ± 0.008 min^{-1}. On the contrary, the mean time constant "b" for the H-508 tumour was equal to 0.018 ± 0.015 min^{-1}. The results are significantly different according to two-sample unpaired t-test ($p < 0.01$). Furthermore, according to one-sample t-test, the mean value for the H-508 tumour is significantly greater than 0 ($p < 0.01$). Figure 2-5 shows a box chart analysis of time constants from both tumour types with a significant difference of $p < 0.01$ between the tumour types. Based on this statistical analysis, we can conclude that 5-FU uptake of studied tumors was significantly different.

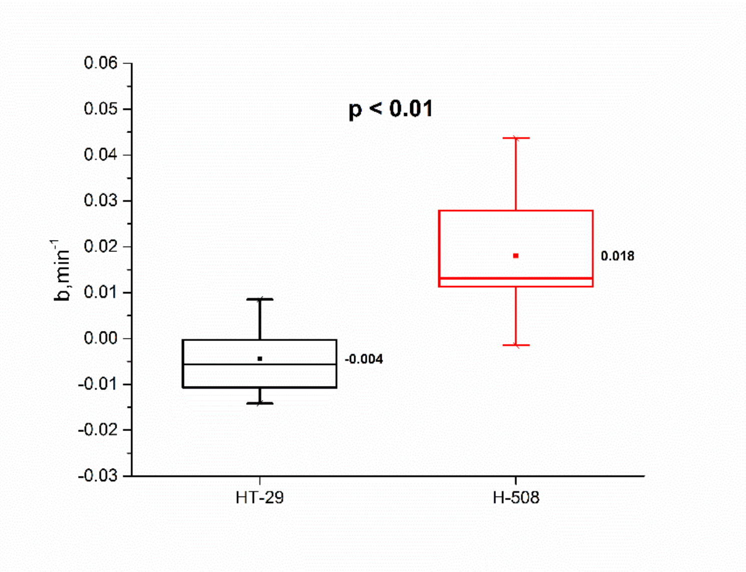

Figure 2–5. Box chart of the time constant for the HT-29 (non 5-FU responder) and the H-508 (5-FU trapper) tumours of single-tumour mice group. Mean value of the time constant for the HT-29 tumour was equal to -4×10^{-3} min^{-1}, however for the H-508 tumour mean time constant was equal to $18 \times 10^{-3}\text{min}^{-1}$.

The mean values of the time constant “b” for the H-508 and HT-29 tumors of dual-tumour cohort were equal to 0.006 ± 0.009 min^{-1} and -0.001 ± 0.008 min^{-1} respectively. The difference in mean values was not statistically significant ($p > 0.01$). However, the Wilcoxon test showed that SNR curves of two different tumours from the dual-tumour animals were significantly different ($p < 0.01$).

Discussion

The results of this study illustrate the feasibility of detecting a 5-FU retention in different types of colorectal cancers using ^{19}F CSI imaging. Time curves of the 5-FU signal acquired following bolus injection can reveal the difference in uptake of 5-FU in different tumour types. Time curves of the 5-FU signal acquired right after a bolus injection of the chemotherapy drug had different dynamics for two different types of human colon adenocarcinoma. Therefore, detection of tumour resistance to chemotherapy based on a 5-FU retention is possible approximately one hour after bolus injection.

5-FU SNR changes with time were found to be significantly different ($p < 0.01$) for the HT-29 and H-508 tumour types. Increasing 5-FU SNR throughout time is characteristic of the H-508 tumour, whereas the HT-29 tumour type SNR shows a tendency to decrease or to remain constant. This result was obtained for the single-tumor mice and it was statistically significant ($p < 0.01$). A significant difference between time constant “b” for the dual-tumour animals was not observed ($p > 0.01$). It could be due to a small number of samples ($n = 5$). These results are consistent with the literature which shows that the HT-29 tumor demonstrates resistivity to 5-FU therapy while the H-508 tumor can be treated using 5-FU[33–35].

We did not observe 5-FU “trapping phenomenon” as described by Presant during the studies timeline from both tumour types. For the H-508 type, the signal did not reach steady-state, so we were not able to estimate the half-life time for the 5-FU in the tumor. However, the retention of 5-FU in H-508 tumour was observed over the studied time course. The HT-29 tumour is not expected to retain 5-FU due to the observation of the negative b time constant indicating a decline in 5-FU within the tumour.

5-FU SNR within the bladder increased steadily from injection time to 70 minutes after treatment. Nearly all of the bladder 5-FU SNR was observed to be stronger than the tumour and liver SNRs. This finding could be due to catabolism of 5-FU in the liver. The limiting factor of 5-FU metabolism in the liver could be attributable to the activity of the enzyme dihydrouracil dehydrogenase[5,24]. Indeed, Fig. 2-2 illustrates the decay of the liver SNR with time. This time course corroborates the results, obtained in the rat model[32]. The control animals which received no cell injection had the same SNR dynamics for the liver and bladder.

Unfortunately, we were not able to observe the signals of 5-FU metabolites such as Fbal and Fnuc. 5-FU catabolizes into Fnuc in the tumour[5,27,32], whereas Fbal can be found in the liver, tumor, and kidneys[5,23,27,32]. According to Otake (2011), Fnuc signal was observed 1 hour after bolus and Fbal signal was detected 10 minutes after injection[32]. In that study, the authors used a 7.0T animal MRI system. The absence of a ^{19}F signal from the fluorinated metabolites could be due to the small concentration of these metabolites in the organs and tumours. Our study time interval was likely too short to allow for a high concentration of catabolites to be produced. Future imaging of the metabolites Fbal and Fnuc requires further parameter optimization due to the low SNR of these metabolites even 40 minutes after bolus. Additionally, to improve the sensitivity of the RF coil, a phased array coil could be used for better coupling with ^{19}F nuclei in the tumor and organs.

Overall, our studies demonstrate that 19F CSI imaging can be used to detect retention of 5-Fluorouracil in a murine model of colorectal cancer. This technique may extend prediction of patient tumour resistivity to 5-FU chemotherapy based on the pharmacokinetics of 5-FU at an early treatment stage, yielding an improvement in personalized cancer therapy. Implementing innovative imaging strategies that identify patients who respond to 5-FU would increase the efficacy of the treatment by allowing targeted matching of patients and chemotherapy agents in the neoadjuvant setting. This MRI-based technique could be readily implemented clinically as a means of non-invasively monitoring early response to 5-FU chemotherapy. Identifying resistant tumours early in cancer treatment will enable patients unlikely to respond to 5-FU therapy to rapidly alter treatment plans. The use of 19F CSI to triage patients into different chemotherapy regimens could be a significant innovation and alter routine clinical practice.

Materials and Methods

Cell lines and culture conditions

All human colon adenocarcinoma cell lines, media, sera, and culture reagents were obtained from ATCC (Burlington, ON, Canada), Life Technologies (Burlington, Ontario, Canada), Becton Dickinson (St. Laurent, Quebec, Canada) or Sigma (St. Louis, MO). HT-29 cells were grown in McCoy's 5 A medium and NCI-H508 were grown in RPMI-1640 medium, with both cell lines supplemented with 10% FBS, 100U/ml Penicillin, 100 μg/ml streptomycin, and 2 mM glutamine. Cells were grown to 50–75% confluency in T-75 flasks prior to injection into animals.

In Vivo cell implantation and tumour growth in immunodeficient mice

This study was approved by Lakehead University Animal Care Committee, and all procedures were done in compliance with the regulations of the Canadian Counsel on Animal Care (CCAC). HT-29 and NCI-H508 cells were grown in T-75 flasks between 60–80% confluency. Cells were trypsinized with 0.25% (w/v) Trypsin −0.53 mM EDTA solution, resuspended in appropriate medium, and counted. 1×10^6 human colon adenocarcinoma cells were mixed with a 1:1 ratio cold Matrigel (Corning Matrigel, Fisher Scientific) for each 100 μl bolus injection into 36–40 day-old male (Nu/Nu) nude mice. Briefly, nude mice were anesthetized using 3% isoflurane and injected with 100ul of a 1:1 cold Matrigel solution of either 1×10^6 HT-29 or NCI-H508 cells using a BD Eclipse 27 G × 1/2 needle. Mice were injected under the skin in the left (HT-29) or right flank (NCI-H508), weighed, labelled by ear piercing, and immediately returned to cages. Mock mice were injected similarly with 100 µl of a 1:1 ratio of appropriate cold medium and Matrigel while control mice received no injection. The H-508 tumour grew more slowly than HT-29. Therefore, the dual-tumour mice were injected with HT-29 tumor 5 days post HT-508 cells injection. A total of 23 mice were injected with either HT-29 cells (9 mice), H – 508 cells (9 mice) or both adenocarcinoma types (5 mice). All animal imaging was performed 12–16 days post injection or when a caliper measurement of the volume of the tumours did not exceed either 450 ± 75 mm^3 for animals with single tumours or 600 ± 75 mm^3 in total for the dual-tumour mice. The mouse body weight was between 30–37 g.

MRI acquisition

Prior to the MRI scanning procedure, all animals were anesthetized using 5% isoflurane oxygen mixture and anesthesia was maintained at 2% with oxygen during all subsequent experiments. Mice were catheterized using a MTV-01 tail-vein catheter (SAI Instruments). All animals received a slow bolus injection of 300 µl 5-FU (50 mg/ml) over the course of 2 minutes inside the magnet bore. During each MRI acquisition, animals were kept at 37 C° with a temperature-controlled water-filled blanket (T/Pump, Gaymar).

MRI was performed using a clinical Philips 3.0 T Achieva whole-body scanner, equipped with a custom-built dual-tuned $^1H/^{19}F$ quadrature birdcage coil. Proton localization was performed using a multi-slice T1-weighted Turbo Spin Echo (TSE) pulse sequence with a Field of View (FOV) of 75×75 mm^2, TR/TE = 2000/55.19 ms, slice thickness of 2 mm and Number of Signal Averages (NSA) = 3. Acquisition matrix size was equal to 256×256 which corresponds to the in-plane resolution of 0.29 mm. The total number of slices was equal to 16 for each mouse. Proton scans were used to determine the location of the tumour, bladder and liver.

After the bolus injection, ^{19}F CSI images were acquired for up to 70 minutes with a time step of 2 minutes and 30 seconds. Mice that had one tumour type were studied using CSI with 8×5 resolution, FOV of 20×50 mm^2 and NSA = 3, whereas mice with both tumour types were studied using 3×5 matrix, FOV equal to 31 × 18.6 mm^2 and NSA = 9. All CSI images were acquired using spectral bandwidth of 32 kHz (266 ppm at 3.0 T) and TR/ TE = 5000/4.27 ms. The data sampling number was 1024, yielding a spectral resolution of 0.26 ppm.

Images were analyzed using a custom imaging processing program written in MATLAB R2016b (The Mathworks, Inc, Natick, MA).

Statistical analysis

All SNR time curves were fitted by the exponential function:

$$SNR = ae^{bt}, \tag{2-1}$$

where amplitude a and time constant b were fitting parameters. The time constant determines signal dynamics. If the time constant is positive, the signal will grow with time, conversely when it is negative, signal will decrease. Thus, time constant can be used as an indicator of 5-FU kinetics. A two-sample t-test was applied for b time constant to analyze the statistical significance of the fitted results for the single tumour animals. A one-sample t-test was applied to the b time constant of each group of single tumour animals to evaluate if the mean b value of each group was significantly different from 0. A Wilcoxon signed rank test has been used to evaluate the difference between SNR time curves obtained from different tumors in dual-tumor animals. OriginPro 2016 was used to conduct statistical analysis (OriginLab Corp., Northampton, MA).

References

1. World Healthcare Organisation. Cancer. 2018. 1–7 Available at, http://www.who.int/mediacentre/factsheets/fs297/en/ (2018). 2. Colorectal cancer statistics - Canadian Cancer Society. Available at, http://www.cancer.ca/en/cancer-information/cancer-type/ colorectal/statistics/?region=on.

3. Canadian Cancer Statistics 2017 Special topic: Pancreatic cancer. Available at, http://www.cancer.ca/~/media/cancer.ca/CW/cancer information/cancer101/Canadian cancer statistics/Canadian-Cancer-Statistics-2017-EN.pdf?la=en.

4. Brenner, D. R. et al. Increasing colorectal cancer incidence trends among younger adults in Canada. *Prev. Med. (Baltim)* **105**, 345–349 (2017).

5. Longley, D. B., Harkin, D. P. & Johnston, P. G. 5-Fluorouracil: mechanisms of action and clinical strategies. *Nat. Rev. Cancer* **3**, 330–338 (2003).

6. Midgley, R. & Kerr, D. Colorectal Cancer. *Lancet* **353**, 391–399 (1999).

7. McIntyre, D. J. O. et al. Can localised 19F magnetic resonance spectroscopy pharmacokinetics of 5FU in colorectal metastases predict clinical response? *Cancer Chemother. Pharmacol.* **68**, 29–36 (2011).

8. Folprecht, G. et al. Efficacy of 5-fluorouracil-based chemotherapy in elderly patients with metastatic colorectal cancer: A pooled analysis of clinical trials. *Ann. Oncol* **15**, 1330–1338 (2004).

9. Launay, M. et al. Beating the odds: Efficacy and toxicity of dihydropyrimidine dehydrogenase-driven adaptive dosing of 5-FU in patients with digestive cancer. *Br. J. Clin. Pharmacol.* **81**, 124–130 (2016).

10. Arbuck, S. G. Overview of clinical trials using 5-fluorouracil and leucovorin for the treatment of colorectal cancer. *Cancer* **63**, 1036–44 (1989).

11. Odin, E., Sondén, A., Gustavsson, B., Goran, C. & Yvonne, W. Expression of Folate Pathway Genes in Stage III Colorectal Cancer Correlates with Recurrence Status Following Adjuvant Bolus 5-FU-Based Chemotherapy. *Mol. Med.* **21**, 597–604 (2015).

12. Souglakos, J. et al. FOLFOXIRI (folinic acid, 5-fluorouracil, oxaliplatin and irinotecan) vs FOLFIRI (folinic acid, 5-fluorouracil and irinotecan) as first-line treatment in metastatic colorectal cancer (MCC): A multicentre randomised phase III trial from the Hellenic Oncolog. *Br. J. Cancer* **94**, 798–805 (2006).

13. Saltz, L. B. et al. Irinotecan plus Fluorouracil and Leucovorin for Metastatic Colorectal Cancer. *N. Engl. J. Med.* **343**, 905–914 (2002).

14. Douillard, J. et al. Irinotecan combined with fluorouracil compared with fluorouracil alone as first-line treatment for metastatic colorectal cancer: a multicentre randomised trial. *Lancet* **355**, 1041–1047 (2000).

15. Presant, C. A. et al. Association of intratumoral pharmacokinetics of fluorouracil with clinical response. *Lancet* **343**, 1184–1187 (1994).

16. Jung, S. H. et al. Predicting response to neoadjuvant chemoradiation therapy in locally advanced rectal cancer: Diffusion-weighted 3 tesla MR imaging. *J. Magn. Reson. Imaging* **35**, 110–116 (2012).

17. Marugami, N. et al. Early detection of therapeutic response to hepatic arterial infusion chemotherapy of liver metastases from colorectal cancer using diffusion-weighted MR imaging. Cardiovasc. *Intervent. Radiol.* **32**, 638–646 (2009).

18. Lavdas, I. et al. Histogram analysis of apparent diffusion coefficient from whole-body diffusion-weighted MRI to predict early response to chemotherapy in patients with metastatic colorectal cancer: preliminary results. *Clin. Radiol.* **73**, 832.e9–832.e16 (2018).

19. Soujanya Chilla, G., Heng Tan, C., Xu, C. & Loo Poh, C. Diffusion weighted magnetic resonance imaging and its recent trend-a survey. *Quant Imaging Med Surg* **5**, 407–422 (2015).

20. Baliyan, V., Das, C. J., Sharma, R. & Gupta, A. K. Diffusion weighted imaging: Technique and applications. *World J. Radiol.* **8**, 785 (2016).

21. Wolf, W., Waluch, V. & Presant, C. A. Non-invasive 19F-NMRS of 5-fluorouracil in pharmacokinetics and pharmacodynamic studies. *NMR Biomed.* **11**, 380–387 (1998).

22. Lovis, J. A. et al. Monitoring in-vivo Absorption of 5-Fluorouracil by 19 F MRI: A Preliminary Study for Clinical Pharmacokinetics Using a Clinical MRI System. *In Proc. ISMRM* 2592.

23. Gade, T. P. F. et al. In vivo 5-fluorouracil and fluoronucleotide T1 relaxation time measurements using the variable nutation angle method. *Magn. Reson. Med.* **52**, 169–173 (2004).

24. Brix, G. et al. Mapping the Biodistribution and Catabolism of 5-Fluorouracil in Tumor-Bearing Rats by Chemical-Shift Selective 19F MR Imaging. *Magn. Reson. Med.* **34**, 302–307 (1995).

25. Brix, G., Bellemann, M. E., Haberkorn, U., Gerlach, L. & Lorenz, W. J. Assessment of the biodistribution and metabolism of 5-fluorouracil as monitored by 18F PET and 19F MRI: A comparative animal study. *Nucl. Med. Biol.* **23**, 897–906 (1996).

26. Doi, Y. et al. 19F Chemical Shift Imaging of F-nuc Formed from 5-FU in Mouse Tumor by Fast Spin Echo. In *Spatially Resolved Magnetic Resonance Methods, Materials, Medicine, Biology,Rheology, Geology, Ecology, Hardware* (eds Blümler, P., Blumich, B., Botto, R. & Fukushima, E.) 413–419 (Wiley-VCH Verlag GmbH, 1988).

27. Doi, Y., Shimmura, T., Kuribayashi, H., Tanaka, Y. & Kanazawa, Y. Quantitative 19F imaging of nmol-level F-nucleotides/-sides from 5-FU with T2 mapping in mice at 9.4T. *Magn. Reson. Med.* **62**, 1129–1139 (2009).

28. Kuribayashi, H., Doi, Y. & Kanazawa, Y. Application of (19)F chemical shift imaging in studies of mice with orally administered 5-fluorouracil. *Magn. Reson. Med.* **46**, 864–9 (2001).

29. Li, C.-W. et al. Quantitation of 5-Fluorouracil Catabolism in Human Liver in Vivo by Three-Dimensional Localized 19F Magnetic Resonance Spectroscopy 1. *Clin. Cancer Res.* **2**, 339–345 (1996).

30. Klomp, D. W. J., Van Laarhoven, H. W. M., Kentgens, A. P. M. & Heerschap, A. Optimization of localized 19F magnetic resonance spectroscopy for the detection of fluorinated drugs in the human liver. *Magn. Reson. Med.*, https://doi.org/10.1002/mrm.10527 (2003).

31. van Laarhoven, H. W. M. et al. Prediction of chemotherapeutic response of colorectal liver metastases with dynamic gadolinium- DTPA-enhanced MRI and localized 19F MRS pharmacokinetic studies of 5-fluorouracil. *NMR Biomed.*, https://doi.org/10.1002/ nbm.1098 (2007).

32. Otake, Y., Hirata, K., Soutome, Y. & Bito, Y. In-vivo 19 F Imaging of 5-Fluorouracil and its Metabolites in Rat by Two-Element Phased-Array Coil. In *Proc. Intl. Soc. Mag. Reson. Med.* **19** (2011).

33. Lesuffleur, T. et al. Resistance to high concentrations of methotrexate and 5-fluorouracil of differentiated HT-29 colon-cancer cells is restricted to cells of enterocytic phenotype. *Int. J. Cancer* **76**, 383–392 (1998).

34. Denise, C. et al. 5-Fluorouracil resistant colon cancer cells are addicted to OXPHOS to survive and enhance stem-like traits. *Oncotarg*et **6**, 41706–41721 (2015).

35. Park, J.-G. et al. Characteristics of cell lines established from human colorectal carcinoma. *Cancer Res*. **47**, 6710–6718 (1987).

Acknowledgements

This work was supported by a grant from the Northern Ontario Academic Medicine Association (NOAMA). Lakehead University and Thunder Bay Regional Health Research Institute provided partial support and access to their facilities. We acknowledge Iain Ball and Peter Smylie for their contributions to the initial phases of this research. Yurii Shepelytskyi was supported by Ontario Graduate Scholarship.

Author Contributions

Y.S. and M.S.F. contributed equally to this work. Y.S. contributed to image reconstruction, data postprocessing and statistical analysis. M.S.F. contributed to data collection and experimental design. K.D. contributed to cell culturing and tumor growth as well as animal preparation, and experimental design. T.L. contributed to experimental design and data collection. M.S.A. and E.D. contributed to experimental design. All authors contributed to data analysis, manuscript writing and manuscript editing.

Additional Information

Competing Interests: The authors declare no competing interests.

Chapter 3: Performance improvement of ^{19}F lung MRI using octafluorocyclobutane

This topic has been elaborated in the following publication: **Shepelytskyi Y.**, Li T., Grynko V., Newman C., Hane FT., Albert MS "**Evaluation of fluorine-19 magnetic resonance imaging of the lungs using octafluorocyclobutane in a rat model**" published in *Magnetic Resonance in Medicine*, volume 85, issue 2, pages: 987-994 (2021). The publication text is listed below.

Evaluation of fluorine-19 magnetic resonance imaging of the lungs using octafluorocyclobutane in a rat model

Yurii Shepelytskyi[1,2], Tao Li[3], Vira Grynko[1,2], Camryn Newman[4], Francis T. Hane[2,3], Mitchell S. Albert[2,3,5,*]

1. Chemistry and Materials Science program, Lakehead University, Thunder Bay, ON, Canada.
2. Thunder Bay Regional Health Research Institute, Thunder Bay, ON, Canada.
3. Chemistry Department, Lakehead University, Thunder Bay, ON, Canada.
4. Biology Department, Lakehead University, Thunder Bay, ON, Canada
5. Northern Ontario School of Medicine, Thunder Bay, ON, Canada.

Correspondence: Mitchell S. Albert, Lakehead University, 955 Oliver Road, Thunder Bay, Ontario P7B 5E1, Canada. Email: malbert1@lakeheadu.ca.

Funding information: Northern Ontario Academic Medicine Association (A-16-01).

Abstract

Purpose: To test octafluorocyclobutane (OFCB) as an inhalation contrast agent for fluorine-19 MRI of the lung, and to compare the image quality of OFCB scans with perfluoropropane (PFP) scans

Theory and Methods: After normalizing for the number of signal averages, a theoretical comparison between the OFCB signal-to-noise ratio (SNR) and PFP SNR predicted the average SNR advantage of 90% using OFCB during gradient echo imaging. The OFCB relaxometry was conducted using single-voxel spectroscopy and spin-echo imaging. A comparison of OFCB and PFP SNRs was performed in vitro and in vivo. Five healthy Sprague-Dawley rats were imaged during single breath-hold and continuous breathing using a Philips Achieva 3.0T MRI scanner (Philips, Andover, MA). The scan time was constant for both gases. Statistical comparison between PFP and OFCB scans was conducted using a paired t test and by calculating the Bayes factor.

Results: Spin-lattice (T_1) and effective spin-spin (T_2^*) relaxation time constants of the pure OFCB gas were determined as 28.5 ± 1.2 ms and 10.5 ± 1.8 ms, respectively. Mixing with 21% of oxygen decreased T_1 by 30% and T_2^* by 20%. The OFCB *in vivo* images showed 73% higher normalized SNR on average compared with images acquired using PFP. The statistical significance was shown by both paired t test and calculated Bayes factors. The experimental results agree with theoretical calculations within the error of the relaxation parameter measurements.

Conclusion: The quality of the lung images acquired using OFCB was significantly better compared with PFP scans. The OFCB images had higher a SNR and were artifact-free.

Keywords:

fluorine-19, lung magnetic resonance imaging, octafluorocyclobutane, perfluoropropane

1. Introduction

MRI of inhaled inert fluorinated gases demonstrated promising results as a novel lung imaging modality.[1-3] A variety of studies using sulfur hexafluoride (SF6),[4-6] perfluoroethane (C_2F_6),[7-9] and perfluoropropane (PFP-C_3F_8)[2,5,10-12] demonstrated the feasibility of fluorine-19 (^{19}F) MRI of the lung for diagnostics and the study of many lung disorders. Fluorinated gases can be mixed with oxygen (O_2) and used for continuous-breathing imaging, which allows for dynamic scanning and the study of dynamic lung physiology, including the fractional ventilation measurement study.[4,13] The short T_1 relaxation times of fluorinated gases allows a high number of signal averages, resulting in a sufficient image signal-to-noise ratio (SNR). Other advantages of ^{19}F lung MRI are that it has a high natural abundance (~100%) and a large gyromagnetic ratio, which maximizes the ^{19}F MRI signal.[9]

Despite the advantages associated with ^{19}F MRI, the SNR of acquired images is lower compared with another lung imaging modality: hyperpolarized noble gas MRI.[1,3] This attribute results from the natural Boltzmann distribution of the spins in the Zeeman energy states for fluorinated gases, as opposed to hyperpolarized gases. Multiple studies have researched ways of improving the quality of ventilation images acquired with fluorinated gases.[2,12,14-16] The main factors that affect SNR are the number of equivalent ^{19}F atoms and the relaxation time of the fluorinated gas. Therefore, it is feasible to explore other fluorinated gases that can enhance the SNR associated with ^{19}F MRI. Octafluorocyclobutane (C_4F_8 [OFCB]) belongs to the family of inert fluorinated gases, contains eight chemically equivalent fluorine atoms per molecule (which is a greater number of equivalent ^{19}F atoms compared to other fluorinated gases), and has a longer spin-spin relaxation time. OFCB is a commercially available gas, with a similar cost as PFP (13.8$ per liter). All these factors make OFCB a promising candidate for ^{19}F lung MRI. Although OFCB has not been clinically approved for human inhalation, it has no adverse effects based on inhalation.[17]

Previous reports by Wolf et al.18 and Friedrich et al.[19] used OFCB for the visualization of inert gas washout during high-frequency oscillatory ventilation. Recently, the first spin-echo images of human lungs using OFCB were acquired at 0.5T.[20]

The goal of this work was to compare OFCB with PFP and to determine the feasibility of using OFCB as a fluorinated gas for ^{19}F lung MRI by comparing its SNR to the SNR of PFP scans. In this work, we demonstrate that OFCB has a higher SNR than PFP for both MR spectroscopy and imaging. In addition, we measured all relaxation parameters of the pure gas and the gas premixed with 20% O_2 and studied the influence of the unequal number of averages on the SNR comparison.

2. Theory

To calculate the theoretical signal for the steady-state condition, the following equation can be used[2]:

$$S = S_0 \frac{\left(1-e^{-TR/T_1}\right)e^{-TE/T_2^*}}{\left(1-\cos(\alpha)e^{-TR/T1}\right)}\sin(\alpha), \qquad [3\text{-}1]$$

where α is the flip angle (FA). Because the T_1 time of the OFCB–O_2 mixture is approximately 70% longer compared with PFP–O_2 (Table 3-1), to make a proper estimation of their SNR performance, the number of signal averages (NSA) of OFCB–O_2 scans should be 70% less compared with PFP–O_2 NSA (to keep scan time the same for both measurements). Using the measured relaxation parameters in vivo (Table 3-1) and NSA for a single breath-hold protocol, the ratio of OFCB SNR normalized on NSA to PFP normalized SNR was plotted as a function of pulse repetition time (TR) and echo time (TE) for a 70°

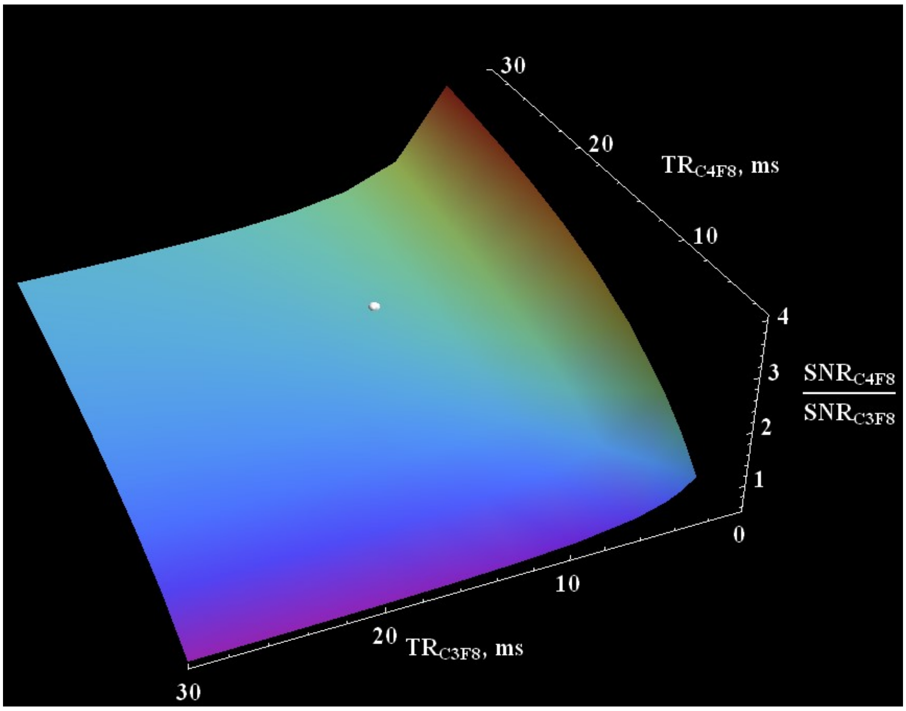

Figure 3-1. Theoretical dependence of in vivo octafluorocyclobutane–oxygen (OFCB-O_2) to perfluoropropane–oxygen (PFP–O_2) signal-to-noise ratio (SNR) as a function of pulse repetition times (TRs). The SNR values were normalized on the number of signal averages (NSA) used for the animal scans (NSA_{OFCB} = 16, NSA_{PFP} = 24). The normalized SNR of PFP gas can excite the normalized SNR of OFCB only if TR_{OFCB} <7 ms. However, this value is impractical for a 70°-Ernst angle; therefore, it will never be used for the real scans. The white dot represents the experimental results. It can be seen that the experimental result nicely agrees with theoretical calculations.

FA (Figure 3-1). Using Equation [3-1], the theoretical SNR advantage of using OFCB was calculated for three types of scan parameters. For a single breath-hold experiment, OFCB normalized SNR should be 86% higher compared with PFP. For continuous breathing using a 70° FA, the normalized SNR advantage of OFCB should be equal to 98%, whereas for a full-recovery regime, the SNR advantage becomes 86%.

3. Methods

3.1. General Information

This study was divided into two parts: (1) A phantom study to measure the relaxation parameters of pure gases and O_2 mixtures. A SNR comparison of OFCB and PFP gradient echo (GRE) images was also conducted. (2) A SNR comparison *in vivo* by acquiring ventilation images of healthy rat lungs. For this study, a clinical Philips Achieva 3T MRI scanner (Philips, Andover, MA) was equipped with a custom-built quadrature birdcage coil tuned to the Larmor frequency of fluorine (120.15 MHz). Four phantoms, consisting of a syringe containing 8 mL of one of the gases, OFCB (99.9999%; Advanced Specialty Gases, Reno, NV), pure PFP (>99.99%; Air Liquide, Paris, France), OFCB breathing mixture (79% OFCB mixed with 21% O_2), and the medical-grade PFP (79% PFP mixed with 21% O_2) were used.

3.2. Phantom Study

MR spectra of the gas phantoms were acquired using the following parameters: TR/TE = 750 ms/0.14 ms, bandwidth (BW) = 32 kHz, sampling number = 2048, and FA = 90°. The spectral peaks were fitted to the Lorentzian peak shape and T_2^* was extracted from full-width half-maximum (FWHM) of the fitted peak using equation $T_2^* = 1/\pi FWHM$. To measure the spin-lattice (T_1) relaxation time constant, a series of inversion recovery (IR) spectra was acquired. Pure gases were studied using the following inversion times (TIs): $TI_{min} = 4$ ms, $TI_{max} = 91$ ms, and $\Delta TI = 3$ ms. The O_2 mixtures were studied using $TI_{min} = 4$ ms, $TI_{max} = 28$ ms, and $\Delta TI = 1$ ms. Other spectroscopy parameters were the same as outlined above. Following the spectroscopy study, the direct comparison of the two axial ^{19}F GRE images of OFCB phantoms and PFP phantoms were acquired. The following GRE imaging parameters were used for the imaging of pure gases: field of view (FOV) = 100 × 100 mm^2, 64 × 64 matrix, TR/TE = 200 ms/1 ms, and Cartesian sampling. To image the breathing mixture phantoms, the following repetition times were used: TR_{PFP}-O_2 = 63 ms, TR_{OFCB}-O_2 = 100 ms, and FA = 90°. All other parameters were kept the same for imaging the pure gases. The SNR was calculated as the peak intensity to the standard deviation (SD) of the noise region ratio.

Table 3-1. Measured T_1 and T_2^* relaxation times and gradient echo image SNR of the studied gases

	T_1(ms)	**T_2^*(ms)**	**GRE SNR (experimental values)**	**GRE SNR (normalized for NSA)**
OFCB	28.5 ± 1.2	10.5±1.8	45.52	45.52
PFP	18.6 ± 0.4	6.26±0.27	30.26	30.26
OFCB-O_2	20.4 ± 0.21	8.6 ± 0.5	14.52	14.52
PFP-O_2	14.98±0.61	5.4 ± 0.3	9.42	9.42
OFCB-O_2 (in vivo)	17.77 ± 1.5	3.4 ± 0.4	9.72 ± 2.1 (breath-hold) 14.48 ± 4.51 (continuous breathing, 70°) 10.23 ± 0.70 (continuous breathing, 90°)	0.61 ± 0.13 (breath hold) 0.1 ± 0.03 (continuous breathing, 70°) 0.39 ± 0.03 (continuous breathing, 90°)
PFP-O_2 (in vivo)	12.8 ± 1.1	2.2 ± 0.3	7.66 ± 2.0 (breath-hold) 12.68 ± 4.09 (continuous breathing, 70°) 8.81 ± 0.46 (continuous breathing, 90°)	0.32 ± 0.08 (breath hold) 0.06 ± 0.02 (continuous breathing, 70°) 0.21 ± 0.01 (continuous breathing, 90°)

3.3 Animal study

3.3.1. Animal preparation

All animal studies were conducted in accordance with the guidelines of the Canadian Council on Animal Care and approved by the Lakehead University Animal Care Committee (AUP 1463772). Five healthy Sprague-Dawley rats weighing between 300 and 400 g were imaged in this study. The animals were prepared for surgery as described in Chahal et al.[21] Briefly, rats were anesthetized with isoflurane and propofol. A midline incision allowed an endotracheal catheter to be placed. The catheter was connected to a custom-built rodent ventilator.

The rat was given a OFCB–O_2 breathing mixture (79% of OFCB mixed with 21% O_2) at 60 breaths per minute with a 4-mL tidal volume. The rat was placed inside the custom-built quadrature ^{19}F coil. After the OFCB data acquisition, the ventilator was switched to pure O_2 to remove any OFCB left inside the lungs. Following 5 minutes of O_2 ventilation, the ventilator was switched to a PFP–O_2 breathing mixture. Following the PFP data acquisition, the animals were euthanized by barbiturate overdose.

3.3.2. *In vivo* imaging

Two different breathing protocols were performed in this study: a single breath-hold for 11 seconds, and continuous breathing for 3 minutes and 5 seconds. All lung images were acquired using a GRE pulse sequence with a Cartesian readout. All animals were scanned during a single breath-hold; however, only three rats were scanned using the continuous breathing protocol. During continuous breathing, the two sets of scans were conducted: (1) using the Ernst angle condition that is most commonly used in preclinical studies, and (2) using the condition of full recovery of longitudinal magnetization for a more accurate comparison between two gases at laboratory conditions because this regime is almost insensitive to T_1 variation of the inhaled gas mixture.

T_1 and T_2^* relaxation times have been measured *in vivo* using the same approach from the phantom study.

The ^{19}F lung projection images during single breath-hold were acquired using the following parameters: FOV = 100×100 mm^2, 32×32 acquisition matrix, TE = 0.63 ms, FA

= 70°, and BW = 436 Hz/pixel. To keep the scan time equal to the breath-hold duration, the NSAs were equal to 16 and 24 for OFCB and PFP breathing mixtures, respectively.

The ^{19}F lung projections for the continuous breathing protocol were acquired either using full recovery (FA = 90°) or using the 70° Ernst FA. The following GRE pulse sequence parameters were used: FOV = 100×100 mm^2, 64×64 acquisition matrix, TE = 0.95 ms, BW = 246 Hz/pixel, and scan time = 185 seconds. The NSAs of 144 and 221 were used for OFCB and PFP, respectively, when the 70° FA was used. During the full-recovery scans, the NSA for the OFCB scan was equal to 29, whereas the PFP NSA was equal to 41. The following TR values were used in this study: TR_{PFP}-O_2/ TR_{OFCB}-O_2 = 12.5 ms/20 ms (FA = 70°) and TR_{PFP}-O_2/ TR_{OFCB}-O_2 = 63 ms/100 ms (FA = 90°). No respiratory gating was used.

3.3.3 Data processing

The spectroscopy data processing, paired t test, and all fitting were calculated using OriginPro 2016 software (OriginLab Corp, Northampton, MA). The ^{19}F MR images were reconstructed and analyzed using custom MATLAB scripts in MATLAB R2016b (MathWorks, Inc, Natick, MA). The image SNR was calculated as the mean signal value in a rectangular region of interest in the right lung divided by the SD of noise in a similar region of interest in the background. The calculation of the Bayes factor for the statistical analysis was conducted using the MATLAB Bayes factor package (v.1.0.0 by Bart Krekelberg). The criterion of significance of the results, based on the value of Bayes factor, was used as published by Kass and Raftery.[22] The theoretical TR versus TE plot was created using Wolfram Mathematica 9.0.1.0 software (Wolfram Research, Inc, Champaign, IL).

4. Results

4.1 The phantom study

The spin-lattice relaxation time constant (T_1) of pure OFCB was measured to be 28.5 ± 1.2 ms (Figure 3-2A). The T_1 relaxation time of pure PFP was measured and was equal to 18.6 ± 0.4 ms, which is similar to values reported in Chang and Conradi.[23] The measured T_2^* relaxation times were equal to 10.5 ± 1.8 ms and 6.26 ± 0.3 ms for OFCB and PFP, respectively.

Following relaxometry of the pure gases, the relaxation properties of the 20% O_2 mixtures were measured. The T_1 relaxation time of the OFCB–O_2 mixture was shortened to 20.4 ± 0.21 ms, and the T_1 time of the PFP–O2 mixture was equal to 14.98 ± 0.61 ms. The T_2^* relaxation times were equal to 8.6 ± 0.5 ms and 5.4 ± 0.3 ms for OFCB–O_2 and PFP–O_2 mixtures, respectively.

Single-voxel (SV) spectroscopy of OFCB, PFP, and their respective O_2 mixtures was conducted to see the signal difference on the MR spectra. The acquired spectra of the pure gases are shown in Figure 3-2A. The single-voxel spectra of the 20% O_2 mixtures are presented in Figure 3-2C. The SNR values were equal to 628.44, 499.91, 400.44, and 362.10 for the OFCB, OFCB–O_2, PFP, and PFP–O_2 phantoms, respectively. The SNR value obtained

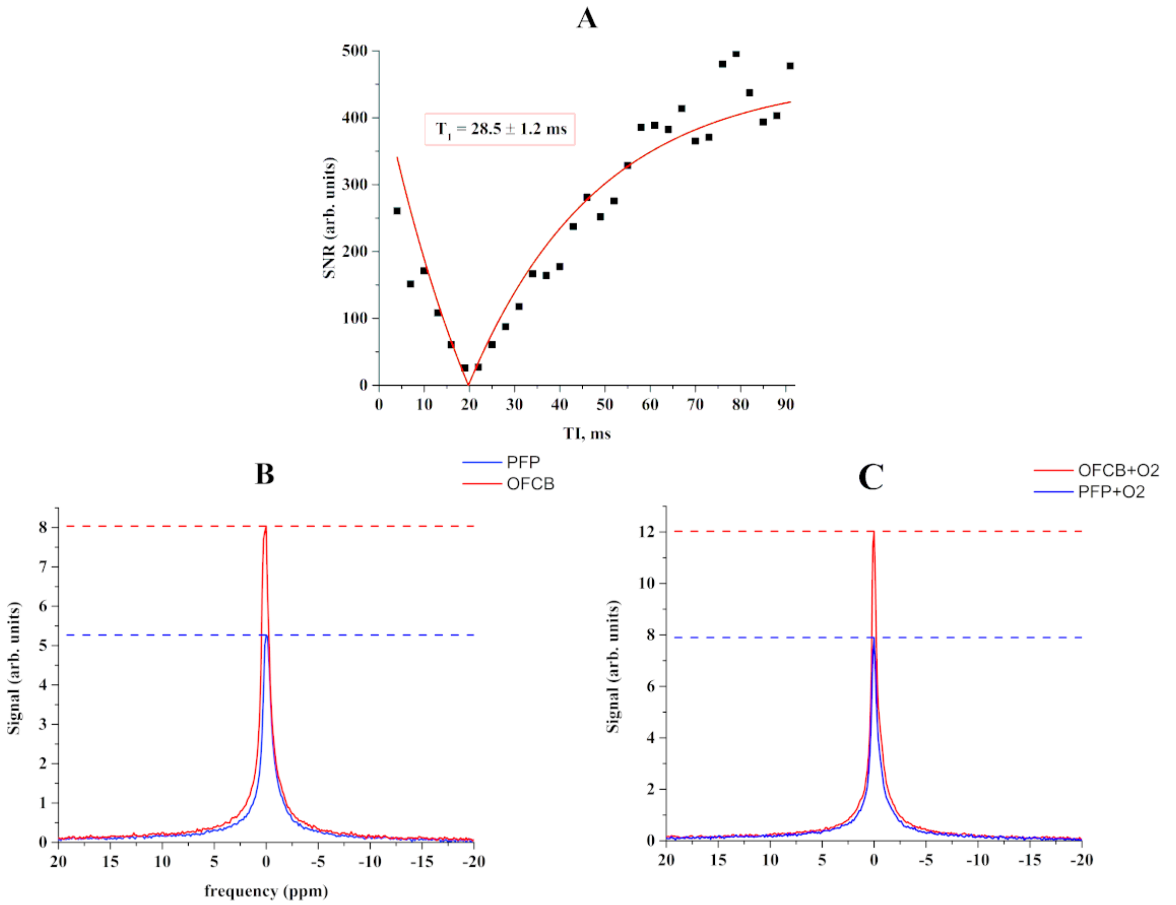

Figure 3-2. A representative inversion recovery curve measured for pure OFCB (A). The measured spectra of 8 ml of pure PFP (blue) and OFCB (red) (B). Spectra (C) were obtained from 8ml of PFP and OFCB breathing mixtures. The horizontal lines represent the maximum value of the corresponding MRS peak.

from pure OFCB gas was approximately 1.57 times higher than pure PFP SNR. However, the SNR value of the OFCB–O_2 spectrum was approximately 38% higher than the PFP–O_2 SNR.

Because the PFP gas has a shorter T_2^* relaxation time, the peak appeared broader and shorter. The ratio of PFP integral values to the OFCB integral was equal to 0.74 and 0.75 for pure gases and O_2 mixtures. This result agrees with the theoretical 6:8 ratio predicted from a molecular structure of the studied gases.

GRE imaging was conducted on phantoms to evaluate the SNR performance of OFCB. The OFCB images were compared with the image of the main peak of PFP. The SNR of the pure PFP phantom image was equal to 30.26, whereas the SNR of the pure OFCB was approximately 50% higher and equal to 45.52. The presence of O_2 did not cause any decrease for the SNR difference. The SNR of the OFCB–O_2 mixture (SNR = 14.22) was 51% higher than the SNR of the medical-grade PFP (SNR = 9.42). The measured relaxation times and SNR values are summarized in Table 3-1.

4.2. The animal study

Figure 3-3 shows whole-lung projections in the axial plane acquired during a single breath-hold (Figure 3-3A,D) and continuous breathing (Figure 3-3B,C,E,F) from the same animal. The first row of images shows the OFCB scans, and the second row shows the PFP scans. Figure 3-3B and E were ac- quired using FA = 70°, TR_{PFP} = 13 ms, and TR_{OFCB} = 20 ms. Figure 3-3C and F were acquired using a full recovery of longitudinal magnetization condition.

The normalized SNR value for the NSA of the OFCB single breath-hold image was equal to 0.61, which was ap- proximately 85% larger than the normalized SNR image from the PFP breathing mixture (SNR = 0.33). The normalized SNR values of images acquired using a FA = 70° during 185 seconds of continuous breathing were equal to 0.11 and 0.06 for OFCB–O_2 and PFP–O_2 mixtures, respectively. The SNR advantage of using OFCB was calculated to be 83%. Finally, the images acquired using a full-recovery condition during continuous breathing had a normalized SNR of 0.37 and 0.22 for OFCB and PFP, respectively.

The T_1 values of OFCB–O2 and PFP–O2 mixtures in the animal lungs were equal to 17.77 ± 1.5 ms and 12.8 ± 1.1 ms. T_2^* values were equal to 3.4 ms and 2.2 ms for OFCB–O_2 and PFP–O_2 breathing mixtures, respectively.

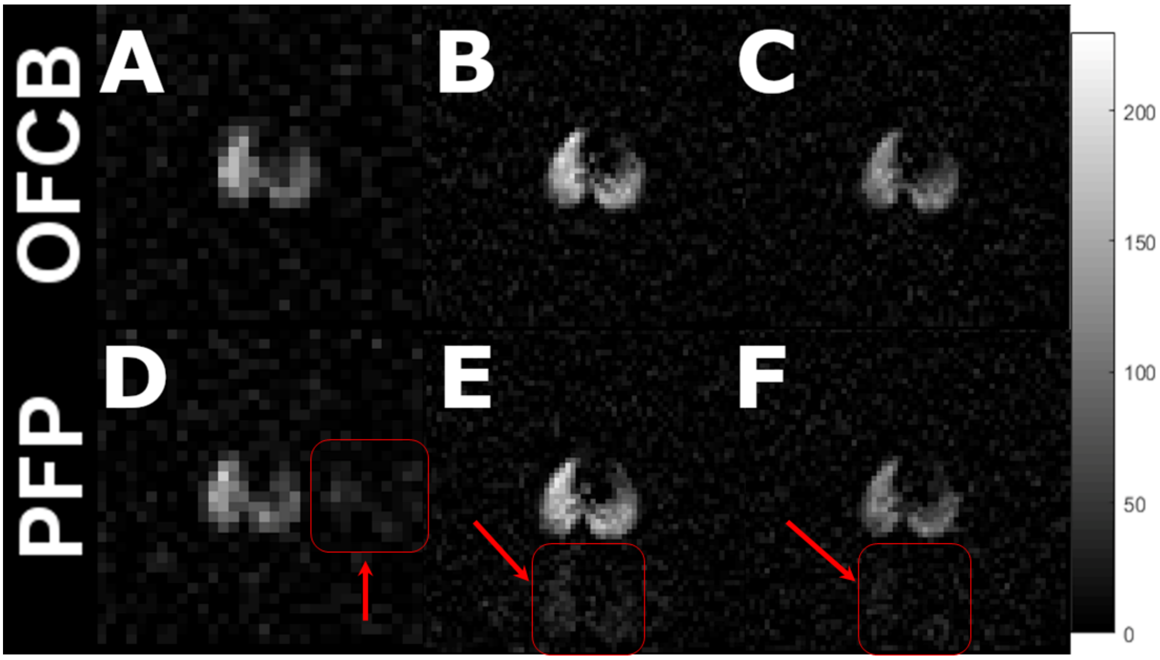

Figure 3-3. In vivo lung ventilation images of a healthy rat acquired in axial projections. The first column shows scans acquired during a single breath-hold; the second column corresponds to the scans acquired during continuous breathing and using a 70° Ernst angle; the third column contains scans obtained during continuous breathing using a 90° flip angle (FA). The signal-to-noise ratio (SNR) of the single breath-hold octafluorocyclobutane (OFCB) scan was 21% higher compared with the corresponding perfluoropropane (PFP) scan. For continuous breathing, the SNR of the OFCB image acquired using the Ernst angle of 70° was 15% stronger. Finally, during continuous breathing scans in the full recovery regime, the OFCB SNR exceeded PFP SNR by 17%. The red arrows indicate the chemical shift artifact associated with second spectral peak of PFP.

The nonnormalized SNR values of images acquired using a single breath-hold protocol and the SNR values of the scans acquired during the continuous-breathing protocol using a FA = 70° and a FA = 90° are shown in Figure 3-4. The SNR of the one axial ventilation image acquired during continuous breathing using a 90° FA was not calculated because a ghosting artifact was observed on the image. Therefore, this scan was excluded from further statistical analysis. The mean normalized and non-normalized SNR values are provided in Table 3-1.

4.3 Statistical analysis

A paired t test was used to evaluate the SNR difference between the OFCB and PFP scans for each image acquisition protocol. The mean values of the nonnormalized SNR values for single breath-hold images were equal to 9.12 ± 2.10 and 7.66 ± 2.00 for OFCB and PFP breathing mixtures, respectively. The OFCB produced significantly a higher SNR (P = .0017), which was supported by a Bayes coefficient of 1.4 × 10^3.

The mean noncorrected SNR of OFCB images obtained during continuous breathing were equal to 14.48 ± 4.51 and 10.23 ± 0.7 using a FA = 70° and a FA = 90°, respectively. The average SNR values of PFP images were equal to 12.68 ± 4.09 (FA = 70°) and 8.81 ± 0.46 (FA = 90°). OFCB SNR values were significantly higher compared with PFP values (P = .0196 [FA = 70°]; P = .038 [FA = 90°]). This significance was supported by values of the Bayes coefficient: 331.73 (FA = 70°) and 343.74 (FA = 90°). Both normalized and non-normalized SNR values are provided in Table 3-1.

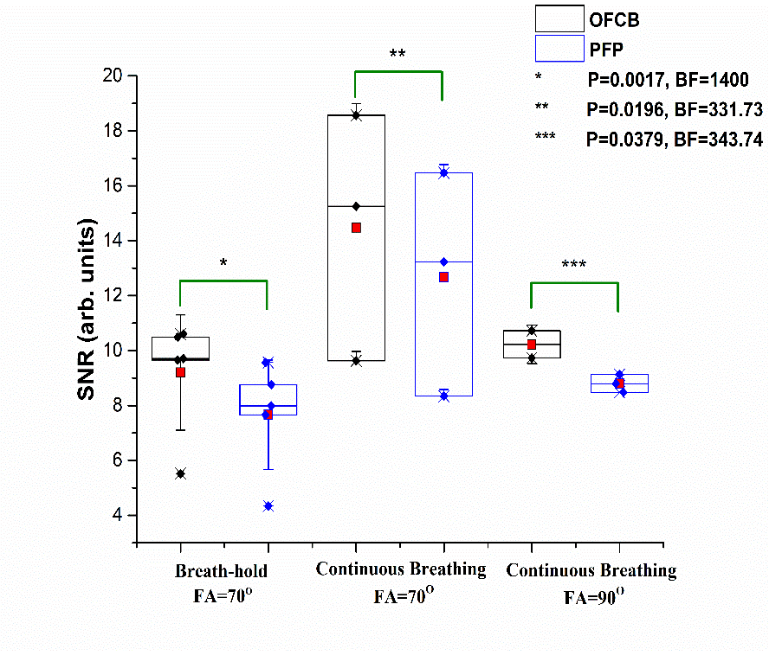

Figure 3-4. Non-normalized signal-to-noise ratio (SNR) box charts of scans conducted using the single breath-hold protocol, and continuous breathing protocol. The black boxes correspond to octafluorocyclobutane (OFCB) scans, and the blue boxes correspond to perfluoropropane (PFP) scans. The red squares illustrate the mean SNR of the group. Whiskers illustrate the standard deviation from the mean SNR. The SNR values of the OFCB scans were statistically significantly higher compared with the PFP scans. The corresponding P values and Bayes factors are shown in the figure legend. The wider scatter of SNR values obtained using the Ernst angle condition during continuous breathing can be explained by the absence of respiratory gating. The Ernst angle condition strongly depends on the T_1 relaxation time of the gas in the lungs, and the absence of gating caused a T_1 variation because of the fluorinated gas-concentration differences during imaging.

5. Discussion

Inert fluorinated gases can be used as gas contrast agents for MRI of the lungs. Currently, PFP is the most common gas agent used in preclinical studies.[1,3] The results presented above demonstrate the benefits of using OFCB gas as an MRI contrast agent. OFCB is inert, which makes it safe for inhalation. The main advantage of OFCB over PFP is the presence of eight chemically equivalent nuclei in the molecule. Furthermore, it has a longer effective transverse relaxation time constant than the PFP T_2^* value. These two properties cause OFCB SNR to be 1.57 times higher than the PFP SNR. The results comparing GRE SNR of PFP and OFCB phantoms showed slightly less SNR differences than spectroscopy. However, the SNR of OFCB images was significantly higher than images of PFP phantoms.

The measured spin-lattice relaxation parameter of pure OFCB was similar to that reported by Friedirich et al.[19] Interestingly, the effective spin-spin relaxation time constant was approximately half of what was previously published. This shortening of T_2^* could be explained by the effect of a two times stronger external magnetic field compared to what was previously used in the literature.[19] The obtained PFPs relaxation parameters values were close to those published by Chang and Couch.[23,24]

The short T_1 relaxation time is an advantage of fluorinated gases, which allows high NSA acquisition during a single breath-hold. OFCB has the longer T_1 relaxation time compared with other widely used fluorinated gases. Theoretical calculations of SNR showed that OFCB still produces higher SNR even with a smaller amount of averages. Because OFCB allows the acquisition of higher SNRs using lower NSA, the specific absorption rate of the imaging sequence with OFCB will be lower than for imaging with any other inert fluorinated gas.

OFCB has another practical advantage compared with PFP: The ^{19}F spectrum of OFCB contains only one single peak, whereas the PFP spectrum has two peaks. As a result, the signal of the second PFP peak should be suppressed to avoid creation of a second lung image, which could over- lap with the image of the main peak. OFCB does not have this drawback, which makes it more convenient for practical applications.

The results of the animal experiments agree with the theoretical calculations (Figure 3-1). The normalized for NSA OFCB SNR advantage was equal to 90% for a single breath- hold (white point on Figure 3-1). The theoretically predicted value of the normalized SNR advantage was 86%. There is a slight deviation from the theory for a continuous breathing protocol. The normalized SNR advantage of OFCB was calculated to be equal to 98% and 86% for the 70° Ernst angle and full longitudinal magnetization conditions, respectively. The observed normalized OFCB SNR boosts were equal to 76% for the Ernst-angle condition and to 86% for the full longitudinal magnetization recovery condition, which is lower than the theoretically predicted value. This can be explained by a slight mismatch between the OFCB T_1 *in vivo* and the TR used during the scans and the absence of respiratory gating. The larger scatter of SNR values for the Ernst-angle condition (Figure 3-4) is caused by the absence of respiratory gating during the scan. Because the 70° Ernst-angle condition depends strongly on the T_1 of the gas in the lungs, the absence of respiratory gating can potentially cause a variation of T_1 based on the different concentrations of the fluorinated gases in the lungs. All of the three predicted advantages of OFCB (higher SNR, absence of chemical shift artifacts, low specific absorption rate) were observed. The SNR of OFCB images was significantly higher even with an approximately 65% smaller number of signal averages.

In this study, we showed that OFCB is a suitable candidate for ^{19}F MRI of the lungs. The image quality of OFCB scans was significantly higher compared with commonly used PFP. In addition, OFCB scans are safer in terms of tissue-heating because of a lower specific absorption-rate value compared with PFP. The roughly estimated OFCB-scan specific absorption rate is approximately 60% lower compared with PFP scans because of the smaller number of signal averages.

Acknowledgments

The authors would like to thank Lakehead University and the Thunder Bay Regional Health Research Institute for partial support of this work and access to their facilities. Yurii Shepelytskyi was supported by an Ontario Graduate Scholarship and Mitacs Accelerate Grant. Vira Grynko is supported by an Ontario Trillium Scholarship. The authors acknowledge Alanna Wade for her contribution to the initial phase of this research. Francis Hane is supported by fellow- ships from the BrightFocus Foundation and the Canadian Institutes for Health Research. The authors would like to thank Martina Agostino for contributing to manuscript editing.

References

1. Couch MJ, Ball IK, Li T, Fox MS, Biman B, Albert MS. 19F MRI of the lungs using inert fluorinated gases: Challenges and new developments. *J Magn Reson Imaging*. 2018;49:343-354.

2. Maunder A, Rao M, Robb F, Wild JM. Optimization of steady-state free precession MRI for lung ventilation imaging with 19F C3F8 at 1.5T and 3T. *Magn Reson Med*. 2019;81:1130-1142.

3. Kruger SJ, Nagle SK, Couch MJ, Ohno Y, Albert M, Fain SB. Functional imaging of the lungs with gas agents. *J Magn Reson Imaging*. 2016;43:295-315.

4. Couch MJ, Fox MS, Viel C, et al. Fractional ventilation mapping using inert fluorinated gas MRI in rat models of inflammation and fibrosis. *NMR Biomed.* 2016;29:545-552.

5. Ouriadov AV, Fox MS, Couch MJ, Li T, Ball IK, Albert MS. In vivo regional ventilation mapping using fluorinated gas MRI with an x-centric FGRE method. *Magn Reson Med.* 2015;74:550-557.

6. Adolphi NL, Kuethe DO. Quantitative mapping of ventilation- perfusion ratios in lungs by19F MR imaging of T1 of inert fluori- nated gases. *Magn Reson Med*. 2008;59:739-746.

7. Carrero-González L, Kaulisch T, Stiller D. In vivo diffu- sion-weighted MRI using perfluorinated gases: ADC comparison between healthy and elastase-treated rat lungs. *Magn Reson Med*. 2013;70:1761-1764.

8. Kuethe DO, Caprihan A, Fukushima E, Waggoner RA. Imaging lungs using inert fluorinated gases. *Magn Reson Med.* 1998;39:85-88.

9. Jacob RE, Chang YV, Choong CK, et al. 19F MR imaging of ventilation and diffusion in excised lungs. *Magn Reson Med*. 2005;54:577-585.

10. Halaweish AF, Moon RE, Foster WM, et al. Perfluoropropane gas as a magnetic resonance lung imaging contrast agent in humans. *Chest*. 2013;144:1300-1310.

11. Couch MJ, Ball IK, Li T, et al. Pulmonary ultrashort echo time 19F MR imaging with inhaled fluorinated gas mixtures in healthy volunteers: Feasibility. *Radiology*. 2013;269:903-909.

12. Obert AJ, Gutberlet M, Kern AL, et al. 1H-guided reconstruc- tion of 19F gas MRI in COPD patients. *Magn Reson Med.* 2020;84:1336-1346.

13. Schreiber WG, Eberle B, Laukemper-Ostendorf S, et al. Dynamic 19F-MRI of pulmonary ventilation using sulfur hexafluoride (SF6) gas. *Magn Reson Med*. 2001;45:605-613.

14. Couch MJ, Blasiak B, Tomanek B, et al. Hyperpolarized and inert gas MRI: The future. *Mol Imaging Biol*. 2015;17:149-162.

15. Neal MA, Pippard BJ, Hollingsworth KG, et al. Optimized and ac- celerated 19F-MRI of inhaled perfluoropropane to assess regional pulmonary ventilation. *Magn Reson Med.* 2019;82:1301-1311.

16. Neal MA, Pippard BJ, Simpson AJ, Thelwall PE. Dynamic suscep- tibility contrast 19F-MRI of inhaled perfluoropropane: A novel ap- proach to combined pulmonary ventilation and perfusion imaging. *Magn Reson Med.* 2020;83:452-461.

17. Clayton JW, Delaplane MA, Hood DB. Toxicity studies with octa- fluorocyclobutane. *Am Ind Hyg Assoc J.* 1960;21:382-388.

18. Wolf U, Scholz A, Terekhov M, Koebrich R, David M, Schreiber LM. Visualization of inert gas wash-out during high-frequency oscillatory ventilation using fluorine-19 MRI. *Magn Reson Med.* 2010;64:1479-1483.

19. Friedrich J, Rivoire J, Terekhov M, Schreiber LM. 19F-MRI: Flow measurement of fluorinated gases during high frequency oscilla- tory ventilation. *Proc Intl Soc Mag Reson Med*. 2011;19:3498.

20. Pavlova OS, Anisimov NV, Gervits LL, et al. 19F MRI of human lungs at 0.5 Tesla using octafluorocyclobutane. *Magn Reson Med*. 2020;84:2117-2123. https://doi.org/10.1002/mrm.28270

21. Chahal S, Prete BRJ, Wade A, Hane FT, Albert MS. Brain imag- ing using hyperpolarized 129 Xe magnetic resonance imaging. In: Eckenhoff RG, Dmochowski IJ, eds. *Methods in Enzymology*. Vol 603. Academic Press Inc. 2018:305-320.

22. Kass RE, Raftery AE. Bayes factors. *J Am Stat Assoc*. 1995;90:773-795.

23. Chang YV, Conradi MS. Relaxation and diffusion of perfluoro- carbon gas mixtures with oxygen for lung MRI. *J Magn Reson*. 2006;181:191-198.

24. Couch M, Ball I, Li T, et al. Inert fluorinated gas MRI: A new pulmonary imaging modality. *NMR Biomed*. 2014;27:1525-1534.

Chapter 4: Invention of HP ^{129}Xe Time-of-Flight (TOF) perfusion imaging. HDR detection using HP ^{129}Xe TOF imaging

4.1. HP ^{129}Xe TOF perfusion imaging methodology

This topic has been elaborated in the following publication: **Shepelytskyi Y.**, Hane FT., Grynko V., Li T., Hassan A., and Albert MS. "**Hyperpolarized ^{129}Xe Time-of-Flight MR Imaging of Perfusion and Brain Function**" published in *Diagnostics*, volume 10, issue 9, Article number: 630 (2020). The publication text is listed below.

Hyperpolarized ^{129}Xe Time-of-Flight MR Imaging of Perfusion and Brain Function

Yurii Shepelytskyi[1,2], Francis T. Hane[2,3], Vira Grynko[1,2], Tao Li[3], Ayman Hassan[4,5], and Mitchell S. Albert[2,3,5,*]

[1]Chemistry and Materials Science Program, Lakehead University, 955 Oliver Rd., Thunder Bay, ON P7B 5E1, Canada.

[2]Thunder Bay Regional Health Research Institute, 980 Oliver Rd., Thunder Bay, ON P7B 5E1, Canada.

[3]Chemistry Department, Lakehead University, 955 Oliver Rd., Thunder Bay, ON P7B 5E1, Canada.

[4]Thunder Bay Regional Health Sciences Centre, 980 Oliver Rd., Thunder Bay, ON P7B 6V4, Canada.

[5]Northern Ontario School of Medicine, 955 Oliver Rd., Thunder Bay, ON P7B 5E1, Canada.

[*]Author to whom correspondence should be addressed.

Abstract

Perfusion measurements can provide vital information about the homeostasis of an organ and can therefore be used as biomarkers to diagnose a variety of cardiovascular, renal, and neurological diseases. Currently, the most common techniques to measure perfusion are ^{15}O positron emission tomography (PET), xenon-enhanced computed tomography (CT), single photon emission computed tomography (SPECT), dynamic contrast enhanced (DCE) MRI, and arterial spin labeling (ASL) MRI. Here, we show how regional perfusion can be quantitively measured with magnetic resonance imaging (MRI) using time-resolved depolarization of hyperpolarized (HP) xenon-129 (^{129}Xe), and the application of this approach to detect changes in cerebral blood flow (CBF) due to a hemodynamic response in response to brain stimuli. The investigated HP 129Xe Time-of-Flight (TOF) technique produced perfusion images with an average signal-to-noise ratio (SNR) of 10.35. Furthermore, to our knowledge, the first hemodynamic response (HDR) map was acquired in healthy volunteers using the HP ^{129}Xe TOF imaging. Responses to visual and motor stimuli were observed. The acquired HP TOF HDR maps correlated well with traditional proton blood oxygenation level-dependent functional MRI. Overall, this study expands the field of HP MRI with a novel dynamic imaging technique suitable for rapid and quantitative perfusion imaging.

1. Introduction

Perfusion measurements can provide vital information about the homeostasis of an organ [1] and can therefore be used as biomarkers to diagnose cardiovascular [2,3], renal [4], and neurological [5–7] diseases. Currently, the most commonly used techniques to measure perfusion are ^{15}O positron emission tomography (PET) [8–10], xenon-enhanced computed tomography (CT) [11,12], single photon emission computed tomography (SPECT) [3,8,13], and arterial spin labeling (ASL) magnetic resonance imaging (MRI) [1,14–18]. In addition, dynamic susceptibility contrast (DSC) and dynamic contrast enhanced (DCE) MRI are frequently used for perfusion imaging [19–21]. Although these techniques are well-established, each has some serious drawbacks. CT requires high-dose ionizing radiation, PET and SPECT rely on injection of radioactive contrast agents and the acquired PET images are of low resolution, and the signal-to-noise ratio (SNR) and contrast of ASL images is low. DSC and DCE MRI require injection of contrast agents, most of which contain gadolinium, which was recently associated with a certain amount of toxicity [22,23]. In addition, the most commonly used gadolinium-based contrast agents are uncapable of crossing the blood–brain barrier [24–26], which makes cerebral perfusion imaging with these agents more challenging.

Hyperpolarized (HP) xenon-129 (^{129}Xe) MRI is a powerful MRI approach used mainly for lung imaging and for the study of lung disorders [27,28]. A hyperpolarized (HP) metastable state is produced by spin exchange optical pumping [29–31], and is characterized by up to 10^5 larger longitudinal magnetization compared to thermal polarization [27]. Therefore, the magnetic resonance signal of HP nuclei can be up to 10^5 times stronger than at thermal equilibrium. Due to the ability of HP ^{129}Xe to dissolve in blood and travel to highly perfused organs, HP ^{129}Xe MRI was recently used to study the brain [6,32–34] and kidneys [35]. The last achievements in the field of HP ^{129}Xe MRI allowed the investigation of cerebral perfusion changes associated with Alzheimer's disease [34] and stroke [6].

Since HP ^{129}Xe dissolves in the blood [36] and has extreme sensitivity to chemical environments [27], it can be used as a contrast agent to study blood flow and conduct perfusion measurements in tissues. Since the HP state is a nonequilibrium, metastable state, the longitudinal magnetization is not restored by spin-lattice relaxation once a radiofrequency (RF) pulse irradiates the nuclei. After irradiation of a volume element containing HP ^{129}Xe dissolved in tissue or blood with a 90^O RF pulse, the HP state is completely destroyed and the dissolved HP ^{129}Xe does not produce any significant amount of signal. If there is continuous flow into the volume of dissolved ^{129}Xe, and if the MR measurement is conducted following a prescribed time delay (time-of-flight (TOF) time), the MR signal is determined mainly by the amount of ^{129}Xe washed into the selected volume. We hypothesize that it is possible to measure the blood flow and tissue perfusion quantitatively by creating a dynamic imaging technique which measures the ^{129}Xe signal evolution with change in TOF. The proposed perfusion imaging technique has the potential to open a new pathway for imaging and diagnostics of perfusion-related diseases.

In this proof-of-concept study, we develop a novel HP ^{129}Xe time-of-flight perfusion imaging pulse sequence and evaluate the performance of this technique in vitro and in vivo. The first quantitative HP cerebral perfusion images were acquired using the proposed technique in healthy volunteers. Furthermore, the HP ^{129}Xe TOF technique was used for hemodynamic response detection and was corroborated by conventional proton (^{1}H) blood oxygenation level-dependent (BOLD) fMRI.

2.Materials and Methods

2.1 Pulse Sequence Design

The Chemical Shift Saturation Recovery (CSSR) pulse sequence is typically used to study the time course of hyperpolarized (HP) ^{129}Xe gas exchange in the lungs [37,38]. We modified the CSSR sequence for cerebral perfusion imaging using HP ^{129}Xe to create the ^{129}Xe TOF used in this study (Figure 4-1). The first 90^{O} block pulse has a time duration of 0.5 ms, which yields a bandwidth (BW) of 2 kHz (56.5 ppm). This pulse is broad enough to saturate the HP ^{129}Xe in all brain tissues and the Xe dissolved in blood. After termination of the saturation pulse, the unsaturated ^{129}Xe from the lungs flows into the brain during time τ. The image pulse sequence is then initiated. Here, the broad-band excitation pulse of spredrex shape was used for imaging. The image was acquired using a Gradient Echo (GRE) pulse sequence with a Cartesian read-out. The TOF pulse sequence was repeated three times with different recovery times τ (Figure 4-1). To detect hemodynamic response to a visual stimulus, we used the following delay times: τ_0 = 1 s, τ_1 = 6.5 s, τ_2 = 8 s. To detect hemodynamic response to a motor task, the TOF delays were equal to 2.5 s, 6.8 s, and 7.1 s.

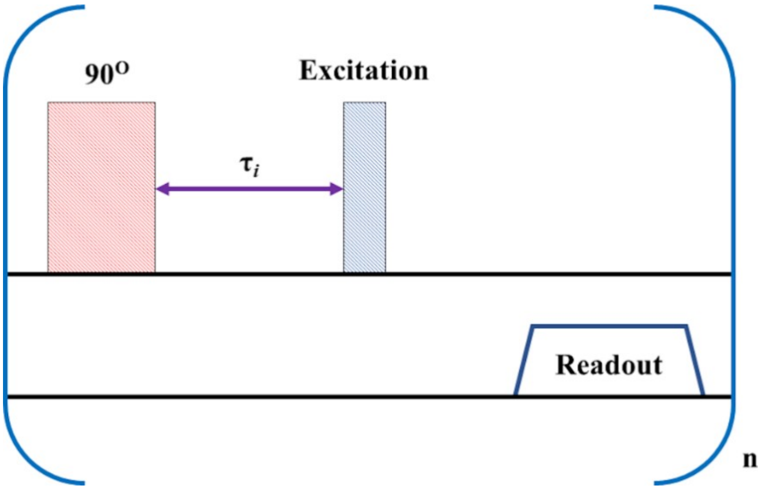

Figure 4-1. ^{129}Xe time-of-flight (TOF) perfusion imaging pulse sequence diagram. The 90° pulse with narrow bandwidth (in pink) is applied first. After the recovery time delay, τ (the purple arrow), the imaging pulse sequence is initiated. The excitation pulse is represented by the blue rectangle. This pulse sequence is repeated n times. Index *i* corresponds to the delay time with an index number *i*.

2.2. In Vitro Flow Measurements

The flow phantom used in this study is shown in Figure 4-2a. The 3.175 mm tube was connected to the syringe pump (Kent Scientific Co, Torrington, CT, USA). A 30 mL syringe was filled with saline and loaded into the pump. One liter of natural abundant ^{129}Xe (~26%) was polarized up to 52% using the Xemed xenon polarizer and dispensed into a TedLar bag. A TedLar bag and a saline tube were connected to the membrane contactor (3M Liqui-Cel MM-0.5 × 1 Series) to mix HP Xe with saline. The outlet of the membrane contactor was connected to the 3.175 mm tube and the end of the tube was placed into the custom-built quadrature coil tuned to the Xe resonance frequency at 3T (35.33 MHz). A saline flow rate was set to 5 mL/min, 6 mL/min, 7 mL/min, and 10 mL/min. The 129Xe TOF GRE imaging was conducted using 20 TOF recovery times that varied from 200 ms to 2000 ms,with a step of 100ms. The following parameters were used for imaging: TR/TE=104.16ms/1.22ms, FA = 12.5^{O}, FOV = 100 × 100 mm^{2}.

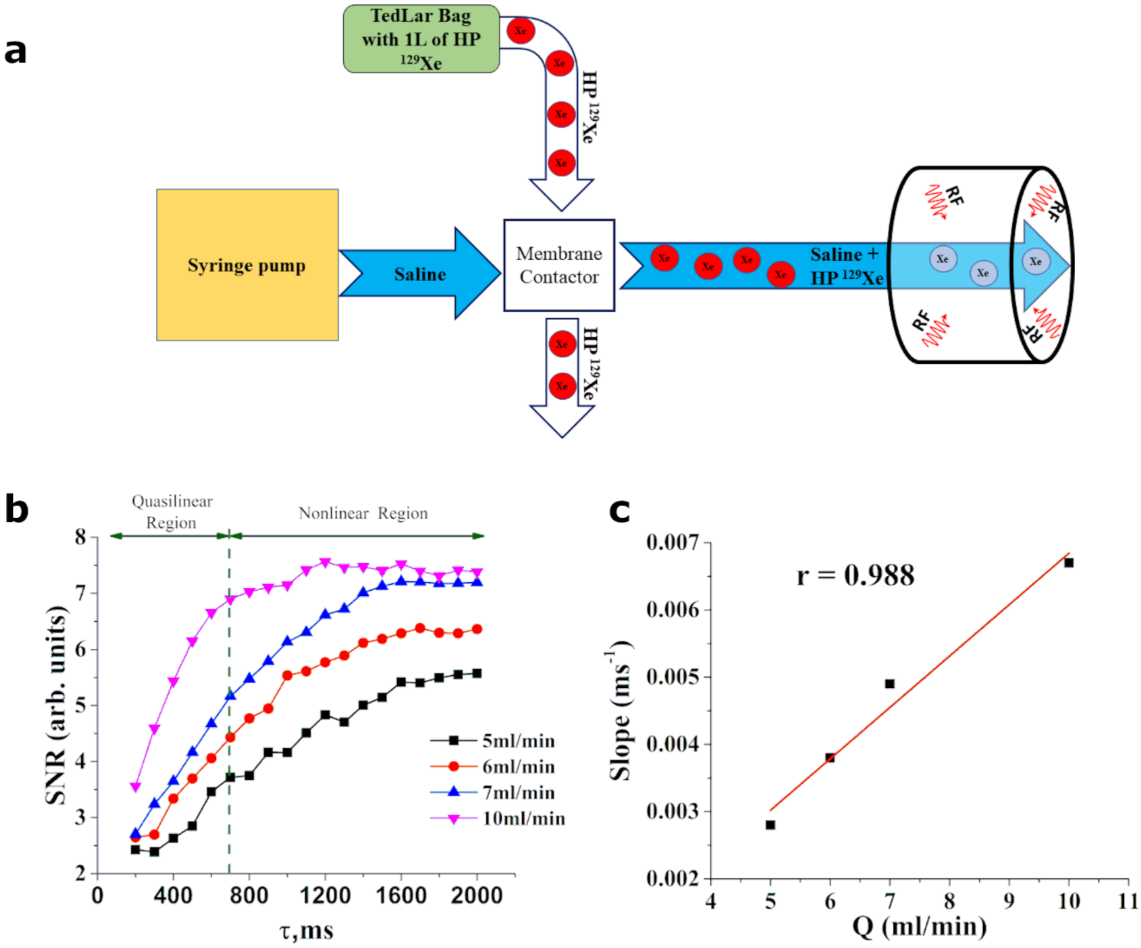

Figure 4-2. *In vitro* phantom design and obtained time-of-flight (TOF) ^{129}Xe curves with Pearson's correlation coefficient. (a) Schematic diagram of the flow phantom used in this study. A syringe pump provided four different flow rates, i.e., 5 mL/min, 6 mL/min, 7 mL/min, and 10 mL/ min. (b) ^{129}Xe TOF recovery curves were measured using the TOF imaging approach. A difference in flow rate of 1 mL/min created well-detected differences in the TOF curves. A quasilinear region was observed between 200 ms and 700 ms. A nonlinear recovery appeared for longer recovery times, followed by a steady state. (c) Pearson's linear correlation between the flow rate and the slopes of the TOF curves was calculated at the quasilinear region. A strong positive correlation (r ≈ 0.988) was observed, indicating the potential to use this slope for flow mapping.

2.3 In Vivo Cerebral Perfusion Measurements in Healthy Volunteers

This research study was approved (Jan. 28, 2019) by the research ethics boards (REB) at Lakehead University (LU) and the Thunder Bay Regional Health Sciences Centre (TBRHSC) (REB file number RP-307) and conducted in accordance with the Tri-Council Policy Statement-2 (TCPS-2). Nine healthy volunteers between the ages of 21 and 77 were recruited from the community for this study. All participants signed an informed consent form. All participants were cognitively normal and consented to the data obtained from them being disseminated in this report.

2.3.1. ^{1}H Magnetic Resonance Imaging

Participants were placed into a dual tuned ^{1}H/^{129}Xe head coil in a Philips Achieva 3T clinical MRI scanner. T_2-weighted ^{1}H MRI were acquired using a turbo-spin echo (TSE) sequence with a Cartesian readout. The high-resolution anatomical proton images were acquired in axial and sagittal views. The sagittal images were acquired using a field-of-view equal to $250 \times 250 \times 46$ mm^3 and a voxel size of $0.98 \times 1.04 \times 6$ mm^3. The repetition time was set to 3 s and the echo time was equal to 80 s. The flip angle of excitation radiofrequency pulse was equal to 90^O. Five slices were acquired, separated by 6 mm gaps. The axial scans were acquired using similar parameters. The only difference was in voxel size, which was equal to $0.98 \times 0.99 \times 6$ mm^3 in the axial scans.

2.3.2 ^{129}Xe Perfusion Mapping Using Time of Flight (TOF)

Enriched ^{129}Xe (83%) was polarized to ~50% using a Xemed xenon polarizer and dispensed into 1 L Tedlar bags. The participant breathed in the gas and held their breath for

20 s. The dynamic ^{129}Xe TOF imaging pulse sequence with a Cartesian gradient echo readout was initiated simultaneously with a breath-hold. Three dynamic projection brain images were acquired during the breath-hold. The TOF recovery delays were equal to 2.5 s, 6.7 s, and 7.1 s. The field of view of gradient echo pulse sequence parameters was equal to 250 × 250 mm^2 and the acquisition matrix was set to 20 × 20. The excitation pulse flip angle was set to 20^{O}. The repetition time was equal to 4 ms, the echo time was equal to 0.71 ms, and the bandwidth per pixel was 382 Hz.

To conduct hemodynamic response mapping, each participant was given two Xe MRI scans, one while staring at a gray screen (baseline) and another while exposed to an external stimulus, such as a flashing visual pattern (the visual stimulus used in this study can be downloaded from the link presented in the Supplementary Material S3) or s rapid left fist squeeze (motor stimulus). Exposure to the visual stimulus started approximately 7 s prior to image acquisition. Immediately prior to image acquisition, the participant inhaled 1 L of the HP ^{129}Xe gas and held their breath for a period of 20 s.

A dynamic ^{129}Xe TOF imaging pulse sequence with a Cartesian gradient echo readout was initiated simultaneously with a breath-hold using the following parameters: FOV = 250 × 250 mm^2, TR/TE = 4 ms/0.71 ms, FA = 20^{O}, BW = 382 Hz, acquisition matrix = 20 × 20. Three dynamic projection brain images were acquired during the breath-hold. The TOF recovery delays were equal to 2.5 s, 6.7 s, and 7.1 s for axial projections and 1 s, 6.5 s, and 7.1 s for the sagittal view. ^{129}Xe TOF perfusion-weighted images were acquired in axial view with a slice thickness of 70 mm and in sagittal view with a slice thickness of 300 mm.

2.3.3. ^{129}Xe Perfusion Mapping Image Processing

Briefly, ^{129}Xe images were zero-padded in k-space to a 32 × 32 matrix and a Fast Fourier transform (FFT) was applied to create MR images. SNR maps were created by dividing each pixel by the standard deviation of the noise region. Based on Killian's model of dissolved Xe [18], the mathematical theory was generalized and applied for HP 129Xe perfusion mapping (for a detailed explanation, see Supplementary Material S1). Three SNR maps created from TOF images and acquired with different recovery times were fitted pixel-by-pixel using the linear equation of the SNR delay time dependence (see Supplementary Material S2), and slope maps were created. The slope maps were further recalculated into perfusion maps using the developed model (see Supplementary Material S1). The SNR of the perfusion images was calculated as the ratio of the mean pixel intensity value from the brain region to the standard deviation of the selected square region from the background. The measured SNR values were compared to the average ASL SNR at 3T published in [39] using one-sample t-test. Xe hemodynamic response maps were created by subtracting the baseline slope map from the task slope map. An Xe functional brain map was overlaid on top of the high-resolution, T_2-weighted proton image. Additional image processing information can be found in the Supplementary Material S4.

2.3.4. BOLD fMRI Image Acquisition

Participants were placed into an eight-channel Philips SENSE coil tuned to the ^1H nucleus. 180 dynamic multi-slice echo-planar imaging (EPI) scans were acquired using the following parameters: FOV = $250 \times 250 \times 119$ mm^3, acquisition matrix = 64×64, voxel size = $3.91 \times 3.91 \times 4$ mm^3, TR/TE = 2 s/30 ms, FA = 90°, 24 slices with a 1 mm slice gap. Participants were subjected to the stimuli described above for the first 20 s and then a rest period for 20 s. Overall, 18 stimulus/rest repetitions were presented during the BOLD fMRI scans. For anatomical localization purposes, high-resolution, T_2-weighted, axial images were acquired using a turbo-spin echo (TSE) pulse sequence using the following parameters: FOV

= 250 × 250 × 119 mm^3, voxel size = 0.98 × 0.99 × 4 mm^3, TR/TE = 3 s/80 ms, FA = 90◦, 24 slices of 4 mm thickness separated by 1 mm gaps.

2.3.5. BOLD fMRI Image Processing

BOLD fMRI and T_2-weighted anatomical images were converted from Philips PAR into Analyze format, and multivolume images were segmented into multiple 3D hdr files using MRIcro 1.40 (by Chris Rorden). The first 20 EPI scans (first complete cycle) were discarded to avoid T_1 effects. fMRI data were processed using SPM12 [40] software using MATLAB R2018b (The Mathworks, Inc, Natick, MA, USA). Following manual alignment of the structural T_2 image to the average canonical T_2 image, the EPI image was manually aligned to the processed structural image. Using the SPM12 software, the obtained aligned EPI images were realigned and only the mean image was resliced. After slice timing and co-registration (an estimate), segmentation of the anatomical T_2 image was performed and the final image was corrected to remove the spatially varying artifact (modulation of the image signal intensity). The functional and anatomical images were normalized using a saved deformation field with specification of the voxel size. Smoothing of the functional images was done with Full Width at Half Maximum (FWHM) set to 6 mm in all directions. The positive t-contrast (stimulus > rest) was calculated for the final functional image. The p-value was adjusted to 0.05 with a Family-Wise Error (FWE) correction. No masking or thresholding were applied during the image processing. Statistical maps were overlaid on volume-rendered brain images provided by SPM12.

Signal enhancement was estimated using the MarsBar extension for SPM12 (by Matthew Brett, available at http://marsbar.sourceforge.net/). The region of interest (ROI) was specified for the cluster with the highest intensity from SPM results file. This was viewed and exported as an image with the base space.

3. Result

3.1. In Vitro Evaluation of HP ^{129}Xe TOF Pulse Sequence

The ^{129}Xe TOF pulse sequence (Figure 4-1) was programmed on a Philips 3.0T Achieva MRI scanner and tested using a flow phantom (Figure 4-2a). A previously developed model of Xe uptake in the brain [41] was modified to facilitate quantitative perfusion measurements using ^{129}Xe TOF imaging. The complete analytical function, which describes the signal evolution in a brain voxel (see Supplementary Material S1), is difficult to implement practically and, therefore, a simplified model for the ^{129}Xe wash-in phase was developed by employing several assumptions. First, ^{129}Xe relaxation in blood [32,41–45] is the predominant factor of polarization decay during the wash-in phase. Second, the value of the sum of the tissue perfusion-to-partition coefficient ratio plus the relaxivity of HP ^{129}Xe in the tissue is small. With these two assumptions, the SNR evolution during the TOF imaging sequence can be expressed as a linear function (for the detailed mathematical derivation please see Supplementary Information), where the slope of the line is directly proportional to the sum of perfusion of all tissues in the voxel. This approach is valid only for short recovery times and can be easily used in practice, albeit yielding an underestimation of the slope of the TOF recovery curves for longer TOF delay times.

The flow rates were set to 5 mL/min, 6 mL/min, 7 mL/min, and 10 mL/min. The signal-to-noise ratio (SNR) increased linearly at small recovery times, followed by a nonlinear transition (intermediate recovery times) up until saturation (long recovery times) (Figure 4-2b). The nonlinear dynamic at intermediate recovery times can be explained by a nonlinear ^{129}Xe velocity distribution in saline flow cross-sections. The signal became saturated earlier for the fastest flow rate, whereas a slight signal saturation was observed for the slowest flow rate. The slopes of the TOF recovery curves were calculated, and a strong

Pearson’s correlation ($r = 0.988$, $p < 0.05$) between the flow rate and the signal recovery rate was observed (Figure 4-2c). A difference of 1 mL/min in flow caused the observed change in the recovery rate.

3.2. HP ^{129}Xe TOF Cerebral Perfusion Imaging

Human imaging experiments were approved by the research ethics boards at Lakehead University and the Thunder Bay Regional Health Science Centre and conducted in accordance with the Tri-Council Policy Statement 2. All participants signed an informed consent form. During human imaging, the changes in the volunteers’ blood oxygen saturation levels were within the normal range. All images were acquired during a single breath-hold after inhalation of 1 L of HP ^{129}Xe. The obtained images were converted from radiological to anatomical views.

Figure 4-3a,f demonstrate the high-resolution, T_2-weighted proton images which were used for brain localization. Figure 4-3b–d show 129Xe TOF images acquired in the axial view after TOF of 2.5, 6.5, and 7.1 s. HP ^{129}Xe TOF sagittal images (Figure 4-3g–i) were acquired following 1 s, 6.5 s, and 8 s TOF delays. Following pixel-by-pixel calculations of the TOF slope, the corresponding ^{129}Xe TOF perfusion-weighted images were reconstructed in both the axial and sagittal projections. The average SNR of the reconstructed, perfusion-weighted images was equal to 11.2 ± 2.9 (in the sagittal projection) and 9.5 ± 2.9 (in the axial projection). Using the theoretical calculations shown in the Supplementary Information, the slope maps were transformed into net perfusion maps (Figure 4-3e,j). Although the ^{129}Xe TOF pulse sequence is similar to the ASL pulse sequence, the manipulation of the magnetization is fundamentally different. The contrast of perfusion-weighted ASL images comes from the difference between control and spin-tagged images, whereas the contrast of TOF perfusion maps comes directly from the velocity of incoming blood flow.

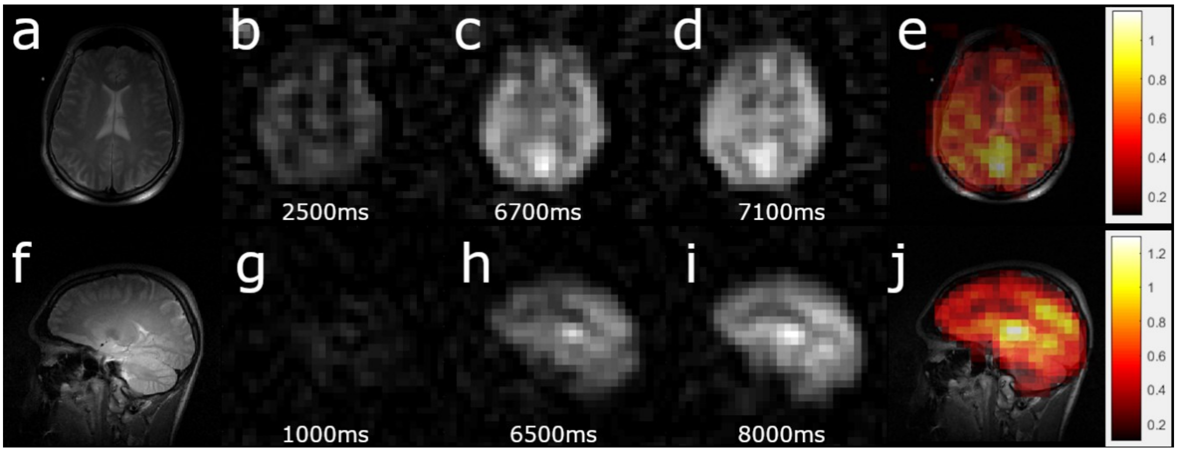

Figure 4-3. Example of perfusion map acquisition. (a,f) High-resolution, T_2-weighted 1H scans for brain localization. (b–d) Three dynamic HP ^{129}Xe TOF images acquired 2.5 s, 6.8 s, and 7.1 s after the application of a depolarization radiofrequency pulse in the axial projection. The image artifact in the top left corner in b is from excess gaseous ^{129}Xe at the end of the inhalation tube connected to the TedLar bag. The gradual signal-to-noise ratio increase can be observed with increasing wash-in time. The slope map was created by a pixel-by-pixel linear fit of the ^{129}Xe brain images. (e) The perfusion map (measured in mL of blood per mL of tissue per min) created by the pixel-by-pixel recalculation of the TOF slope was used to calculate the sum of the perfusion rates of gray and white matter superimposed on top of a high-resolution proton brain image. The calculated values of perfusion agreed with previously observed values [41,46]. (g–i) Three dynamic TOF images acquired after 1s, 6.5 s, and 8 s TOF in the sagittal view. (j) Perfusion map in the sagittal view. Similar to e, the intensity values were the net sum of the white and gray matter perfusion rates.

3.3. HP ^{129}Xe Hemodynamic Response Detection

The blood-flow changes due to the hemodynamic response (HDR) to visual and motor stimuli (see Supplementary Material S3) were detected using 129Xe TOF perfusion imaging. The experimental designs for HP ^{129}Xe TOF and ^{1}H BOLD fMRI are shown in Figure 4-4a,c and Figure 4-5a,c. The reconstructed HDR maps nicely correlated with ^{1}H BOLD fMRI and demonstrated the activation of the same brain regions. Activation areas demonstrated on ^{129}Xe HDR maps agreed with previously published results [47–50].

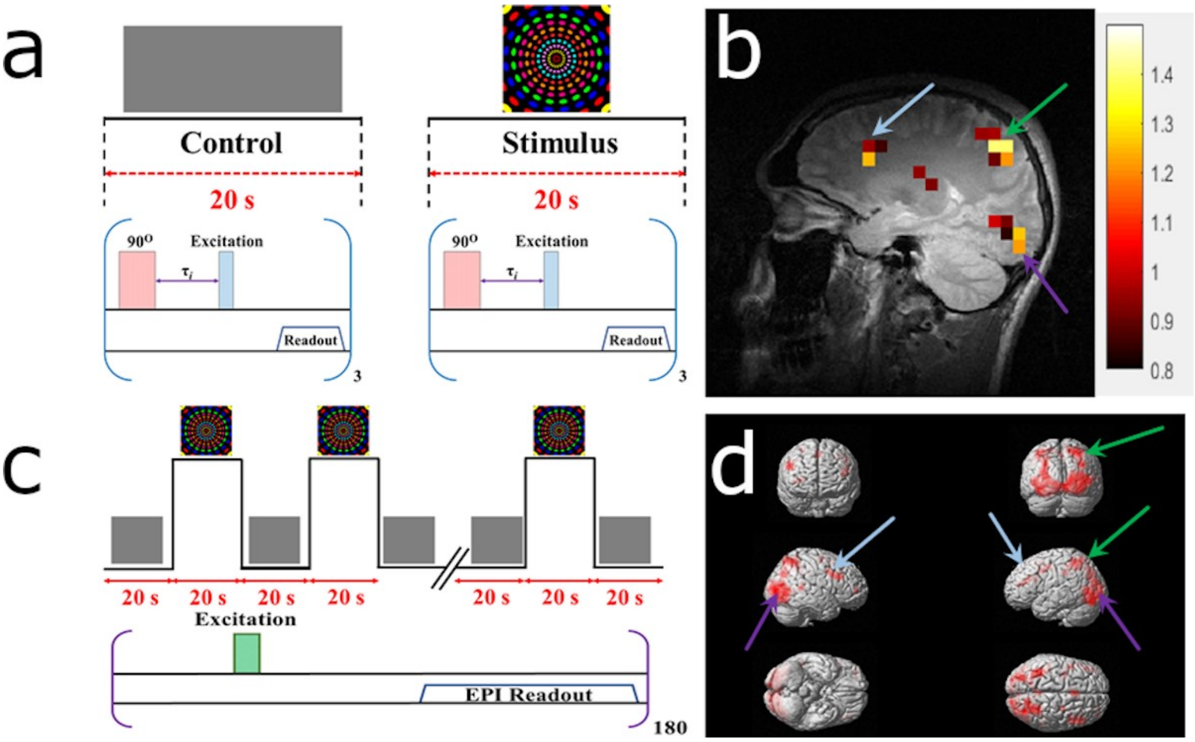

Figure 4-4. Detection of a hemodynamic response from a colorful visual stimulus using HP ^{129}Xe perfusion mapping validated by blood oxygenation level-dependent (BOLD) functional brain MRI (fMRI). (a) Experimental design used for hemodynamic response detection. Two separate perfusion maps were acquired during the control (gray screen) and visual stimulation. (b) Hemodynamic response map created by subtracting the control perfusion map from the stimulated perfusion map and overlaid on top of a high-resolution proton scan. Activation of the occipital lobe, superior parietal lobe, and frontal gyrus was observed. (c) BOLD fMRI experimental design for validation of the HP ^{129}Xe technique. (d) BOLD fMRI 3D activation maps demonstrate a correlation with a ^{129}Xe hemodynamic response map. The activated areas are indicated by colored arrows. The matched activated areas on the Xe image are indicated with arrows of the corresponding color.

Figure 4-4 illustrates the results obtained after subjecting the volunteer to the colorful rotating dotted visual stimulation. HP ^{129}Xe TOF detected activation of the visual cortex (occipital lobe), superior parietal lobe, and frontal gyrus (Figure 4-4b). These results completely agreed with ^{1}H BOLD fMRI images acquired by ^{129}Xe TOF image (Figure 4-4d).

Figure 4-5 illustrated the experimental design (a,c) and obtained ^{129}Xe TOF HDR maps (b) and ^{1}H BOLD fMRI images (d) of the representative volunteers subjected to the motor stimulus. Both approaches detected activation of the motor cortex contralaterally to the clenched fist.

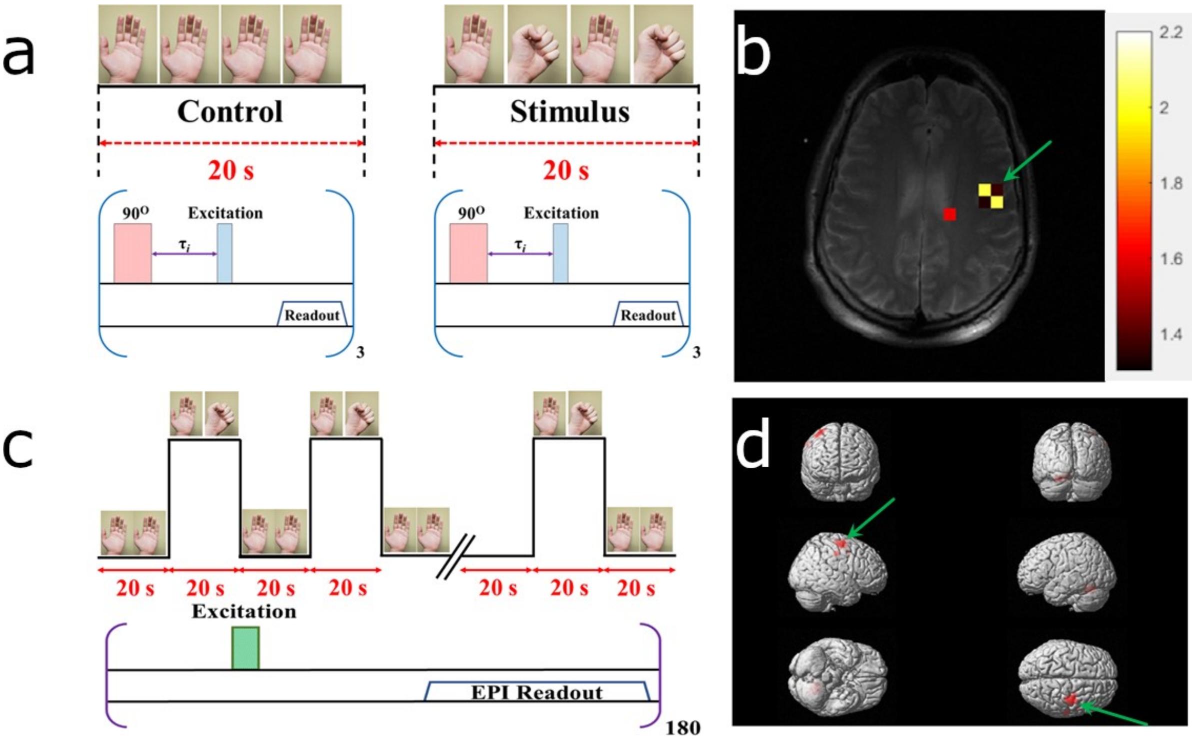

Figure 4-5. Detection of the hemodynamic response to a motor stimulus using HP ^{129}Xe perfusion mapping corroborated by blood oxygenation level-dependent (BOLD) functional brain MRI (fMRI). (a) Experimental design used for hemodynamic response detection. Two separate perfusion maps were acquired during the control (calm rest) and motor stimulation (left fist clenching) stages. (b) Hemodynamic response map created by subtracting the control perfusion map from the stimulated perfusion map and overlaid on top of the high-resolution proton scan. Activation of the right posterior precentral gyrus (i.e., the motor cortex) was observed. (c) BOLD fMRI experimental design for validation of the HP ^{129}Xe technique. (d) BOLD fMRI 3D activation maps. Activation was observed from the motor cortex (green arrow); this result correlated with the HP ^{129}Xe hemodynamic response map.

4. Discussion

There is no HP MRI approach currently available which is suitable for quantitative perfusion imaging. Recently, HP MRI was used to detect cerebral perfusion changes caused by stroke [35] and Alzheimer's disease [34]. Since HP ^{129}Xe freely dissolves in the blood and travels to highly perfused organs, it can be used as a contrast agent for quantitative imaging of perfusion and blood flow. Therefore, HP ^{129}Xe TOF blood flow mapping is a possible next step in blood flow and perfusion measurement.

Previous works focused on the dynamic acquisition of multiple brain projection images during a breath-hold and the following wash-out time of ^{129}Xe from the brain [6,33,34]. Acquired images were subsequently averaged [6,33] or postprocessed to characterize the wash-out process of ^{129}Xe from the brain [34]. These approaches were strongly dependent on variations in the breath-hold period and the individual lung capacities of the subjects. There is typically some signal variation in the ^{129}Xe images acquired from the same subject from different breath-holds due to individual variation in the amount of inhaled gas, the amount of gas actually in the alveolar lung space, and the amount of gas remaining in the trachea and larynx. Therefore, a proper comparison of images acquired from different breath-holds is challenging and requires proper signal normalization.

The HP ^{129}Xe TOF technique is the first differential HP MRI technique, to our knowledge, that relies on ^{129}Xe signal recovery rate calculation. This imaging approach is fundamentally different from all other MRI methods for blood flow mapping and relies on the special properties of HP MRI. An initial depolarization radiofrequency pulse applied to the imaging region provides the necessary reference for accurate imaging and makes the obtained perfusion-weighted images independent of individual lung capacity and breath-hold variations. In addition, the HP ^{129}Xe TOF approach allows quantitative perfusion mapping using the derived theory (see Supplementary Material S1).

Although HP ^{129}Xe blood flow mapping is similar to ASL in terms of pulse sequences, this technique overcomes the issue of low signal-to-noise ratio, which is typical for ASL perfusion images (the mean SNR of the Xe perfusion maps was approximately double compared to values acquired for ASL [39] ($p < 0.05$)) [1,51]. The obtained 129Xe perfusion maps (Figure 4-3e,j) looked similar to results previously obtained from healthy volunteers acquired using ASL MRI [52]. With the additional separation of the HP 129Xe signals originating from various brain tissues from the signal of ^{129}Xe dissolved in blood (either via different phase separation methods or using chemical shift selective imaging), it should be possible to quantitively map the perfusion of each tissue in a region of interest. Signal separation of the dissolved ^{129}Xe phases may allow the use of an exact mathematical solution for perfusion map calculations (see Supplementary Material S1), which would eliminate any potential underestimation of perfusion caused by using an approximate linear model.

Recently, multiple advances in ASL perfusion imaging were achieved by developing a pseudo-continuous ASL (pCASL), resulting in an SNR increase compared to conventional ASL [16–18,53]. pCASL perfusion images have higher spatial resolution compared to the present HP ^{129}Xe TOF images, mainly due to their significantly better developed hardware (multichannel coils used for parallel imaging during perfusion imaging) and software available for conducting proton ASL MRI. By using a parallel imaging approach, compressed sensing, non-Cartesian k-space trajectories, and by developing multichannel ^{129}Xe coils, it should be possible to acquire HP ^{129}Xe perfusion maps with a spatial resolution comparable to pCASL resolution and with a significantly higher SNR.

Although the scan time for acquiring a single brain perfusion map was ~20 s, it could be shortened to ~10 s by reducing TOF recovery time delays. The scan time could be shortened further for kidney perfusion measurements, since the reasonably high SNR of HP ^{129}Xe dissolved in the kidneys can be acquired in less than 4 s [35].

As one practical application, the HP ^{129}Xe perfusion mapping technique could be used for functional imaging of the human brain, which would allow direct hemodynamic response mapping. HP ^{129}Xe functional brain maps can be acquired significantly faster compared to traditional BOLD functional images. In addition, this approach requires less postprocessing than the BOLD technique, which makes it less ambiguous in terms of data processing. Although BOLD fMRI and HP ^{129}Xe perfusion mapping are two fundamentally different techniques and quantitative comparisons between them are challenging, the estimated percent signal enhancement of the functional maps obtained by HP ^{129}Xe perfusion mapping was up to two orders of magnitude larger than the BOLD fMRI images. Xenon gas is used in clinics as a general inhalation anesthetic with continuous breathing over several minutes at a total lung concentration greater than 50% [54]. Previous studies demonstrated an acceptably low incidence of adverse effects caused by inhalation of xenon with an overall alveolar concentration below 32% [55]. The concentration of inhaled HP ^{129}Xe in our study was 20–25% (considering a lung volume of 4–5 L), and there were no side effects observed after multiple inhalations and breath-holds.

A major limitation of the approach demonstrated for ^{129}Xe TOF functional imaging is the requirement of acquiring projection images instead of multislice images due to the limited quantity of HP ^{129}Xe that is transported to the brain. This issue can be overcome by using parallel imaging and compressed sensing techniques, which allow for faster acquisition with higher SNR per TOF image. Therefore, a larger number of slices can be scanned during a single breath-hold. Another limitation of HP ^{129}Xe perfusion mapping, in terms of its clinical relevance, is the ability of a participant to hold their breath. Although the short scan time required allows perfusion mapping in patients with lung diseases who can only tolerate short breath-hold periods, this technique is not possible for participants who cannot hold their breath for at least eight seconds. As an alternative, continuous breathing of an HP ^{129}Xe mixture with oxygen could be considered. A continuous breathing protocol has so far only been utilized for animal lung studies [56,57]. Translation of this breathing protocol to HP perfusion imaging might be challenging due to the oxygen-induced T_1 shortening of HP ^{129}Xe and subsequent decrease in the ^{129}Xe MRI signal. On the other hand, this approach could allow for multiple signal averaging and expand the application of HP ^{129}Xe TOF perfusion imaging. As a particular example, patients who are not able to hold their breath for eight seconds could be scanned using continuous breathing. Moreover, this might allow for HP ^{129}Xe perfusion imaging during clinical procedures when patients are under HP ^{129}Xe-induced anesthesia. Since the ^{129}Xe TOF technique is based on selective depolarization of ^{129}Xe nuclei, the MRI scanner needs to be properly calibrated, otherwise there will be an additional contribution to the signal from partially depolarized nuclei. Another potential limitation for some HP perfusion imaging applications is the time needed for ^{129}Xe polarization. The polarizer used in this study requires about 15 min to polarize 1 L of ^{129}Xe. Therefore, as a diagnostic tool, HP ^{129}Xe TOF might not be suitable for urgent imaging purposes. On the other hand, Xe was shown to demonstrate neuroprotective properties [58], indicating a potential use of this modality for cerebral perfusion imaging in stroke patients, for example. Finally, the other limitations of this technique are the high cost of enriched ^{129}Xe gas and the polarizer instrument. It should be noted that the use of enriched ^{129}Xe is required by an overall low HP ^{129}Xe signal in the brain. With further hardware development, the use of naturally abundant ^{129}Xe, which is substantially less expensive, is expected to become more feasible.

Overall, HP ^{129}Xe perfusion mapping is a novel HP MRI method which, we believe, could expand future knowledge in the field of perfusion imaging and functional brain mapping. It may also be a useful tool for the detection of perfusion changes in different organs and for further diagnostics regarding perfusion-related diseases.

5. Patents

Based on the results of this work, the provisional patent entitled “Method to Detect Brain Functional Activities Using Hyperpolarized 129Xe MR” was filed.

Supplementary Materials: The following are available online at http://www.mdpi.com/2075-4418/10/9/630/s1.

Author Contributions: Conceptualization, Y.S., F.T.H., T.L., A.H., and M.S.A.; methodology, Y.S., F.T.H., and V.G.; software, Y.S.; theoretical calculations, Y.S.; validation, Y.S., F.T.H, V.G., and T.L.; formal analysis, Y.S. and V.G; investigation, Y.S., F.T.H, V.G., and T.L.; resources, T.L. and F.T.H.; data curation, Y.S., F.T.H, V.G., and T.L.; writing—original draft preparation, Y.S; writing—review and editing, Y.S., F.T.H., V.G., T.L., A.H., and M.S.A; visualization, Y.S., F.T.H, V.G., and T.L.; supervision, A.H. and M.S.A; project administration, F.T.H., Y.S., M.S.A., and A.H.; funding acquisition, M.A and F.T.H. All authors have read and agreed to the published version of the manuscript.

Funding: This research was funded by the Ontario Research Fund (ORF RE 09 029) and the Northern Ontario Academic Medical Association (A-18-05). Y.S. received partial funding from the Mathematics of Information Technology and Complex Systems (Mitacs) Accelerate grant (IT10555) and an Ontario Graduate Scholarship. F.T.H. held postdoctoral fellowships from the BrightFocus Foundation (A2015344F) and the Canadian Institute for Health Research (358549). V.G. was supported by an Ontario Trillium Scholarship.

Acknowledgments: The authors would like to thank the numerous administrative and technical staff that assisted in conducting these experiments, including Martina Agostino, Nikka Stoger, Elizabeth Turubchuk, Kendra Rhys, Erin Venn, Sue Wright, James McNabb, Crystal Forsyth, Jane Lawrence-Dewar, and Karl Granberg. This project would not have been possible without the diligent assistance of these individuals. The authors would like to thank Dilip Balamore and Ariel Avilion for their valuable suggestions regarding the manuscript. The authors also thank Martina Agostino for her contributions to manuscript editing. M.S.A. would like to thank Dilip Balamore and Marcus Couch for stimulating discussions on this topic. The authors thank a reviewer of a previous draft of the manuscript for their insights on the topic of Xe perfusion imaging.

References

1. Petersen, E.T.; Zimine, I.; Ho, Y.C.L.; Golay, X. Non-invasive measurement of perfusion: A critical review of arterial spin labelling techniques. *Br. J. Radiol.* 2006, 79, 688–701. [CrossRef] [PubMed]

2. Lubbers, M.; Coenen, A.; Kofflard, M.; Bruning, T.; Kietselaer, B.; Galema, T.; Kock, M.; Niezen, A.; Das, M.; van Gent, M.; et al. Comprehensive Cardiac CTWith Myocardial Perfusion Imaging Versus Functional Testing in Suspected Coronary Artery Disease: The Multicenter, Randomized CRESCENT-II Trial. *JACC Cardiovasc. Imaging* 2018, 11, 1625–1636. [CrossRef] [PubMed]

3. Mori, H.; Isobe, S.; Suzuki, S.; Unno, K.; Morimoto, R.; Kano, N.; Okumura, T.; Yasuda, Y.; Kato, K.; Murohara, T. Prognostic value of left ventricular dyssynchrony evaluated by gated myocardial perfusion imaging in patients with chronic kidney disease and normal perfusion defect scores. *J. Nucl. Cardiol.* 2019, 26, 288–297. [CrossRef] [PubMed]

4. Gillis, K.A.; McComb, C.; Patel, R.K.; Stevens, K.K.; Schneider, M.P.; Radjenovic, A.; Morris, S.T.W.; Roditi, G.H.; Delles, C.; Mark, P.B. Non-Contrast Renal Magnetic Resonance Imaging to Assess Perfusion and Corticomedullary Differentiation in Health and Chronic Kidney Disease. *Nephron* 2016, 133, 183–192. [CrossRef] [PubMed]

5. Greenberg, D.A.; Jin, K. From angiogenesis to neuropathology. *Nature* 2005, 438, 954–959. [CrossRef] [PubMed]

6. Rao, M.R.; Norquay, G.; Stewart, N.J.; Hoggard, N.; Griffiths, P.D.; Wild, J.M. Assessment of brain perfusion using hyperpolarized 129Xe MRI in a subject with established stroke. *J. Magn. Reson. Imaging* 2019, 50, 1002–1004. [CrossRef]

7. Hu, W.T.; Wang, Z.; Lee, M.-Y.; Trojanowski, J.Q.; Detre, J.A.; Grossman, M. Distinct cerebral perfusion patterns in FTLD and AD. *Neurology* 2010, 75, 881–888. [CrossRef]

8. Ito, H.; Inoue, K.; Goto, R.; Kinomura, S.; Taki, Y.; Okada, K.; Sato, K.; Sato, T.; Kanno, I.; Fukuda, H. Database of normal human cerebral blood flow measured by SPECT: I. Comparison between 1-123-IMP, Tc-99m-HMPAO, and Tc-99m-ECD as referred with O-15 labeled water PET and voxel-based morphometry. *Ann. Nucl. Med.* 2006, 20, 131–138. [CrossRef]

9. Okazawa, H.; Higashino, Y.; Tsujikawa, T.; Arishima, H.; Mori, T.; Kiyono, Y.; Kimura, H.; Kikuta, K. ichiro Noninvasive method for measurement of cerebral blood flow using O-15 water PET/MRI with ASL correlation. *Eur. J. Radiol.* 2018, 105, 102–109. [CrossRef]

10. Kamath, A.; Smith, W.S.; Powers, W.J.; Cianfoni, A.; Chien, J.D.; Videen, T.; Lawton, M.T.; Finley, B.; Dillon, W.P.; Wintermark, M. Perfusion CT compared to H215O/O15O PET in patients with chronic cervical carotid artery occlusion. *Neuroradiology* 2008, 50, 745–751. [CrossRef]

11. Yonas, H.; Darby, J.M.; Marks, E.C.; Durham, S.R.; Maxwell, C. CBF Measured by Xe-CT: Approach to Analysis and Normal Values. *J. Cereb. Blood Flow Metab.* 1991, 11, 716–725. [CrossRef] [PubMed]

12. Johnson, U.; Engquist, H.; Howells, T.; Nilsson, P.; Ronne-Engström, E.; Lewén, A.; Rostami, E.; Enblad, P. Bedside Xenon-CT Shows Lower CBF in SAH Patients with Impaired CBF Pressure Autoregulation as Defined by Pressure Reactivity Index (PRx). *Neurocrit. Care* 2016, 25, 47–55. [CrossRef] [PubMed]

13. Fukuda, T.; Ogasawara, K.; Kobayashi, T.; Komoribayashi, N.; Endo, H.; Inoue, T.; Kuzu, Y.; Nishimoto, H.; Terasaki, K.; Ogawa, A. Measurement of cerebral hemodynamics with perfusion-weighted MR imaging: Comparison with pre- and post-acetazolamide 133Xe-SPECT in occlusive carotid disease. *AJNR Am. J. Neuroradiol.* 2001, 22, 248–254.

14. Golay, X.; Petersen, E.T. Arterial Spin Labeling: Benefits and Pitfalls of High Magnetic Field. *Neuroimaging Clin. N. Am.* 2006, 16, 259–268. [CrossRef] [PubMed]

15. Nery, F.; Gordon, I.; Thomas, D. Non-Invasive Renal Perfusion Imaging Using Arterial Spin Labeling MRI: Challenges and Opportunities. *Diagnostics* 2018, 8, 2. [CrossRef] [PubMed]

16. Vidorreta, M.; Wang, Z.; Chang, Y.V.; Wolk, D.A.; Fernández-Seara, M.A.; Detre, J.A. Whole-brain background-suppressed pCASL MRI with 1D-accelerated 3D RARE Stack-Of-Spirals readout. *PLoS ONE* 2017, 12, e0183762. [CrossRef]

17. Kilroy, E.; Apostolova, L.; Liu, C.; Yan, L.; Ringman, J.; Wang, D.J.J. Reliability of two-dimensional and three-dimensional pseudo-continuous arterial spin labeling perfusion MRI in elderly populations: Comparison with 15o-water positron emission tomography. *J. Magn. Reson. Imaging* 2014, 39, 931–939. [CrossRef]

18. Harteveld, A.A.; de Boer, A.; Franklin, S.L.; Leiner, T.; van Stralen, M.; Bos, C. Comparison of multi-delay FAIR and pCASL labeling approaches for renal perfusion quantification at 3T MRI. *Magn. Reson. Mater. Phys. Biol. Med.* 2020, 33, 81–94. [CrossRef]

19. Ni, L.; Li, J.; Li, W.; Zhou, F.; Wang, F.; Schwarz, C.G.; Liu, R.; Zhao, H.; Wu, W.; Zhang, X.; et al. The value of resting-state functional MRI in subacute ischemic stroke: Comparison with dynamic susceptibility contrast-enhanced perfusion MRI. *Sci. Rep.* 2017, 7, 1–8. [CrossRef]

20. Hashido, T.; Saito, S.; Ishida, T. A radiomics-based comparative study on arterial spin labeling and dynamic susceptibility contrast perfusion-weighted imaging in gliomas. *Sci. Rep.* 2020, 10, 6121. [CrossRef]

21. Sourbron, S.; Ingrisch, M.; Siefert, A.; Reiser, M.; Herrmann, K. Quantification of cerebral blood flow, cerebral blood volume, and blood-brain-barrier leakage with DCE-MRI. *Magn. Reson. Med.* 2009, 62, 205–217. [CrossRef] [PubMed]

22. Yerram, P.; Saab, G.; Karuparthi, P.R.; Hayden, M.R.; Khanna, R. Nephrogenic systemic fibrosis: A mysterious disease in patients with renal failure—Rrole of gadolinium-based contrast media in causation and the beneficial effect of intravenous sodium thiosulfate. *Clin. J. Am. Soc. Nephrol.* 2007, 2, 258–263. [CrossRef] [PubMed]

23. Perazella, M.A. Nephrogenic systemic fibrosis, kidney disease, and gadolinium: Is there a link? *Clin. J. Am. Soc. Nephrol.* 2007, 2, 200–202. [CrossRef] [PubMed]

24. Liu, X.; Madhankumar, A.B.; Miller, P.A.; Duck, K.A.; Hafenstein, S.; Rizk, E.; Slagle-Webb, B.; Sheehan, J.M.; Connor, J.R.; Yang, Q.X. MRI contrast agent for targeting glioma: Interleukin-13 labeled liposome encapsulating gadolinium-DTPA. *Neuro. Oncol.* 2016, 18, 691–699. [CrossRef] [PubMed]

25. Le Mignon, M.M.; Chambon, C.; Warrington, S.; Davies, R.; Bonnemain, B. Gd-DOTA. Pharmacokinetics and tolerability after intravenous injection into healthy volunteers. *Investig. Radiol.* 1990, 25, 933–937. [CrossRef]

26. Runge, V.M.; Clanton, J.A.; Price, A.C.; Wehr, C.J.; Herzer, W.A.; Leon Partain, C.; James, E. The Use of Gd dtpa as a Perfusion Agent and Marker of Blood-Brain Barrier Disruption. *Mqnnrrrc Krsonance Imaging* 1985, 3, 43–55. [CrossRef]

27. Albert, M.S.; Cates, G.D.; Driehuys, B.; Happer, W.; Saam, B.; Springer, C.S.; Wishnia, A. Biological Magnetic Resonance Imaging Using Laser-Polarized 129Xe. *Nature* 1994, 370, 199–201. [CrossRef]

28. Kruger, S.J.; Nagle, S.K.; Couch, M.J.; Ohno, Y.; Albert, M.; Fain, S.B. Functional imaging of the lungs with gas agents. *J. Magn. Reson. Imaging* 2016, 43, 295–315. [CrossRef]

29. Norquay, G.; Collier, G.J.; Rao, M.; Stewart, N.J.; Wild, J.M. Xe 129 -Rb Spin-Exchange Optical Pumping with High Photon Efficiency. *Phys. Rev. Lett.* 2018, 121, 153201. [CrossRef]

30. Skinner, J.G.; Ranta, K.; Whiting, N.; Coffey, A.M.; Nikolaou, P.; Rosen, M.S.; Chekmenev, E.Y.; Morris, P.G.; Barlow, M.J.; Goodson, B.M. High Xe density, high photon flux, stopped-flow spin-exchange optical pumping: Simulations versus experiments. *J. Magn. Reson.* 2020, 312, 106686. [CrossRef]

31. Ruset, I.C.; Ketel, S.; Hersman, F.W. Optical pumping system design for large production of hyperpolarized 129Xe. *Phys. Rev. Lett.* 2006, 96, 053002. [CrossRef] [PubMed]

32. Rao, M.; Stewart, N.J.; Norquay, G.; Griffiths, P.D.; Wild, J.M. High Resolution Spectroscopy and Chemical Shift Imaging of Hyperpolarized 129Xe Dissolved in the Human Brain In Vivo at 1.5 Tesla. *Magn. Reson. Med.* 2016, 75, 2227–2234. [CrossRef] [PubMed]

33. Rao, M.R.; Stewart, N.J.; Griffiths, P.D.; Norquay, G.; Wild, J.M. Imaging Human Brain Perfusion with Inhaled Hyperpolarized 129Xe MR Imaging. *Radiology* 2017, 286, 659–665. [CrossRef] [PubMed]

34. Hane, F.T.; Li, T.; Plata, J.-A.; Hassan, A.; Granberg, K.; Albert, M.S. Inhaled Xenon Washout as a Biomarker of Alzheimer’s Disease. *Diagnostics* 2018, 8, 41. [CrossRef]

35. Chacon-Caldera, J.; Maunder, A.; Rao, M.; Norquay, G.; Rodgers, O.I.; Clemence, M.; Puddu, C.; Schad, L.R.; Wild, J.M. Dissolved hyperpolarized xenon-129 MRI in human kidneys. *Magn. Reson. Med.* 2019. [CrossRef]

36. Chang, Y.V. MOXE: A model of gas exchange for hyperpolarized 129Xe magnetic resonance of the lung. *Magn. Reson. Med.* 2013, 69, 884–890. [CrossRef]

37. Fox, M.S.; Ouriadov, A.; Thind, K.; Hegarty, E.; Wong, E.; Hope, A.; Santyr, G.E. Detection of radiation induced lung injury in rats using dynamic hyperpolarized 129Xe magnetic resonance spectroscopy. *Med. Phys.* 2014, 41, 72302. [CrossRef]

38. Driehuys, B.; Cofer, G.P.; Pollaro, J.; Mackel, J.B.; Hedlund, L.W.; Johnson, G.A. Imaging alveolar-capillary gas transfer using hyperpolarized 129Xe MRI. *Proc. Natl. Acad. Sci. USA* 2006, 103, 18278–18283. [CrossRef]

39. Hare, H.V.; Blockley, N.P.; Gardener, A.G.; Clare, S.; Bulte, D.P. Investigating the field-dependence of the Davis model: Calibrated fMRI at 1.5, 3 and 7T. *Neuroimage* 2015, 112, 189–196. [CrossRef]

40. Ashburner, J.; Barnes, G.; Chen, C.C.; Daunizeau, J.; Flandin, G.; Friston, K.; Jafarian, A.; Kiebel, S.; Litvak, V.; Moran, R.; et al. SPM (Statistical Parametric Mapping); Wellcome Trust Centre for Neuroimaging: London, UK, 2014.

41. Kilian, W.; Seifert, F.; Rinneberg, H. Dynamic NMR Spectroscopy of Hyperpolarized 129Xe in Human Brain Analyzed by an Uptake Model. *Magn. Reson. Med.* 2004, 51, 843–847. [CrossRef]

42. Zhou, X.; Mazzanti, M.L.; Chen, J.J.; Tzeng, Y.S.; Mansour, J.K.; Gereige, J.D.; Venkatesh, A.K.; Sun, Y.; Mulkern, R.V.; Albert, M.S. Reinvestigating hyperpolarized 129Xe longitudinal relaxation time in the rat brain with noise considerations. *NMR Biomed.* 2008, 21, 217–225. [CrossRef] [PubMed]

43. Wolber, J.; Cherubini, A.; Leach, M.O.; Bifone, A. On the oxygenation-dependent 129 Xe T 1 in blood. *NMR Biomed.* 2000, 13, 234–237. [CrossRef]

44. Albert, M.S.; Kacher, D.F.; Balamore, D.; Venkatesh, A.K.; Jolesz, F.A. T 1 of 129 Xe in Blood and the Role of Oxygenation. *J. Magn. Reson.* 1999, 140, 264–273. [CrossRef] [PubMed]

45. Norquay, G.; Leung, G.; Stewart, N.J.; Tozer, G.M.; Wolber, J.; Wild, J.M. Relaxation and exchange dynamics of hyperpolarized 129Xe in human blood. *Magn. Reson. Med.* 2015, 74, 303–311. [CrossRef]

46. Peled, S.; Jolesz, F.A.; Tseng, C.-H.; Nascimben, L.; Albert, M.S.; Walsworth, R.L. Determinants of tissue delivery for 129Xe magnetic resonance in humans. *Magn. Reson. Med.* 1996, 36, 340–344. [CrossRef] [PubMed]

47. Neale, C.; Johnston, P.; Hughes, M.; Scholey, A. Functional Activation during the Rapid Visual Information Processing Task in aMiddle Aged Cohort: An fMRI Study. *PLoS ONE* 2015, 10, e0138994. [CrossRef] [PubMed]

48. Liu, Y.; Shen, H.; Zhou, Z.; Hu, D. Sustained Negative BOLD Response in Human fMRI Finger Tapping Task. *PLoS ONE* 2011, 6, e23839. [CrossRef]

49. Turesky, T.K.; Olulade, O.A.; Luetje, M.M.; Eden, G.F. An fMRI study of finger tapping in children and adults. *Hum. Brain Mapp.* 2018, 39, 3203–3215. [CrossRef]

50. Gountouna, V.E.; Job, D.E.; McIntosh, A.M.; Moorhead, T.W.J.; Lymer, G.K.L.; Whalley, H.C.; Hall, J.; Waiter, G.D.; Brennan, D.; McGonigle, D.J.; et al. Functional Magnetic Resonance Imaging (fMRI) reproducibility and variance components across visits and scanning sites with a finger tapping task. *Neuroimage* 2010, 49, 552–560. [CrossRef]

51. Zhao, L.; Fielden, S.W.; Feng, X.; Wintermark, M.; Mugler, J.P.; Meyer, C.H. Rapid 3D dynamic arterial spin labeling with a sparse model-based image reconstruction. *Neuroimage* 2015, 121, 205–216. [CrossRef]

52. Cui, Y.; Liang, X.; Gu, H.; Hu, Y.; Zhao, Z.; Yang, X.Y.; Qian, C.; Yang, Y.; Teng, G.J. Cerebral perfusion alterations in type 2 diabetes and its relation to insulin resistance and cognitive dysfunction. *Brain Imaging Behav.* 2017, 11, 1248–1257. [CrossRef] [PubMed]

53. Dai, W.; Garcia, D.; De Bazelaire, C.; Alsop, D.C. Continuous flow-driven inversion for arterial spin labeling using pulsed radio frequency and gradient fields. *Magn. Reson. Med.* 2008, 60, 1488–1497. [CrossRef] [PubMed]

54. Luttropp, H.H.; Thomasson, R.; Dahm, S.; Persson, J. Clinical experience with minimal flow xenon anesthesia. *Acta Anaesihessiol. Scand.* 1994, 38, 121–125. [CrossRef] [PubMed]

55. Latchaw, R.E.; Yonas, H.; Pentheny, S.; Gur, D. Adverse Reactions to Xenon-enhanced CT Cerebral Blood Flow Determination. *Radiology* 1987, 163, 251–254. [CrossRef]

56. Imai, H.; Matsumoto, H.; Miyakoshi, E.; Okumura, S.; Fujiwara, H.; Kimura, A. Regional fractional ventilation mapping in spontaneously breathing mice using hyperpolarized 129Xe MRI. *NMR Biomed.* 2015, 28, 24–29. [CrossRef]

57. Loza, L.A.; Kadlecek, S.J.; Pourfathi, M.; Hamedani, H.; Duncan, I.F.; Ruppert, K.; Rizi, R.R. Quantification of Ventilation and Gas Uptake in Free-Breathing MiceWith Hyperpolarized 129Xe MRI. *IEEE Trans. Med. Imaging* 2019, 38, 2081–2091. [CrossRef]

58. Homi, H.M.; Yokoo, N.; Ma, D.; Warner, D.S.; Franks, N.P.; Maze, M.; Ch, M.B.B.; Grocott, H.P. The Neuroprotective Effect of Xenon Administration during Transient Middle Cerebral Artery Occlusion in Mice. *Anesthesiology* 2003, 99, 876–881. [CrossRef]

4.2 Theoretical aspect of HP ^{129}Xe perfusion imaging

This topic has been elaborated in supplementary information to the following publication: **Shepelytskyi Y.**, Hane FT., Grynko V., Li T., Hassan A., and Albert MS. "**Hyperpolarized ^{129}Xe Time-of-Flight MR Imaging of Perfusion and Brain Function**" published in *Diagnostics*, volume 10, issue 9, Article number: 630 (2020). The derivation of theoretical HP ^{129}Xe SNR time evolution is presented below.

Theoretical aspect of HP ^{129}Xe perfusion imaging

Due to the solubility of ^{129}Xe in blood[1], the ^{129}Xe travels with the blood stream to the organs. Following Kilian's[2] model, the time evolution of the ^{129}Xe concentration within tissue obeys the differential equation:

$$\frac{dC_i(t)}{dt} = F_i\left(C_B(t) - \frac{1}{p_{iB}}C_i(t)\right) - \frac{C_i(t)}{T_{1i}}, \qquad [4\text{-}1]$$

where C$_i$ is a HP ^{129}Xe concentration within the tissue *i*, F$_i$ is a perfusion rate, p$_{iB}$, the partial coefficient between the tissue i and blood, T$_{1i}$ spin-lattice relaxation time of HP ^{129}Xe within the tissue i. Kilian's model can be expanded to describe the concentration of HP ^{129}Xe in a one image voxel. We consider a case of the brain imaging. We assume that the MRI signal caused by HP ^{129}Xe dissolved in white matter (WM), gray matter (GM) and blood. The concentration change in the one voxel can be expressed using the following system of equations:

$$\begin{cases} \dfrac{dC_W(t)}{dt} = F_W\left(C_B(t) - \dfrac{1}{p_{WB}}C_W(t)\right) - \dfrac{C_W(t)}{T_{1W}} \\ \dfrac{dC_G(t)}{dt} = F_G\left(C_B(t) - \dfrac{1}{p_{GB}}C_G(t)\right) - \dfrac{C_G(t)}{T_{1G}} \\ C_B(t) = \lambda_B C_{A,0} e^{-t\left(\frac{1}{T_{1A}} + \lambda_B \frac{Q}{V_A}\right)} e^{-\frac{t_B}{T_{1B}}} \end{cases}, \qquad [4\text{-}2]$$

where T$_{1A}$ is a spin-lattice relaxation time in the lungs; C$_B$, the ^{129}Xe concentration reaching the image voxel at time t; t$_B$, the time required for the blood to reach brain; λ_B, the Oswald solubility of ^{129}Xe in blood; T$_{1B}$, ^{129}Xe relaxation in blood; Q, pulmonary blood flow; V$_A$, alveolar volume. The first two equations are inhomogeneous differential equations of the first order. These equations can be solved using the Lagrange's variation of parameters method.

The solution of homogeneous differential equation for the ^{129}Xe concentration in white matter in which the integration constant was substituted by the time function is:

$$C_W = C_0(t)e^{-\beta_W t}. \qquad [4\text{-}3]$$

The $C_0(t)$ can be determined after substitution of [4.3] into correspondent equation of [4.2]:

$$C_0(t) = \frac{\xi F_W}{\beta_W - \gamma} e^{t(\beta_W - \gamma)} + C^*, \qquad [4\text{-}4]$$

where

$$\beta_W = \frac{F_W}{p_{WB}} + \frac{1}{T_{1W}}; \xi = \lambda_B C_{A0} e^{t_B\left(\frac{1}{T_{1A}} - \frac{1}{T_{1B}} + \lambda_B \frac{Q}{V_A}\right)}; \gamma = \frac{1}{T_{1A}} + \lambda_B \frac{Q}{V_A}. \qquad [4\text{-}5]$$

The integration constant C* can be calculated since we know that there is a time (t_B) that ^{129}Xe needs to reach the brain. This gives the following condition:

$$C_W(t_B) = 0 \Rightarrow C_0(t) = 0. \qquad [4\text{-}6]$$

Substituting [4.4] into [4.6], the integration constant C* can be obtained. The Xe concentration time dependence in WM can be written as follows:

$$C_W(t) = \frac{F_W \xi}{\beta_W - \gamma} e^{-\gamma t}\left(1 - e^{-(t - t_B)(\beta_W - \gamma)}\right). \qquad [4\text{-}7]$$

Using the same approach, the concentration of Xe in GM can be expressed as follows:

$$C_G(t) = \frac{F_G \xi}{\beta_G - \gamma}\left(1 - e^{-(t - t_B)(\beta_G - \gamma)}\right). \qquad [4\text{-}8]$$

Based on the definition of the partial coefficient, the Xe concentration in blood can be written as:

$$C_B = \frac{C_W + C_G}{p_{GB} + p_{WB}}. \qquad [4\text{-}9]$$

The net concentration of Xe in the image voxel can be described by the following equation:

$$C_{Voxel} = C_B + C_G + C_W$$

$$C_{Voxel} = \left(1 + \frac{1}{p_{WB} + p_{GB}}\right)\xi e^{-\gamma t}\left(\frac{F_G}{\beta_G - \gamma}\left(1 - e^{-(t - t_B)(\beta_G - \gamma)}\right) + \frac{F_W}{\beta_W - \gamma}\left(1 - e^{-(t - t_B)(\beta_W - \gamma)}\right)\right) \qquad [4\text{-}10]$$

Equation [4.10] describes both wash-in and wash-out of HP ^{129}Xe into and out of the voxel. To obtain a more accurate blood flow map, equation [4.10] should be corrected with respect to receiving bandwidth and used for pixel-by-pixel fit of ^{129}Xe TOF images. However, the fitting process becomes ambiguous due to symmetry of equation [4.10]. Indeed, converting F_G into F_W and β_G into β_W yields to the same function. Therefore, model simplifications are needed for data analysis. Considering wash-in phase and assuming that relaxation in blood is predominant factor of signal decay, the following simplification can be used:

$$\gamma \to 0; e^{-\gamma t} \to 1. \qquad [4\text{-}11]$$

Second, we consider a small sum of tissue perfusion and relaxivity of ^{129}Xe in tissue:

$$\frac{F_i}{p_{iB}} + \frac{1}{T_{1i}} << 1;\ 0 < \beta << 1 \Rightarrow 1 - e^{-\beta_i (t - t_B)} \approx \beta (t - t_B). \qquad [4\text{-}12]$$

Using assumptions [4.11] and [4.12], the equation [4.10] can be rewritten as:

$$C_{Voxel} = \left(1 + \frac{1}{p_{WB} + p_{GB}}\right) \xi \left(F_G + F_W\right)\left(t - t_B\right). \qquad [4\text{-}13]$$

Equation [4.13] is a linear function of time. The signal to noise ratio is proportional to the concentration of the nuclei (SNR=const·C_{Voxel}). Therefore, the signal to noise ratio evolution during the ^{129}Xe TOF scans can be written as:

$$SNR = SNR_0 \left(F_G + F_W\right)\left(\tau - t_B\right). \qquad [4\text{-}14]$$

The slope of equation S.14 is a scaled sum of perfusion rates of WM and GM. This equation can be used for creation of perfusion-weighted images of the human brain. By using similar approach, it is possible to analyse perfusion of any other organ.

The solution of the Eqn. [4.1] can be written as:

$$\begin{gathered} C_i(t) = \frac{F_i \xi}{\beta_i - \gamma} e^{-\gamma t} \left(1 - e^{-(t - t_B)(\beta_i - \gamma)}\right); \\ \beta_i = \frac{F_i}{p_{iB}} - \frac{1}{T_{1i}}; \xi = \lambda_B C_{A0} e^{t_B \left(\frac{1}{T_{1A}} - \frac{1}{T_{1B}} + \lambda_B \frac{Q}{V_A}\right)}; \gamma = \frac{1}{T_{1A}} + \lambda_B \frac{Q}{V_A}. \end{gathered} \qquad [4\text{-}15]$$

Considering N tissues in voxel, the net ^{129}Xe concentration can be expressed as follows:

$$C_{Tot}(t) = \sum_{i=1}^{N} C_i\left(t\right) + C_B\left(t\right); \qquad [4\text{-}16]$$

and the SNR evolution with TOF recovery obeys the following equation:

$$SNR\left(\tau\right) = SNR'\left(1 + \frac{1}{\sum_{i=1}^{N} p_{iB}}\right)\xi e^{-\gamma\tau}\sum_{i=1}^{N}\frac{F_i}{\beta_i - \gamma}\left(1 - e^{-(\tau - t_B)(\beta_i - \gamma)}\right). \qquad [4\text{-}17]$$

Eqn. [4.17] can be further simplify using similar to Eqn. [4.12] approach.

References

1. Zhou X, Mazzanti ML, Chen JJ, et al. Reinvestigating hyperpolarized 129Xe longitudinal relaxation time in the rat brain with noise considerations. NMR Biomed. 2008;21(3):217-225.

2. Kilian W, Seifert F, Rinneberg H. Dynamic NMR Spectroscopy of Hyperpolarized 129Xe in Human Brain Analyzed by an Uptake Model. Magn Reson Med. 2004;51(4):843-847. doi:10.1002/mrm.10726

3. Ogawa S, Lee TM, Nayak AS, Glynn P. Oxygenation-sensitive contrast in magnetic resonance image of rodent brain at high magnetic fields. Magn Reson Med. 1990;14(1):68-78. doi:DOI 10.1002/mrm.1910140108

Chapter 5: Conclusion and Future Work

5.1 Summary

Due to the increased demands in personalized medicine and improvements in functional imaging, multinuclear (or non-proton) MRI is becoming more and more popular. This approach utilizes a variety of different exogenous contrast agents containing non-proton nuclei which allows detection and visualization of organ function at disease sites. The most widely used areas of multinuclear MRI are ^{19}F MRI and HP MRI. Despite numerous advantages in the field, multiple challenges remain unresolved.

^{19}F MRI has relatively low SNR compared to conventional ^{1}H MRI due to the small concentration of injected ^{19}F nuclei. This fact results in typically low resolution of ^{19}F MRI images. Nevertheless, ^{19}F MRI of the lungs is capable of producing relatively high-resolution images (usually ~ 64x64 pixels) by employing a large number of signal averages (NSA). However, this high NSA results in excessive tissue heating due to the large quantity of RF pulses. Further SNR improvement is usually gained through implementation of non-Cartesian *k*-space sampling, but this results in poor resolution and can potentially cause image artifacts. Therefore, increasing the image SNR of ^{19}F images and implementing low-resolution and low-SNR ^{19}F molecular MRI are immediate needs.

This work demonstrated, for the first time, the possibility of low-resolution ^{19}F CSI implementation for tumor resistivity detection to 5-FU. The resistivity of HT-29 adenocarcinoma has been detected approximately one-hour post bolus injection of 5-FU. This methodology has potential to improve personalized cancer care significantly since there are no other early-stage tumor resistivity detection methods.

Furthermore, this work demonstrated the possibility of OFCB use as an inhalation contrast agent for ^{19}F lung MRI. Substantial SNR improvement compared to the most commonly used PFP gas is caused by the presence of eight magnetically equivalent ^{19}F nuclei per OFCB molecule. Moreover, OFCB has the longest apparent spin-spin relaxation time constant of all fluorinated gases used for lung imaging. These unique physical properties of the OFCB gas allowed up to 21% increase in image SNR with 60% less NSA compared to PFP.

Finally, this work resolves two major issues in HP ^{129}Xe brain imaging: a) the qualitative approach of imaging; and b) the sensitivity of HP ^{129}Xe brain imaging to pulmonological differences. Currently, imaging of HP ^{129}Xe dissolved in brain tissue strongly depends on the amount of HP ^{129}Xe inhaled by the human subject. Indeed, the signal of HP ^{129}Xe in the brain is directly proportional to the amount of HP ^{129}Xe dissolved in blood and, therefore, it is proportional to the amount of HP ^{129}Xe enclosed in the subject's lungs. Since the breathing capacity of people differs widely, the HP ^{129}Xe image SNR varies between subjects. Therefore, it is incredibly hard to compare images acquired from different subjects properly. Due to this variability, HP ^{129}Xe brain imaging mostly remained a qualitative approach to roughly estimate cerebral perfusion.

The HP ^{129}Xe TOF MRI pulse sequence, invented as part of this work, resolves these issues associated with HP ^{129}Xe brain imaging. Due to the presence of an initial depolarization pulse, HP ^{129}Xe TOF becomes almost insensitive to interpersonal pulmonological variations. The initial selective depolarization pulse sets the clear "baseline" with respect to which the signal evolution is measured. This technique makes the HP ^{129}Xe signal dependent mainly on CBF. Therefore, the demonstrated HP ^{129}Xe TOF pulse sequence is capable of quantifying direct blood flow and perfusion. The mathematical theory developed in this work enables quantitative perfusion mapping. The first HP ^{129}Xe cerebral perfusion image has been obtained from healthy volunteers.

As one particular example of HP ^{129}Xe TOF application, HDR detection was performed. The HDR to visual and motor stimuli was localized. HP ^{129}Xe HDR maps correlated well with conventional ^{1}H BOLD fMRI. However, the contrast mechanism of HP ^{129}Xe TOF HDR mapping is fundamentally different from BOLD since HP ^{129}Xe TOF pulse sequence quantifies CBF change directly and does not rely on oxygenation differences.

5.2 Future Work

5.2.1. Hardware development

The MRI image SNR strongly depends on the hardware used in experiments. Although the SNR of the acquired images was adequate to support the research hypotheses and is common for the research field, it limited the spatial resolution of the acquired scans. In order to facilitate further technology development and potential clinical translation, the image resolution and SNR should be increased substantially.

One of the main hardware aspects which determines the image SNR is an RF coil. All experiments conducted in this work utilized quadrature single-channel volume coils. Although quadrature coils provide sufficient SNR once properly calibrated, multichannel phased surface coil arrays can further increase the image SNR and decrease scan time. Currently, a parallel imaging approach with multichannel coils is well-developed for conventional proton MRI. On the other hand, parallel imaging is not so common in the field of multinuclear MRI. A four-channel RF receive coil has been developed for HP ^{129}Xe brain imaging recently[145] and has been used for two HP ^{129}Xe brain studies[1,2]. Sixteen-channel RF receivers are available for human lung imaging[3], are not yet commonly used.

Development and implementation of the multichannel phased-array receiver coils will be beneficial for all future studies based on the results described in this thesis. Utilization of the parallel imaging approach will allow a decrease in scan time for ^{19}F CSI and potentially increase NSA which will allow detection of 5-FU metabolites in tumor and liver. Decreased scan times and higher NSA will have dramatic effect on OFCB lung images due to a high OFCB SNR [4]. Finally, implementation of parallel imaging for dissolved phase HP ^{129}Xe imaging can sufficiently increase the SNR of HP TOF images, yielding more accurate perfusion recalculations and, potentialy, increased spatial resolution.

5.2.2. Improvement of the designed pulse sequences

Multiple pulse sequence improvements can be implemented in order to significantly improve performance of the developed MRI techniques.

HP ^{129}Xe TOF perfusion imaging was developed and tested using the conventional GRE pulse sequence with Cartesian *k*-space readout. Although this approach is quite simple and was mainly used in the field of HP ^{129}Xe brain imaging, TOF mathematical theory cannot be applied without simplifications for data analysis in case of simple GRE readout. This fact results in potential overestimation of perfusion values if TOF times exceed the quasilinear region of the SNR time recovery curve.

In order to apply Eqn. [4-17] for perfusion calculation, the phase separation technique integration into readout is required. This will allow separation of HP ^{129}Xe signals originating from different tissues with subsequent reconstruction of HP ^{129}Xe TOF images of each tissue separately. In the case of brain imaging, phase separation will allow one to reconstruct HP ^{129}Xe grey matter, white matter, soft muscle tissue, and blood TOF images. Each of these image sets can be further analysed using Eqn. [4-17] in order to achieve an accurate perfusion map of each tissue. Although there are multiple different phase separation methodologies, implementation of iterative decomposition with echo asymmetry and least squares estimation (IDEAL)[5-7] seems to be the most promising approach for HP ^{129}Xe TOF perfusion imaging taking into account the necessity of working during the single breath hold. Furthermore, potential implementation of non-Cartesian *k*-space trajectories such as spiral trajectories can help in IDEAL implementation for TOF imaging due to the overall shortening of scan time.

The compressed sensing data acquisition techniques are of increasing interest in the MRI field, and have been recently implemented in the area of lung ^{19}F imaging[8]. Briefly, this methodology relies on undersampling of the *k*-space data, preserving the spatial resolution of the resulting image. Compressed sensing allows significant scan time reduction compared to the conventional non-Cartesian *k*-space trajectories. Implementation of this technique will be extremely beneficial for OFCB lung imaging due to the potential of increasing the number of signal averages without substantial increase of the specific absorption rate.

5.2.3. Software development

Although numerous studies were done using ^{19}F and ^{129}Xe MRI, there is still no clear vision of the appropriate image analysis procedure. Each project discussed above requires development of an accurate and appropriate data analysis algorithm which can be freely used for further human experiments.

The SNR time dependencies of 5-FU measured from the different organs were approximated using an exponential function. Although this model was sufficient for classification of two different colorectal adenocarcinomas, the complete mathematical model of 5-FU dynamics should be developed in order to improve the accuracy and sensitivity of resistivity detection. Once a mathematical model is built, the dedicated CSI analyzing software should be developed and optimized prior to further implementation of this technique.

The SNR improvement caused by OFCB implementation for ^{19}F imaging of the lungs has a potential to significantly improve diagnostics of pulmonary diseases. However, the MRI image must be recalculated into the pulmonological parameters such as ventilation volume, ventilation defect percentage, etc. The first step of every lung image analysis is image segmentation with subsequent clusterization. Currently, one of the most commonly used segmentation approaches is *k*-mean algorithm[9]. However, the *k*-mean segmentation algorithm tends to fail at processing images with low SNR (which are most of the ^{19}F MRI images) and overestimates ventilated volume[10]. Therefore, development and implementation of the novel segmentation algorithm will be significantly beneficial for further ^{19}F MRI imaging of the lungs. In addition, implementation of neural network segmentation similar to the work of Zha et.al.[11] can revolutionize ^{19}F lung MRI.

Lastly, dedicated software capable of reconstructing HP ^{129}Xe TOF perfusion images using Eqn. [4-17] must be developed simultaneously with IDEAL readout implementation. Besides perfusion map recalculation, this software must be capable of ^{129}Xe/^{1}H brain image co-registration and realignment as well as of filtering and clusterization. In addition, in order to improve the HP ^{129}Xe image quality, the k-space lines should be corrected with respect to the FA of the excitation pulse. For example, the HP ^{129}Xe study described in Chapter 4 utilized a FA of 20^{O} resulting in approximately 6.1% loss of longitudinal magnetization for each subsequent line of k-space. Although the low-high arrangement of k-space can be used for increasing the image SNR, it also will result in some image blurring. Correction of the k-space lines with respect to an applied FA will reduce the blurring and result in a further SNR increase.

5.2.4. Correlation of 5-FU uptake and DCE MRI

The study discussed in Chapter 2 demonstrated 5-FU retention detection in colorectal adenocarcinoma. Despite the promising results, further study of 5-FU retention and its correlation with tumor perfusion is needed. Generally speaking, different tumor types likely have different vascularization which will result in different perfusion of the tumors. Because of this, the different amounts of 5-FU will reach different tumor types per unit of time. This will affect 5-FU uptake by the tumor and, potentially, might affect 5-FU retention in the tumor. In order to evaluate the tumor perfusion effect on 5-FU retention, either DCE MRI or ASL MRI should be performed and the average perfusion value of the tumor should be correlated with the 5-FU tumor retention value.

For accurate retention detection, normalization of the 5-FU signal with respect to a known standard should be performed. This normalization will eliminate potential influence of the 5-FU relaxation effects on the measured 5-FU retention. In addition, an accurate modeling of the 5-FU time dynamics should be performed.

5.2.5. Evaluation of a potential gravitational gas gradient of OFCB in human lungs

Since OFCB is a slightly denser gas than PFP (ρ_{C4F8} = 200 g/mol; ρ_{C3F8} = 188 g/mol), the gas distribution in the lungs might be inhomogeneous. This gravitational gradient in the gas distribution might cause an image inhomogeneity once large amounts of gas is inhaled and, therefore, can potentially be observed on the images of the human lungs. Therefore, comparison of image homogeneities should be performed between the human lung images acquired using PFP and OFCB.

In order to perform human lung imaging using OFCB, this fluorinated gas should be approved for human inhalation by Health Canada. Since OFCB is a non-toxic inert fluorinated gas, there should be no potential issues for getting all regulatory approvals for this gas.

5.3 Conclusion

This thesis demonstrates multiple techniques that are aimed at technical improvement and practical application of multinuclear MRI, specifically ^{19}F MRI and HP ^{129}Xe MRI. The methodologies described in this thesis demonstrate the ability of multinuclear MRI to serve as a functional imaging modality in oncology, pulmonology, and neurology.

Each technique developed during this work resolves at least one of the challenges previously associated with multinuclear MRI imaging. The ongoing image quality and data acquisition improvement will allow fast translation of these imaging techniques into the clinic.

5.4 References

1. Rao MR, Stewart NJ, Griffiths PD, Norquay G, Wild JM. Imaging Human Brain Perfusion with Inhaled Hyperpolarized 129 Xe MR Imaging. *Radiology*. 2017;286(2):659-665.
2. Rao MR, Norquay G, Stewart NJ, Hoggard N, Griffiths PD, Wild JM. Assessment of brain perfusion using hyperpolarized 129Xe MRI in a subject with established stroke. *J Magn Reson Imaging*. 2019;50(3):1002-1004. doi:10.1002/jmri.26686
3. Obert AJ, Gutberlet M, Kern AL, et al. 1H-guided reconstruction of 19F gas MRI in COPD patients. *Magn Reson Med*. 2020. doi:10.1002/mrm.28209
4. Shepelytskyi Y, Li T, Grynko V, Newman C, Hane FT, Albert MS. Evaluation of fluorine-19 magnetic resonance imaging of the lungs using octafluorocyclobutane in a rat model. *Magn Reson Med*. August 2020. doi:10.1002/mrm.28473
5. Doganay O, Stirrat E, McKenzie C, Schulte RF, Santyr GE. Quantification of regional

early stage gas exchange changes using hyperpolarized ^{129} Xe MRI in a rat model of radiation-induced lung injury. *Med Phys*. 2016;43(5):2410-2420. doi:10.1118/1.4946818

6. Reeder SB, Pineda AR, Wen Z, et al. Iterative decomposition of water and fat with echo asymmetry and least-squares estimation (IDEAL): Application with fast spin-echo imaging. *Magn Reson Med*. 2005. doi:10.1002/mrm.20624
7. Friedlander Y, Zanette B, Couch M, Kassner A, Santyr G. Spiral-IDEAL for Time-Resolved Imaging of Hyperpolarized 129Xe Kinetics in the Rat Brain. In: *Proc. Intl. Soc. Mag. Reson. Med. 27*. John Wiley and Sons Inc.; 2019:4300. doi:10.1002/mrm.27042
8. Neal MA, Pippard BJ, Hollingsworth KG, et al. Optimized and accelerated 19F-MRI of inhaled perfluoropropane to assess regional pulmonary ventilation. *Magn Reson Med*. 2019;82(4):1301-1311. doi:10.1002/mrm.27805
9. Kirby M, Heydarian M, Svenningsen S, et al. Hyperpolarized 3He Magnetic Resonance Functional Imaging Semiautomated Segmentation. *Acad Radiol*. 2012;19(2):141-152. doi:10.1016/j.acra.2011.10.007
10. Hughes PJC, Horn FC, Collier GJ, Biancardi A, Marshall H, Wild JM. Spatial fuzzy c-means thresholding for semiautomated calculation of percentage lung ventilated volume from hyperpolarized gas and ^{1} H MRI. *J Magn Reson Imaging*. 2018;47(3):640-646. doi:10.1002/jmri.25804
11. Zha W, Fain SB, Schiebler ML, Evans MD, Nagle SK, Liu F. Deep convolutional neural networks with multiplane consensus labeling for lung function quantification using UTE proton MRI. *J Magn Reson Imaging*. 2019;50(4):1169-1181. doi:10.1002/jmri.26734